UNIVERSITY OF CALIFORNIA
SANTA CRUZ

SINGLE-MOLECULE STUDIES OF HUMAN TELOMERIC DNA AND TELOMERE-INTERACTING PROTEINS

A dissertation submitted in partial satisfaction
of the requirements for the degree of

DOCTOR OF PHILOSOPHY

in

CHEMISTRY

by

Terren Chang

December 2020

The dissertation of Terren Chang is approved:

_____
Professor Michael Stone, chair

_____
Professor Seth Rubin

_____
Professor Susan Strome

_____
Quentin Williams
Acting Vice Provost and Dean of Graduate Studies

TABLE OF CONTENTS

List of Figures……..……...vi

Abstract…….…….....x

Acknowledgements…….…...xi

CHAPTER I:

INTRODUCTION…….……1

Telomere function…….……...1

Telomere maintenance mechanisms……..…….4

Telomere end protection…….……8

References…….12

Chapter II: SINGLE-MOLECULE MECHANICAL ANALYSIS OF STRAND INVASION IN HUMAN TELOMERE DNA……16

Abstract…….……..16

Introduction……....17

Results…….……...……19

Discussion……..29

References…….33

CHAPTER III: TELOMERE DNA G-QUADRUPLEX FOLDING WITHIN ACTIVELY EXTENDING HUMAN TELOMERASE……37

Abstract……..……..……38

Significance…….……...39

Introduction……....39

Results……...……...43

Discussion……..64

Materials and methods…….……69

References…….……..…..65

Supplementary methods…….…….73

Supplementary references……..…….……105

CHAPTER IV: GUIDE TO SETUP AND EXECUTION OF SINGLE-MOLECULE MAGNETIC TWEEZER EXPERIMENTS……..……..…017

Introduction……...…...107

Overview of the magnetic tweezers…….…….110

Flow cell assembly…….…112

Protocol for telomere molecule assembly for magnetic tweezer experiments…...…118

Protocol for telomere molecule immobilization……...…129

Magnetic tweezer microscope operation……123

References…….…….145

CHAPTER V: FUTURE DIRECTIONS……....148

TRF2 binding experiments……148

WRN protein, topoisomerase 1b, and camptothecin experiments……...153

Telomeric nucleosomes……157

References……..……..161

LIST OF FIGURES

Chapter 1:

Figure 1 – Telomeres and their role in chromosomal shortening……..……2

Table 1 – Telomeric DNA sequences of model organisms…..……..3

Figure 2 – Mechanism of telomerase-dependent telomere elongation……5

Figure 3 – G-quadruplex folding…….……...6

Figure 4 – The alternative lengthening of telomeres mechanism……..……...7

Figure 5 – The canonical shelterin complex…….……8

Figure 6 – Proposed mechanism of telomere end protection…….……9

Chapter2:

Figure 1 – Telomeric DNA for magnetic tweezers…….20

Figure 2 – DNA topology based strand invasion assay……22

Figure 3 – Tel7C invasion kinetics……...23

Figure 4 – Sequence dependence of strand invasion time trace complexity……..…25

Figure 5 – Stable D-loops result in a shift of the rotation extension curve……..…27

Chapter 3:

Figure 1 – Human telomerase function…….……..45

Figure 2 – The telomerase product distribution profile varies with the number of consecutive TTAGGG DNA repeats……...48

Figure 3 – POT1-TPP1 alters the telomerase product distribution profile……..…49

Figure 4 – The telomerase product distribution profile depends on monovalent cation identity…….51

Figure 5 – POT1-TPP1 does not enhance telomerase catalysis rates in GQ-destabilizing conditions……...53

Figure 6 – Human telomerase kinetics……...55

Figure 7 – Single-molecule studies of telomerase in the presence of KCl and LiCl..…59

Figure 8 – Model of GQ folding within an actively extending telomerase complex..….67

Figure S1 – RRL-reconstituted human telomerase compares to enzyme preparations from HEK293T-cells……..96

Figure S2 – Using radiolabeled dGTP or radiolabeled primer results in similar product accumulation profiles…….97

Figure S3 – Telomerase is processive in the presence of 50nM primer……..…98

Figure S4 – Telomerase activity is slower in Li^+……..…99

Figure S5 – Analysis of the kinetics of a primer extension assay described in Figure 6 using DynaFit……..…….100

Figure S6 – Reproducibility and self-consistency of kinetic analysis……101

Figure S7 – Real-time smFRET traces……102

Figure S8 – Model of a GQ within the telomerase enzyme……103

Table S1……DNA oligonucleotides used in this study……104

Chapter 4:

Figure 1 – Typical magnetic tweezer experimental setup……109

Figure 2 – Overview of the magnetic tweezers……111

Figure 3 – Guide hole positions……113

Figure 4 – Coverslip drill assembly……...113

Figure 5 – Coverslips help together with hose clamps……...114

Figure 6 – Outlet tubing assembly……115

Figure 7 – Fluidics assembly……..…116

Figure 8 – Flow cell assembly……...….116

Figure 9 – Assembled flow cell……..…117

Figure 10 – Tevzel nut assembly……...117

Figure 11 – Completed flow cell……..…118

Table 1 – PCR primers for DNA handles……...119

Figure 12 – Telomere molecule construction……..……120

Table 2 – DNA oligonucleotides used for adapters……....122

Figure 13 – pRST5 diagnostic double restriction enzyme digest gel……....124

Figure 14 – Autoligation gel……...125

Figure 15 – Telomere molecule gel……...127

Figure 16 – Magnetic tweezer controllers……123

Figure 17 – Andor XION 860 vi……...133

Figure 18 – Linear Stage Control vi……...134

Figure 19 – Rotation Control vi……..…136

Figure 20 – Bead Panel Tracker vi……....137

Figure 21 – NanoDrive Control……..138

Figure 22 – Bead Position vi……..139

Figure 23 – Bead Panel Math vi……140

Table 3 – Force calibration acquisition times……...141

Figure 24 – Force extension calibration……...142

Figure 25 – Double exponential fit of forces as a function of magnet position……143

Figure 26 – Worm-like chain fit……..144

Chapter 5:

Figure 1 – TRF2 binding magnetic tweezers experimental setup……149

Figure 2 – TRF2 dependent telomeric DNA compaction against an externally applied force……..150

Figure 3 – Proposed future force ramp experiment……...152

Figure 4 – Effects of SN-38 on the relaxation velocity of top1b……155

Figure 5 – Representative traces of top1b telomeric DNA relaxation in the presence of 125μM SN-38……156

Figure 6 – Confocal smFRET nucleosome positioning assay experimental setup.…158

Figure 7 – TRF2 orders heterogeneously position telomeric nucleosomes……159

Figure 8 – Proposed TIRF-based smFRET experiment……160

ABSTRACT

Terren Chang

Single-Molecule Studies Of Human Telomeric Dna And Telomere-Interacting Proteins

Telomeres are nucleoprotein structures that protect the ends of linear chromosomes. Telomeres serve two functions within the cell: to protect against genetic loss due to chromosomal shortening as a result of the end replication problem, and to distinguish chromosomal termini from sites of DNA damage that would otherwise elicit an unwanted DNA damage response. The foundation of telomere structures begins with a hexameric double-stranded repeat DNA sequence (TTAGGG in vertebrates) ranging from 2-20kb in length and terminate in a 3' G-rich single-stranded DNA overhang ranging from 50-300bp in length. Telomeric chromatin is known to contain tightly spaced nucleosomes, as well as a telomere-specific protein complex known as the shelterin complex. It is known that the shelterin complex is responsible for providing telomere end protection, however the mechanistic details of how this complex establishes end protection is lacking. Furthermore, how this complex transitions the telomere from a protected state required for end protection into an open deprotected state required for telomere replication remains largely unknown. This thesis outlines single-molecule studies of both telomeric DNA and telomere-interacting proteins to further our understanding of how these structures protect the genome.

ACKNOWLEDGEMENTS

I would like to thank my mother Nora Ross and my father Evan Chang for their unconditional support throughout my lifetime. Putting into words the magnitude of the help they have provided through this journey is impossible, as is overstating my gratefulness. Both taught me the value of education, and inspired me to pursue my ambitions. I would like to thank my sister Tristen, as it is no exaggeration to say this would have been impossible without her. I would like to thank my friends and family for their support and friendship. I would like to thank professor Seth Rubin and professor Susan Strome for their assistance and support throughout my graduate career. I would like to thank the members of the Stone lab for cultivating a fun and thought-provoking environment I was excited to be a part of everyday. Finally, I would like to thank my mentor Michael Stone, whose leadership, guidance, patience and care has truly inspired me.

CHAPTER I

INTRODUCTION

TELOMERE FUNCTION

During the course of evolution, higher biological organisms transitioned from storing genetic material in the form of circular chromosomes to linear DNA molecules. Circular chromosomes offer the advantage of being more easily replicated to completion, as the DNA replication machinery can synthesize the daughter strand of DNA while moving around the entire circular DNA molecule uninterrupted[1]. Although more difficult to maintain, linear chromosomes offered a clear advantage: the ability to better generate genetic diversity through mechanisms such as chromosomal crossing over[2], where sections of homologous chromosomes exchange genetic information, and the random combination of haploid chromosomes to form diploid cells during processes such as fertilization[3]. Along with these advantages, two major complications arose: the need to fully replicate the ends of chromosomes, a task of which the standard DNA replication machinery is incapable of performing[4], and the need to distinguish chromosomal termini from sites of DNA damage[5]. The former complication, if left unaddressed, could lead to the gradual shortening of chromosomes with each round of cellular replication, the loss of genetic information, and ultimately cell death.

The latter complication, if left unaddressed, could lead to the generation of an aberrant DNA damage response resulting in unwanted chromosomal fusion and genetic instability. The solution to both of these major complications in eukaryotic cell biology led to the evolution of telomeres: specialized nucleoprotein structures found at the termini of linear chromosomes. These structures simultaneously buffer against the gradual shortening of chromosomes by flanking the coding regions with non-coding DNA sequences and protect them from the loss of genetic information, while also distinguishing the ends of chromosomes from sites of DNA damage as to not illicit an unwanted DNA damage response.

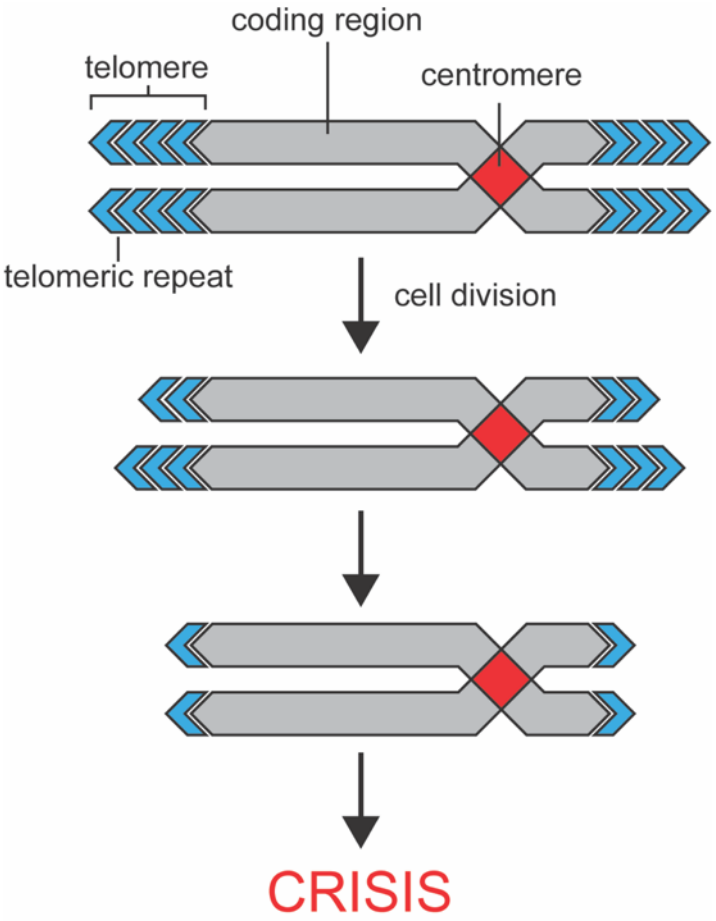

Figure 1 – Telomeres and their role in chromosomal shortening. The coding region of the DNA is shown in grey, centromeres in red, and telomeric repeats in blue. With each round of cellular division, telomeric DNA is lost due to the end replication problem and if left unchecked, the cellular response crisis is triggered.

The standard DNA replication machinery requires an upstream 5' RNA primer to initiate elongation of the daughter strand of DNA. While the leading strand can be

replicated to completion, the lagging strand lacks an upstream 5' RNA primer at the terminus of the parent strand, and therefore this DNA sequence is lost during replication. As a result, chromosomes gradually shorten with each round of cellular replication, a phenomenon termed the "end replication problem" (Figure 1). In the event chromosomes shorten past a critical length, a cellular checkpoint called crisis is reached, where cells either undergo apoptosis upregulate a telomere elongation mechanism.

Vertebrates	TTAGGG
S. pombe	G_{2-8}TTAC(A)
S. cerevisiae	$T(G)_{2-3}(TG)_{1-6}$
T. thermophila	TTGGGG
A. thaliana	TTTAGGG

Table 1 – Telomeric DNA sequences of model organisms. Although the sequences vary among organisms, the stretches of guanine bases within the repeats are highly conserved.

The foundation of telomere structure begins with a hexameric g-rich DNA tandem repeat sequence (TTAGGG in vertebrates). Although the sequence itself is not universally conserved among eukaryotes, the repetitive nature and stretches of guanine bases (G tracks) within the repeats are highly conserved (Table 1). The G tracks within the repeats impart interesting properties to the telomere and will be discussed later in this chapter. Telomeres range in length from ~2 – 20kbp (dependent on species, age, and tissue type) and terminate in a single-stranded 3' G-rich overhang from ~50 – 500 bases in length. This single-stranded overhang is vital to telomere function and therefore cellular health.

TELOMERE MAINTENANCE MECHANISMS

Telomeric DNA is synthesized by the specialized ribonucleoprotein telomerase[7] (Figure 2). The catalytic core of telomerase is comprised of two main components, the protein component telomerase reverse transcriptase (TERT) and the integrally bound telomerase RNA (TR). Telomerase is first recruited to the terminal 3' end of the telomere where it engages telomeric DNA through base pairing interactions with TR. Although this recruitment mechanism is largely unknown, it has been shown to be aided by telomere-specific binding proteins[8]. Once bound, telomerase reverse transcribes one telomere repeat templated off of TR, a process referred to as nucleotide addition processivity (NAP). Telomerase can then translocate to the newly formed 3' end of the DNA, where it can re-engage with TR or dissociate. If re-engaged, telomerase can again synthesize a second telomeric repeat, a process known as repeat addition processivity (RAP). It has been shown that telomerase is processive, and can synthesize many telomeric repeats in a given binding event[9]. Following G-strand synthesis by telomerase the complimentary C-rich strand is synthesized[10] followed by nucleolytic processing of the C-rich strand to maintain the G-rich overhang[11]. It is through this mechanism that telomerase positive cells are able to escape crisis, cellular senescence, and apoptosis. Escape from these vital

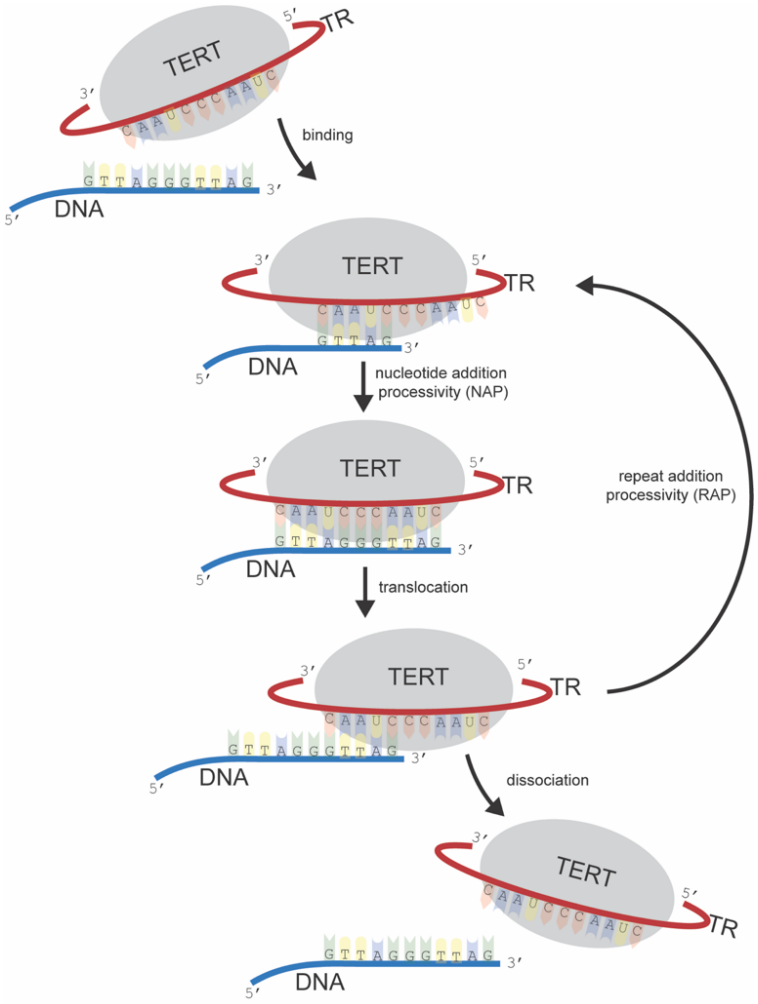

Figure 2 – Mechanism of telomerase-dependent telomere elongation. Telomerase is first recruited to the 3' end of the telomere. Telomerase then synthesized one telomeric repeat, translocated, and either dissociates or continues synthesizing telomeric DNA repeats.

checkpoints allows cells to divide indefinitely, and is responsible for the immortal phenotype of ~90% of human cancers.

It has been shown that single-stranded DNA sequences rich in G tracks have the propensity to fold into intramolecular secondary structures known as g-quadruplexes (GQ)[12]. GQs form when four guanine bases align in a plane by forming Hoogsteen base pairing interaction stabilized by a monovalent cation in the center of

the plane, a structure called a g-quartet (Figure 3A). A minimum of three g-quartets stack on each other stabilized by monovalent cations and π-π stacking interactions forming a GQ. The identity of the monovalent cation has an effect on the stability of the GQ, with a rank order of K^+>Na^+>Li^+, where Li^+ conditions disallow GQ folding[13]. Single stranded oligonucleotides containing the telomere sequence readily fold into GQs *in vitro*[14], and have been shown to play a role in telomerase catalysis regulation[15-17]. This finding has led to much effort being put forth to identify small molecule ligands that can bind to and stabilize these structures[18], and indeed the treatment of cells with these ligands provoke a cellular response[19].

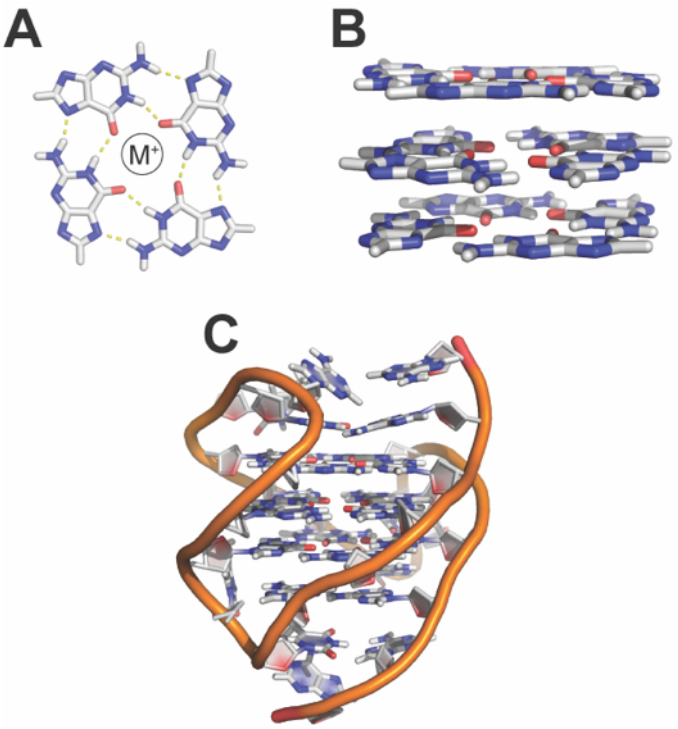

Figure 3 – G-quadruplex folding. A) A g-quartet is formed by four guanine bases formed by Hoogsteen base pairing stabilized by a monovalent cation in the center. B) A minimum of three g-quartets stack onto each other stabilized by monovalent cations and π-π interactions. C) The structure of a telomeric G-quadruplex (PDB: 2HY9).

There does exist a second telomerase-independent mechanism in which a cell can maintain telomere length, termed the “alternative lengthening of telomeres” (ALT) pathway[20]. One proposed mechanism for this pathway begins with the g-rich strand of one telomere invading and base pairing with a second telomere forming a

displacement loop (d-loop) in a process known as strand invasion (Figure 4), akin to the mechanism of homology-directed DNA repair[21]. During strand invasion, the displaced g-rich strand of the invaded telomere has the potential to fold into GQs, and this has a stabilizing effect on the structure *in vitro* (see chapter II). Once the d-loop is established, the replicative DNA polymerase pol∂ elongates the g-rich strand of the invading telomere templated off of the c-rich strand of the invaded telomere. After g-rich strand synthesis, the complementary c-rich strand is synthesized followed by nucleolytic processing to maintain the g-rich single stranded DNA overhang. This telomere maintenance is present in ~10-15% of human cancers, however it is worth

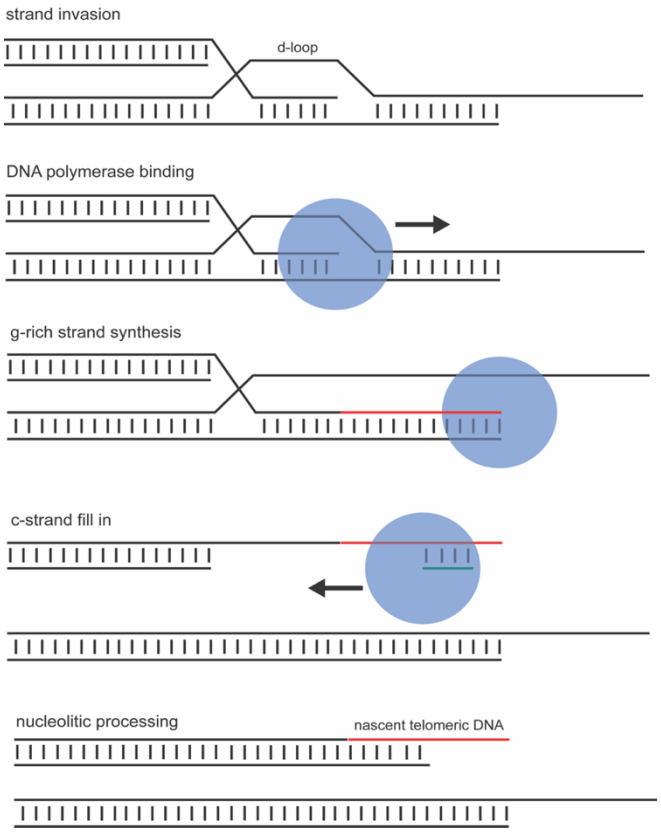

Figure 4 – The alternative lengthening of telomeres mechanism. The g-rich strand of one telomere invades the duplex region of another telomere establishing a d-loop. DNA polymerase pol∂ (blue) binds and elongated the invading g-rich strand using the invaded c-rich strand as a template. Once elongated, the complimentary c-rich strand is synthesized followed by nucleolytic processing to maintain the g-rich single stranded overhang.

noting that many telomerase-positive cancer cells can become resistant to telomerase specific inhibitors, likely because these cells adopt the ALT pathway, highlighting it's clinical importance[22].

TELOMERE END PROTECTION

The protein complex responsible for establishing telomere end protection is known collectively as shelterin[23] (Figure 5). There are six proteins in the canonical shelterin complex: telomere repeat binding factor 1 (TRF1), telomere repeat binding factor 2 (TRF2), repressor activator protein 1 (Rap1), TRF interacting nuclear factor 2 (TIN2), TPP1, and protection of telomeres 1 (POT1). TRF1 forms homodimers and other higher-order oligomers when bound to double-stranded DNA. TRF2 forms a dimer of heterodimers when bound to Rap1 and double-stranded DNA. Both the TRF proteins can bind double-stranded DNA non-specifically, but have a much higher affinity for the telomere sequence[24]. POT1 binds single-stranded telomeric DNA and has the capacity to resolve GQ structures[25]. TPP1 forms a homodimer with POT1 and also interacts with telomerase[26], increasing telomerase

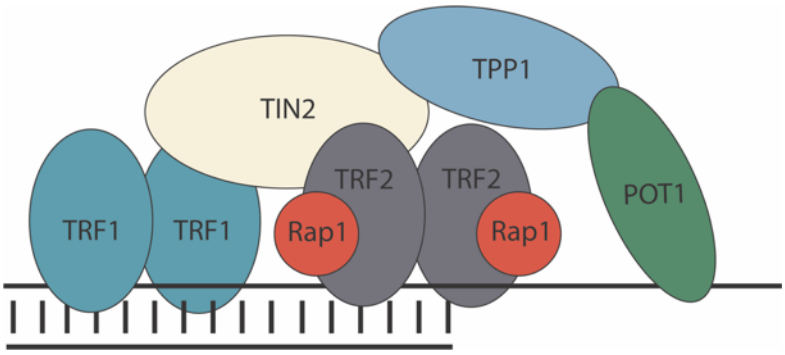

Figure 5 – The canonical shelterin complex. TRF1 and 2 both bind double-stranded telomeric DNA, the POT1:TPP1 heterodimer binds single-stranded telomeric DNA, and TIN2 bridges the two domains of the complex together.

processivity[27]. TIN2 binds to TRF1, TRF2, and TPP1 which bridges the double-stranded DNA binding and single-stranded DNA binding proteins in the complex. Although the number of double-stranded and single-stranded DNA binding proteins in the shelterin complex varies between species, what is well conserved is the shelterin complex always contains at least one double-stranded DNA binding protein, at least one single-stranded DNA binding protein, and typically a protein that will bridge the two (*S. cerevisiae* is a notable exception[5]).

The molecular details of how shelterin protects telomeres from eliciting an aberrant DNA damage response is not only largely unknown, it is also highly debated[28-30]. However, it is known that there is a division of labor amongst the shelterin proteins as to which DNA damage response pathway each protein represses. TRF1

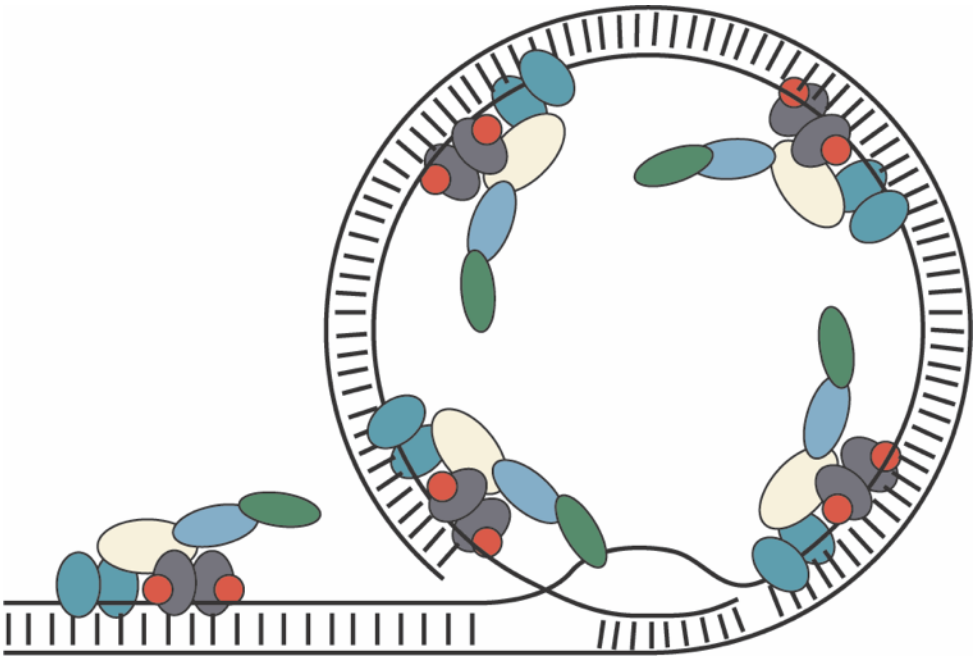

Figure 6 – Proposed mechanism of telomere end protection. The single-stranded g-rich overhang wraps back and invade the duplex region of the same telomere. Chiral wrapping of TRF2 generates compensatory torque that assists in DNA melting. The displaced strand of the d-loop is stabilized by adjacent POT1 binding.

deletion results in a robust ATM signaling-dependent DNA damage response[31], a mechanism activated when a double stranded break is detected. The ATR signaling pathway, which is activated when single-stranded DNA is detected, is activated upon removal of POT1. A proposed model for shelterin-mediated telomere protection is the formation of telomere loop (t-loop), a lariat structure formed when the terminal g-rich overhang wraps back and invades the duplex region of the same telomere[32] (Figure 6). Evidence that supports this model came from electron microscopy[32] and super-resolution microscopy, which showed t-loop formation to be TRF2 dependent[33]. This is further supported by the finding that TRF2 promoted strand invasion *in vitro*[34].

In chapter II of this thesis I will describe a single-molecule technique that studies the process of strand invasion at telomeres. I will describe that strand invasion required the aid of assisting torque applied to the DNA molecule, and directly measure the kinetics of telomeric strand invasion. I will further describe how the displaced strand of a telomeric d-loop folds into intramolecular GQs, and these structures have an overall stabilizing effect. The development of this assay can further be used as a platform to study how shelterin proteins interact with d-loops, and the effect small molecule ligands have on these structures.

Chapter III will describe a study investigating the roles GQ have while formed in the nascent strand of DNA by an actively extending telomerase enzyme. I will describe the finding that GQ formation modulates the kinetics of telomerase catalysis. This modulation is abolished in the presence of POT1:TPP1 heterodimer as well as in the presence of Li^+, both of which are refractory to GQ formation. This chapter concludes with a proposed model for how POT1:TPP1 acts as a telomerase processivity factor.

Chapter IV will describe the methods of performing a single-molecule magnetic tweezer experiment. I will first describe the method for the construction of materials used in the experiment. I will go on to describe the method for the creation of long telomeric DNA molecules of physiologically relevant length for the use in magnetic tweezer experiments, a first to my knowledge. I finally outline the procedure for the operation of the microscope and characterization and calibration of the DNA molecule.

In chapter V, I will outline future experiments to build on work I have done. I will describe experiments that probed the interaction of shelterin proteins and telomeric DNA using single-molecule magnetic tweezers. I will also describe work done using magnetic tweezers that investigated the ability of topoisomerase 1b to relax supercoiled telomeric DNA and the effect that a topoisomerase poison had on this enzyme. Finally, I will describe experiments I performed on telomeric nucleosomes, heterogeneity in their positioning on a telomere, and the effect TRF2 had on this hetergeneity.

REFERENCES

1. Marians, K. J., Prokaryotic DNA replication. *Annu Rev Biochem* **1992,** *61*, 673-719.

2. Szostak, J. W.; Orr-Weaver, T. L.; Rothstein, R. J.; Stahl, F. W., The double-strand-break repair model for recombination. *Cell* **1983,** *33* (1), 25-35.

3. Okabe, M., Sperm-egg interaction and fertilization: past, present, and future. *Biol Reprod* **2018,** *99* (1), 134-146.

4. Cech, T. R.; Lingner, J., Telomerase and the chromosome end replication problem. *Ciba Found Symp* **1997,** *211*, 20-8; discussion 28-34.

5. Palm, W.; de Lange, T., How shelterin protects mammalian telomeres. *Annu Rev Genet* **2008,** *42*, 301-34.

6. Counter, C. M.; Avilion, A. A.; LeFeuvre, C. E.; Stewart, N. G.; Greider, C. W.; Harley, C. B.; Bacchetti, S., Telomere shortening associated with chromosome instability is arrested in immortal cells which express telomerase activity. *EMBO J* **1992,** *11* (5), 1921-9.

7. Greider, C. W.; Blackburn, E. H., Identification of a specific telomere terminal transferase activity in Tetrahymena extracts. *Cell* **1985,** *43* (2 Pt 1), 405-13.

8. Schmidt, J. C.; Zaug, A. J.; Kufer, R.; Cech, T. R., Dynamics of human telomerase recruitment depend on template-telomere base pairing. *Mol Biol Cell* **2018,** *29* (7), 869-880.

9. Greider, C. W., Telomerase is processive. *Mol Cell Biol* **1991,** *11* (9), 4572-80.

10. Feng, X.; Hsu, S. J.; Kasbek, C.; Chaiken, M.; Price, C. M., CTC1-mediated C-strand fill-in is an essential step in telomere length maintenance. *Nucleic Acids Res* **2017,** *45* (8), 4281-4293.

11. Martina, M.; Clerici, M.; Baldo, V.; Bonetti, D.; Lucchini, G.; Longhese, M. P., A balance between Tel1 and Rif2 activities regulates nucleolytic processing and elongation at telomeres. *Mol Cell Biol* **2012,** *32* (9), 1604-17.

12. Spiegel, J.; Adhikari, S.; Balasubramanian, S., The Structure and Function of DNA G-Quadruplexes. *Trends Chem* **2020,** *2* (2), 123-136.

13. Lane, A. N.; Chaires, J. B.; Gray, R. D.; Trent, J. O., Stability and kinetics of G-quadruplex structures. *Nucleic Acids Res* **2008,** *36* (17), 5482-515.

14. Tippana, R.; Xiao, W.; Myong, S., G-quadruplex conformation and dynamics are determined by loop length and sequence. *Nucleic Acids Res* **2014,** *42* (12), 8106-14.

15. Zahler, A. M.; Williamson, J. R.; Cech, T. R.; Prescott, D. M., Inhibition of telomerase by G-quartet DNA structures. *Nature* **1991,** *350* (6320), 718-20.

16. Patrick, E. M.; Slivka, J. D.; Payne, B.; Comstock, M. J.; Schmidt, J. C., Observation of processive telomerase catalysis using high-resolution optical tweezers. *Nat Chem Biol* **2020,** *16* (7), 801-809.

17. Jansson, L. I.; Hentschel, J.; Parks, J. W.; Chang, T. R.; Lu, C.; Baral, R.; Bagshaw, C. R.; Stone, M. D., Telomere DNA G-quadruplex folding within actively extending human telomerase. *Proc Natl Acad Sci U S A* **2019,** *116* (19), 9350-9359.

18. Asamitsu, S.; Obata, S.; Yu, Z.; Bando, T.; Sugiyama, H., Recent Progress of Targeted G-Quadruplex-Preferred Ligands Toward Cancer Therapy. *Molecules* **2019,** *24* (3).

19. Tauchi, T.; Shin-ya, K.; Sashida, G.; Sumi, M.; Okabe, S.; Ohyashiki, J. H.; Ohyashiki, K., Telomerase inhibition with a novel G-quadruplex-interactive agent, telomestatin: in vitro and in vivo studies in acute leukemia. *Oncogene* **2006,** *25* (42), 5719-25.

20. Cesare, A. J.; Reddel, R. R., Alternative lengthening of telomeres: models, mechanisms and implications. *Nat Rev Genet* **2010,** *11* (5), 319-30.

21. Dilley, R. L.; Verma, P.; Cho, N. W.; Winters, H. D.; Wondisford, A. R.; Greenberg, R. A., Break-induced telomere synthesis underlies alternative telomere maintenance. *Nature* **2016,** *539* (7627), 54-58.

22. Recagni, M.; Bidzinska, J.; Zaffaroni, N.; Folini, M., The Role of Alternative Lengthening of Telomeres Mechanism in Cancer: Translational and Therapeutic Implications. *Cancers (Basel)* **2020,** *12* (4).

23. de Lange, T., Shelterin: the protein complex that shapes and safeguards human telomeres. *Genes Dev* **2005,** *19* (18), 2100-10.

24. Zhong, Z.; Shiue, L.; Kaplan, S.; de Lange, T., A mammalian factor that binds telomeric TTAGGG repeats in vitro. *Mol Cell Biol* **1992,** *12* (11), 4834-43.

25. Lee, C. Y.; McNerney, C.; Myong, S., G-Quadruplex and Protein Binding by Single-Molecule FRET Microscopy. *Methods Mol Biol* **2019,** *2035*, 309-322.

26. Nandakumar, J.; Bell, C. F.; Weidenfeld, I.; Zaug, A. J.; Leinwand, L. A.; Cech, T. R., The TEL patch of telomere protein TPP1 mediates telomerase recruitment and processivity. *Nature* **2012,** *492* (7428), 285-9.

27. Wang, F.; Podell, E. R.; Zaug, A. J.; Yang, Y.; Baciu, P.; Cech, T. R.; Lei, M., The POT1-TPP1 telomere complex is a telomerase processivity factor. *Nature* **2007,** *445* (7127), 506-10.

28. Bandaria, J. N.; Qin, P.; Berk, V.; Chu, S.; Yildiz, A., Shelterin Protects Chromosome Ends by Compacting Telomeric Chromatin. *Cell* **2016,** *164* (4), 735-46.

29. Timashev, L. A.; Babcock, H.; Zhuang, X.; de Lange, T., The DDR at telomeres lacking intact shelterin does not require substantial chromatin decompaction. *Genes Dev* **2017,** *31* (6), 578-589.

30. Vancevska, A.; Douglass, K. M.; Pfeiffer, V.; Manley, S.; Lingner, J., The telomeric DNA damage response occurs in the absence of chromatin decompaction. *Genes Dev* **2017,** *31* (6), 567-577.

31. Celli, G. B.; de Lange, T., DNA processing is not required for ATM-mediated telomere damage response after TRF2 deletion. *Nat Cell Biol* **2005,** *7* (7), 712-8.

32. Griffith, J. D.; Comeau, L.; Rosenfield, S.; Stansel, R. M.; Bianchi, A.; Moss, H.; de Lange, T., Mammalian telomeres end in a large duplex loop. *Cell* **1999,** *97* (4), 503-14.

33. Doksani, Y.; Wu, J. Y.; de Lange, T.; Zhuang, X., Super-resolution fluorescence imaging of telomeres reveals TRF2-dependent T-loop formation. *Cell* **2013,** *155* (2), 345-356.

34. Benarroch-Popivker, D.; Pisano, S.; Mendez-Bermudez, A.; Lototska, L.; Kaur, P.; Bauwens, S.; Djerbi, N.; Latrick, C. M.; Fraisier, V.; Pei, B.; Gay, A.; Jaune, E.; Foucher, K.; Cherfils-Vicini, J.; Aeby, E.; Miron, S.; Londono-Vallejo, A.; Ye, J.; Le Du, M. H.; Wang, H.; Gilson, E.; Giraud-Panis, M. J., TRF2-Mediated Control of Telomere DNA Topology as a Mechanism for Chromosome-End Protection. *Mol Cell* **2016,** *61* (2), 274-86.

CHAPTER II

SINGLE-MOLECULE MECHANICAL ANALYSIS OF STRAND INVASION IN HUMAN TELOMERE DNA

ABSTRACT

Telomeres are essential chromosome end capping structures that safeguard the genome from dangerous DNA processing events. DNA strand invasion occurs during vital transactions at telomeres, including telomere length maintenance by the alternative lengthening of telomeres (ALT) pathway. During telomeric strand invasion, a single stranded guanine-rich (G-rich) DNA invades at a complementary duplex telomere repeat sequence forming a displacement loop (D-loop) in which the displaced DNA consists of the same G-rich sequence as the target duplex DNA. Single stranded G-rich telomeric DNA readily folds into stable, compact, structures called G-quadruplexes (GQ) *in vitro*, and is anticipated to form within the context of a D-loop; however, evidence supporting this hypothesis is lacking. Here we report a magnetic tweezers assay that permits the controlled formation of telomeric D-loops (TDLs) within uninterrupted duplex human telomere DNA molecules of physiologically relevant lengths. Our results are consistent with a model wherein the displaced single stranded DNA of a TDL folds into a GQ. This study provides new insight into telomere

structure and establishes a framework for development of novel therapeutics designed to target GQs at telomeres in cancer cells.

INTRODUCTION

Telomeres safeguard the genome by distinguishing chromosomal termini from sites of DNA lesions which would otherwise elicit an unwanted DNA damage response resulting in chromosomal fusion, genomic instability, and often apoptosis[1]. The foundation of telomere structure begins with tandem hexameric guanine-rich (G-rich) repetitive DNA (GGTTAG in humans) ~2 – 20 kilobases in length[2] and terminates with a ~50 – 300 nucleotide long single stranded G-rich 3' overhang[3]. Telomeres also act to buffer against the end replication problem, wherein chromosomes gradually shorten with each subsequent round of cell division. Replication-dependent telomere attrition can compromise the protective function of telomeres as well as lead to a loss of genetic information if left unaddressed[4]. Therefore, continually dividing cells, including the majority of human cancers, must maintain telomere length to support an immortal phenotype[5]. Most highly proliferative cell types upregulate the specialized enzyme telomerase, which reverse transcribes telomeric DNA to chromosomal termini using an RNA template that resides within the integral telomerase RNA subunit[6]. However, many aggressive cancer subtypes employ a telomerase-independent mechanism for telomere maintenance termed alternative lengthening of telomeres (ALT). In ALT cells, the 3' single stranded DNA (ssDNA) overhang of one telomere base-pairs with the duplex region of another telomere, in a manner similar to early steps in homology

directed repair[7]. This telomeric strand invasion event forms a displacement loop (D-loop), where the single stranded G-rich 3' overhang base-pairs with the C-rich strand of the invaded telomere, displacing the G-rich strand[8]. The 3' overhang can then be extended by a specialized DNA polymerase using the invaded telomere as a template, followed by C-strand fill in and nucleolytic processing to maintain the 3' overhang[9].

Single stranded G-rich telomeric DNAs readily fold into compact structures called G-quadruplexes (GQ) *in vitro*, where four guanine bases participating in Hoogsteen base-pairing align in a plane while coordinating a monovalent cation at the center[10]. The stability of GQs is highly dependent on the identity of the monovalent cation, with a rank order of $K^+ > Na^+ > Li^+$, in terms of degree of stabilization[11]. Furthermore, small molecule ligands designed to target GQ structures elicit a phenotype in living cells, suggesting a possible regulatory role for these structures *in vivo*[12]. Therefore, much effort has been put forth to identify potential GQ forming sequences in the genome to expand the potential targets for these molecules to be used as therapeutics[13]. In the current study, we report results from a single-molecule mechanical assay of DNA strand invasion at human telomeres. Using a magnetic tweezers system, uninterrupted duplex telomere DNA molecules as long as ten kilobases can be manipulated in order to impart precise degrees of tension and torque to the system. Strand invasion by single-stranded DNA oligonucleotides in solution can be monitored in real-time as a change in the overall extension of the telomere DNA duplex target molecule. To our knowledge, this assay represents the first to permit direct detection of telomeric D-loops (TDLs) at the single-molecule level. We find that conditions which disfavor GQ folding dramatically alter the properties of TDLs, suggesting a role for GQ folding within

these important structures. Finally, this system provides an opportunity to analyze the binding of small molecule drugs that may bind and stabilize GQ structures within a TDL, and also represents a powerful new system for studies of replication associated factors that may bind and resolve TDLs *in vivo*.

RESULTS

Single molecule manipulation of long human telomere DNA molecules

The DNA molecules used in the present work consist of between nine to twelve kilobases of uninterrupted double-stranded telomeric DNA sequence. The telomere DNA molecule is flanked by biotin- or digoxigenin-modified DNA linker fragments used to immobilize the DNA tether between a streptavidin-coated magnetic bead and an anti-digoxigenin coated glass slide, respectively (Figure 1A and 1B). To generate these long, uninterrupted, telomere DNA tether molecules for single-molecule analysis in our magnetic tweezers microscope, we perform a controlled DNA concatenation

reaction seeded on the digoxigenin linker fragment using a 576 base pair telomere DNA fragment with incompatible sticky ends generated by restriction endonuclease cleavage of the previously reported pRST5 DNA plasmid[14]. Following multiple rounds of DNA ligation, the molecule is ultimately capped by ligation of the biotin-modified DNA linker fragment and gel purified to remove unwanted reaction side products and excess handle material.

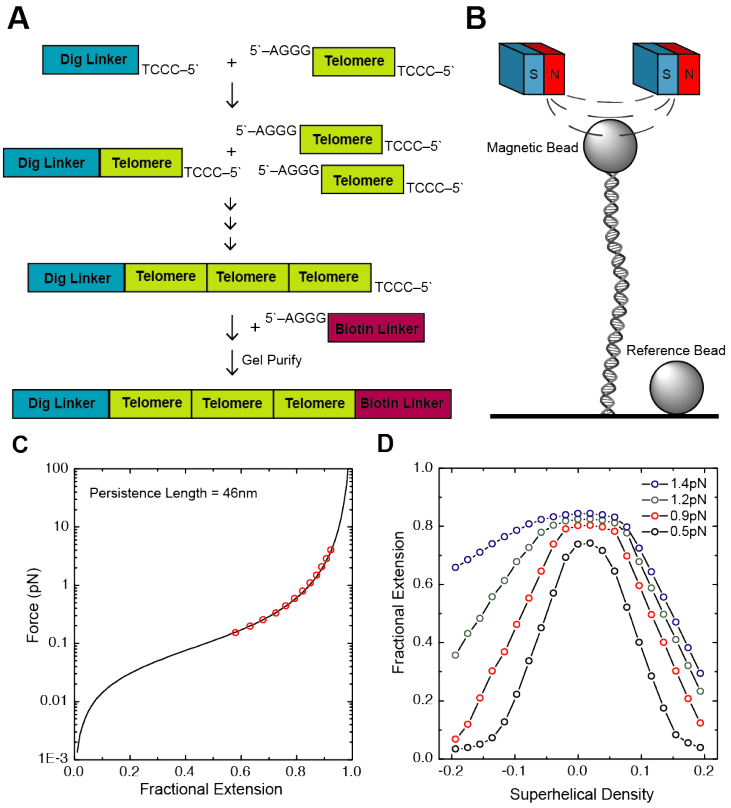

Figure 1. Telomeric DNA for magnetic tweezers. (A) Schematic of the construction of telomeric DNA molecules used in this study. (B) Schematic of the magnetic tweezers instrument. The z-position of the magnets is adjusted to control the force exerted on the tethered DNA molecule. The magnets can also be rotated to apply torque. (C) Force extension curve of telomeric DNA. Data points are in red with the wormlike chain fit in black. (D) Rotation extension curves of telomeric DNA at various forces.

The elasticity of doubled stranded DNA is well described by the worm-like chain (WLC) polymer model[15] and is characterized by a bending persistence length ranging from ~45-50 nanometers (nm), depending upon the ionic strength[11]. To test whether our telomere DNA tethers exhibit unique elastic properties due to their highly repetitive G-rich sequence, we performed force-extension analysis. Our results indicate that long

double-stranded telomere DNA molecules exhibit canonical DNA elastic properties with an average persistence length of 46 +/- 4 nm under the conditions of our experiments (10 mM TRIS pH 7.5, 150 mM KCl, 0.5mg/mL BSA) (Figure 1C). Next, we analyzed the supercoiling response of our telomere DNA tethers by rotating the magnets held above a molecule of interest, which permits precise introduction of positive or negative superhelical strain into the system. DNA tether extension data were collected for a variety of supercoiling densities, given by the expression $\sigma = \Delta L_k / L_{ko}$, where σ is the supercoiling density, ΔL_k is the change in DNA linking number (i.e. integer number of magnet rotations), and L_{ko} is the linking number of the DNA molecule in a topologically relaxed state (i.e. the total number of DNA base pairs in the tether divided by the number of base pairs per helical turn of the double helix) (Figure 1D). For example, at a stretching force of ~ 0.9 pico-Newtons (pN) the telomere DNA tether compacted in a highly symmetric manner when comparing the negative and positive supercoiling regimes, consistent with formation of plectonemic supercoils (Figure 1D).

Real-time observation of DNA strand invasion in human telomere DNA

Having characterized the physical properties of the telomere DNA tethers, we next developed a DNA topology based assay to directly measure telomere DNA strand invasion in real time (Figure 2A). The molecule was initially negatively supercoiled resulting in a decrease in extension. When the molecule was stretched to 0.9 pN of force, the negative superhelical density imparted torque on the molecule, which resulted in transient, local destabilization of the DNA double helix and facilitated strand invasion by a freely diffusing complementary DNA oligonucleotide from solution[16]

(Figure 2A and 2B). In this assay, the negatively supercoiled telomere DNA tether represents a closed topological system. Therefore, the local DNA unwinding that must occur upon strand invasion imparts compensatory positive supercoiling into the molecule, which in turn cancels some of the pre-existing negative supercoiling, resulting in a sudden increase in the DNA tether extension when held at constant force (Figure 2B, black arrowheads). To initially characterize strand invasion in our system we monitored the properties of a 42 nucleotide long single-stranded invading DNA molecule comprised of seven repeats of the C-rich telomere DNA strand sequence (tel7C). Although this oligonucleotide is the complement of the physiologically relevant G-rich ssDNA telomere tail, it has the advantage of not folding

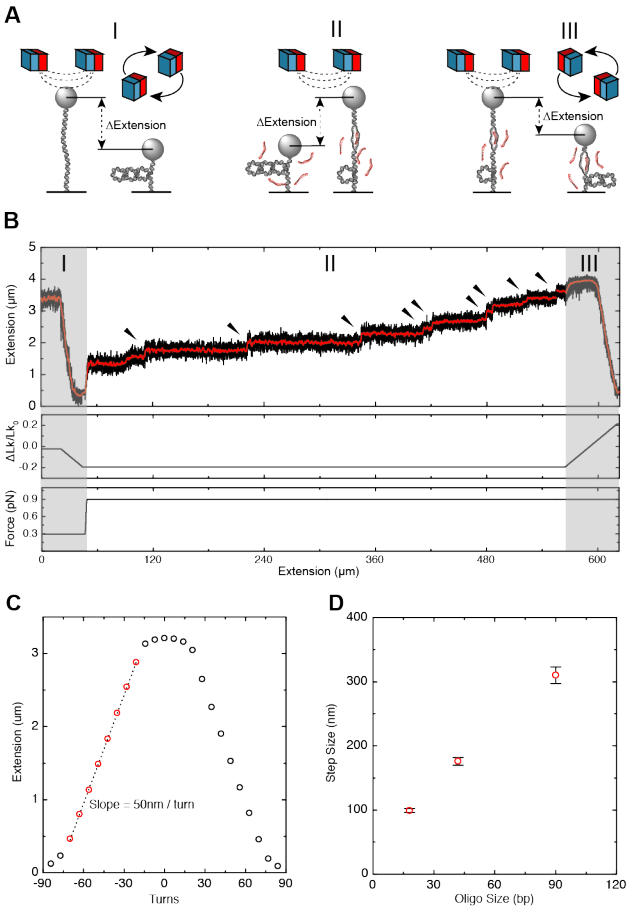

Figure 2. DNA topology based strand invasion assay. (A) Schematic of the experimental setup. First a molecule is negatively supercoiled (I). Spontaneous invasion events are detected by stepwise positive changes in extension (II). The molecule is then positively supercoiled while monitoring the extension (III) The molecule is then pulled at ~10pN to eject the invaded strands. (B) Real time trace of a $(CCCTAA)_7$ strand invasion experiment (reset not shown). (C) Rotation extension curve at 0.9pN. At this force, the rotation extension curve is symmetrical, with a linear regime at negative superhelical density corresponding to 50nm per turn (red). (D) The step size is correlated to the length of the strand used for invasion, consistent with the change in extension being a result of strand invasion events.

into intramolecular GQ structures and therefore simplified our initial experiments. In the presence of 10 nM tel7C we observed discrete steps of increased extension as a function of time as expected (Figure 2B). A collection of time trajectories as shown in Figure 2B were fit with a step finding algorithm[17] to extract the distributions of step sizes and waiting times between discrete stepping events. For the tel7C invading strand the distribution of step sizes is 176 ± 6 nm. Once a DNA molecule buckles and begins to form plectonemic supercoils, subsequent supercoiling results in a linear change in the DNA tether extension, yielding an extension change of 50 nm per turn introduced under our experimental conditions (Figure 2C). Using this value, we would predict that invasion of the 42 nt long tel7C molecule should remove ~ 4 helical turns (42 bases / 10.5 base pairs per turn), which should result in 200 nm steps in the extension signal. The ~10% lower change in extension we observed for the tel7C invasion events may be due to incomplete invasion of the entire oligonucleotide sequence. However, we did find that the mean step size did monotonically change with different length C-rich oligonucleotides (tel3C and tel15C) as expected, supporting the conclusion that the

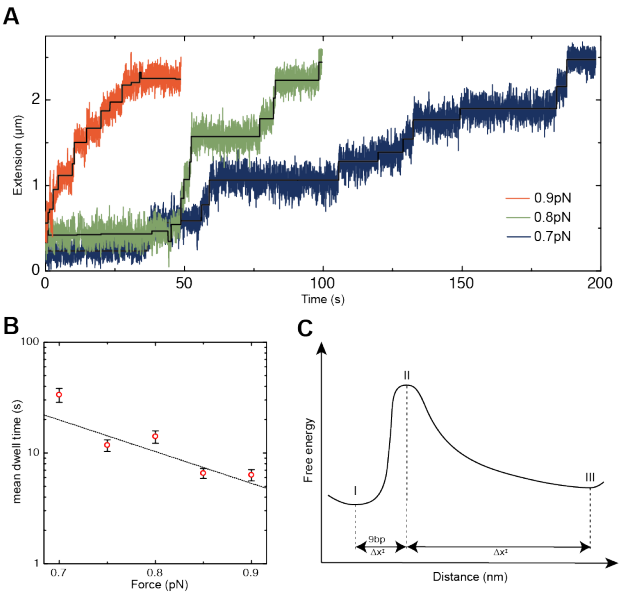

Figure 3. Tel7C invasion kinetics. (A) Time traces of 2μM tel7C strand invasion at 0.7pN (blue), 0.8pN (green) and 0.9pN (red). (B) Mean dwell time between invasion events as a function of torque. Dotted line is a single exponential fit. (C) Energetic landscape of strand invasion. From the exponential fit in figure 3b, we find a 9bp separation between b-form DNA and the transition state along the reaction coordinate to the invaded state.

discrete steps we observed in the real-time strand invasion trajectories correspond to individual oligonucleotides invading the target molecule and forming TDLs.

Formation of TDLs is torque dependent

To gain insight into the energetics of strand invasion for the tel7C strand, we next monitored the torque dependence of the rate of strand invasion by studying the dwell time distributions at a variety of force set points (Figure 3). In our system, the amount of torque (τ) applied locally to the DNA molecule can be approximated by the expression $\tau = (2BF)^{1/2}$, where B is the DNA bending persistence length and F is the applied stretching force[18]. Interestingly, we found the kinetics of strand invasion to be exceedingly torque dependent, which can be seen qualitatively by comparison of representative strand invasion trajectories collected at different stretching forces (Figure 3A). For each of the force set points, a distribution of waiting times between strand invasion events can be measured; the mean dwell time for each experiment was plotted as a function of the applied torque (Figure 3B). This torque-velocity relationship can be modeled using a simple transition state model, given by the expression $k(\tau) = k_o \exp^{-2\Pi n\tau}$, where k_o is the rate constant for the strand invasion process in the absence of applied torque, and n is the characteristic number of base pairs unwound in the target DNA at the transition state for the strand invasion reaction[19]. Fitting the torque-dependence of the kinetics of strand invasion with this simple model yields values of $k_o = 3 \times 10^{-7}\ s^{-1}$ and n = 9 base pairs (Figure 3B and

3C). This analysis indicates that only a small fraction of the 42 nt invading strand is required to base pair with the target DNA to create an effective toe hold for the formation of a D-loop, and in the absence of applied torque the formation of these structures occurs at a vanishingly slow rate.

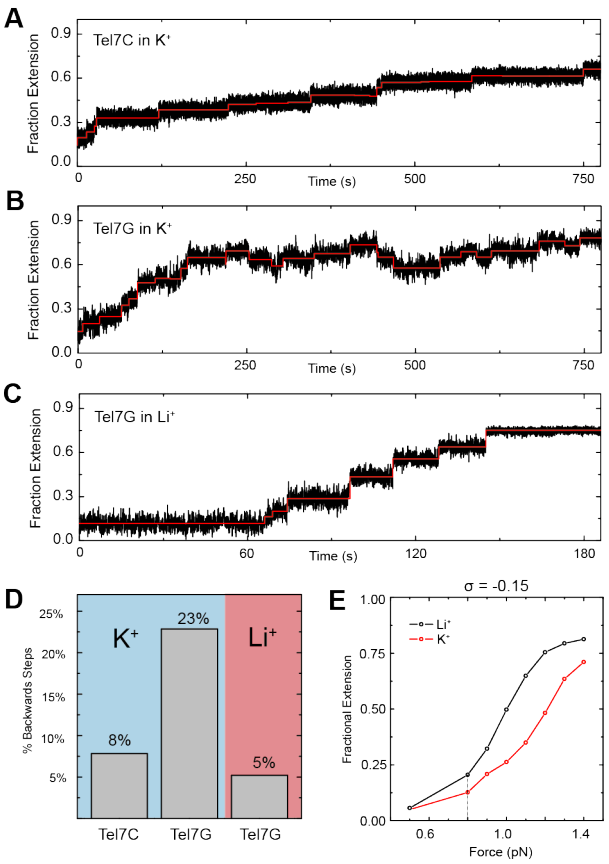

Figure 4. Sequence dependence of strand invasion time trace complexity. (A-C) Telomere invasion time traces. (B) Tel7G invasion time trace. (D) Percentage of backwards steps for tel7C and tel7G, showing increased complexity for the tel7G strand. (E) Fractional extension in Li^+ and K^+ at $\sigma = -0.15$

G-rich telomere DNA exhibits complex structural dynamics during strand invasion

We next set out to investigate differences in the strand invasion dynamics observed for the C-rich tel7C strand as well as the complementary G-rich seven-repeat telomere sequence (tel7G) (Figure 4). Comparison of strand invasion trajectories collected for the tel7C and tel7G invading strands revealed an obvious qualitative difference. Whereas the tel7C invasion trajectory primarily consisted of a stepwise monotonic increase in the observed DNA tether extension as a function of time (Figure 4A), the process for the tel7G invading strand exhibited increased complexity characterized by a higher prevalence of backstepping (Figure 4A vs. Figure 4B). We note that invasion of the

more physiologically relevant tel7G strand generates a telomere D-loop wherein the displaced strand possesses the identical G-rich telomere repeat sequence. Therefore, we reasoned that the increased complexity and backstepping observed in the tel7G strand invasion trajectories may be due in part to the propensity of either the G-rich invading or displaced strand to form GQ structures.

As a further test of this hypothesis, we next changed the buffer conditions to disfavor the stable folding of GQ structures by replacing K^+ with Li^+. Tel7G invasion trajectories collected in the presence of Li^+ displayed two notable features. First, the kinetics of invasion was markedly faster compared to the identical experiment performed in K^+ with the tel7G experiments (Figure 4B vs. 4C). One possible explanation for this observation is that the target DNA duplex is less energetically stable in the presence of Li^+ when compared to K^+, a feature of B-form DNA that, to our knowledge, has not been biophysically characterized. To analyze this possibility, we compared the extension properties of our telomere DNA tethers as a function of superhelical density in both K^+ and Li^+. Indeed, we found that the DNA is more readily denatured by applied torques in the presence of Li^+ (Figure 4D), which provides an explanation for the increased rate of tel7G invasion observed in our experiments. The second salient feature of the tel7G invasion trajectories was the prevalence of back-stepping throughout the invasion process in K+. Unlike the D-loops formed by tel7C strand invasion, the physiologically relevant TDLs formed by tel7G strand invasion have the potential to form GQs in the displaced strand. We can quantify the amount of back-stepping within the invasion trajectories using a step fitting algorithm[17]. We define forward and backward steps as either an increase or decrease in extension in the DNA

tether, respectively. Using this analysis approach for the tel7C strand, we found 8% of the total steps to be backward steps, compared to 23% of the total steps for the tel7G strand (Figure 4E). In contrast, performing the tel7G strand invasion experiment in the presence of Li^+ significantly reduced the probability of backstepping to levels comparable to that observed for the tel7C experiments (Figure 4E). Taken together, these results again support a model wherein GQ folding in the displaced strand of a TDL underlies the complex dynamics and backstepping observed in tel7G and tel7dG strand invasion trajectories in K+ conditions.

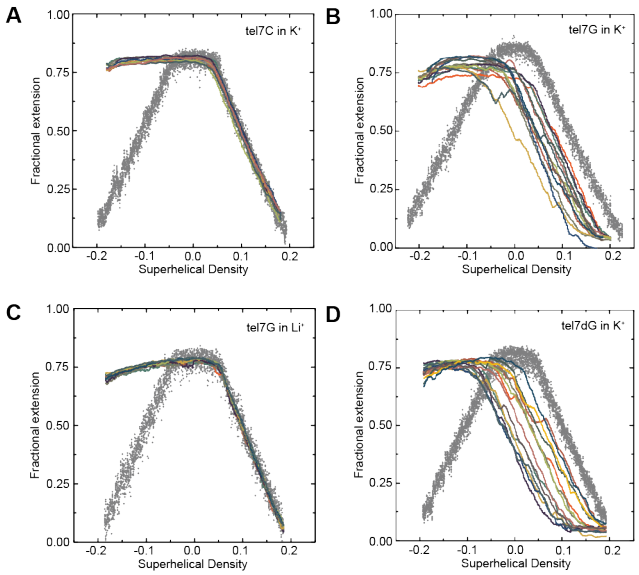

Figure 5. Stable d-loops result in a shift of the rotation extension curve. Invasion traces are in colored lines, rotation extension curves in the absence of invaded strands are in grey dots. (A) Tel7C in K^+. (B) Tel7G in K^+. (C) Tel7G in Li^+. (D) Tel7dG in K^+.

Structural stability of TDLs formed by G-rich strand invasion

If the displaced strand within a TDL formed upon G-rich strand invasion folds into a GQ structure, one prediction is that the TDL will be less energetically favored to resolve since the H-bonds that have been disrupted upon strand invasion are compensated by H-bonds within a GQ fold. As noted above, the stable unwinding of the telomere DNA target during strand invasion results in a change in the overall DNA twist (i.e. the

number of helical turns per unit length of the DNA molecule). Such changes in DNA twist, if structurally stable, can be directly measured as a shift in the rotation-extension curve to the left when the magnets are rotated back toward the relaxed state of the DNA molecule[16]. In contrast, if the invading strands are ejected during the rewinding of the molecule back toward the relaxed state, one would expect to observe a rotation-extension curve that overlays the original pre-invaded state. After complete invasion of a target telomere DNA tether with the tel7C oligonucleotide, the magnets were rotated back toward the relaxed state and into the positive superhelical density regime (Figure 5). Overlay of many independent rotation-extension curves taken following tel7C invasion revealed no shift in the rotation extension curve (Figure 5A), consistent with the notion that as positive turns are being added back to the molecule the C-rich invasion strands are ejected from the molecule and the TDLs are resolved. In contrast, when the same experiment was conducted with the tel7G invading strand, a significant shift in the rotation-extension curve was observed across many independent experimental trials (Figure 5B). This hysteresis in the rotation-extension curve taken on a molecule invaded by the tel7G oligonucleotide is indicative of increased structural stability of TDLs when the physicologically relevant G-rich invading strand is used. Interestingly, when the same experiment was performed with the tel7G strand in the presence of Li^+ rather than K^+, the observed hysteresis in the rotation-extension curve was eliminated (Figure 5C). Given the known destabilizing effect of Li^+ on GQ structures, this result is in close accord with a model wherein GQ folding within the displaced strand of the TDL has an overall stabilizing effect on the structure.

Although our results are consistent with a role for GQ in stabilizing TDL structures formed upon tel7G invasion, it remained a possiblity that the G-rich invading strands in solution were participating in intermolecular GQ formation with the diplaced strand, rather than formation of an intramolecular GQ within the displaced strand of the TDL. To distinguish between these two possibilities, we turned to the use of a modified oligonucleotide wherein the central guanine in the G-track of every other telomere repeat was substituted by a 7-deazaguanine (tel7dG), serving to disrupt the Hoogsteen face of the nucleoside. This modification prevents GQ folding while leaving the Watson-Crick face required for canonical helical basepairing unperturbed[20]. Analysis of DNA tethers following strand invastion by the tel7dG strand again revealed a leftward shift of the rotation-extension curve, consistent with stable TDL formation (Figure 5D). These data lend further support to the notion that intramolecular GQs formed within the displaced strand of TDLs are structurally stabilizing.

DISCUSSION

Magnetic Tweezers (MT) force spectroscopy is a powerful tool with which to probe DNA mechanics[21-22]. MT-based methods have been applied to the study of human telomere DNA in recent years, with a focus on the propensity of this repetitive G-rich sequence $(TTAGGG)_n$ to fold into G-quadruplex (GQ) structures[23-24]. Previously published force spectroscopy analyses of telomere DNA mechanics have largely focused on the structural properties of short single-stranded (ss) model telomere DNA substrates. In the present work, we use a MT system to interrogate the structural properties of long, uninterrupted duplex telomere DNA molecules of physiologically

relevant lengths (> 10 kilobases). We find that duplex telomere DNA has a similar bending persistence length to that of non-repetitive DNA sequence[15]. In contrast, telomere DNA tethers are slightly more torsionally stiff than non-telomere control DNA tethers, requiring greater applied torques to drive the transition to denatured DNA. We hypothesize this effect is due to the absence of large AT-rich regions within the DNA molecule, where the DNA melting transition is conventionally thought to be nucleated.

MT methods have also previously been used to directly monitor DNA strand invasion in real-time, providing a tool to study the mechanics of this essential DNA transaction that occurs during DNA repair and recombination pathways[16, 25]. Here, we have adapted this approach to study strand invasion at telomere DNA target sites, a process proposed to occur during the formation of telomere-loops (T-loops) as well as during the alternative lengthening of telomeres (ALT) pathway[7]. By using telomeric ssDNA probes of various lengths introduced to individual duplex telomere DNA molecules held under precisely applied degrees of superhelical strain, we detect real-time strand invasion and the formation of telomeric displacement-loops (TDLs). Varying the amount of applied torque to the target telomere DNA molecule reveals that formation of TDLs is highly torque dependent. Analysis of the kinetics of strand invasion as a function of applied torque using a simple transition state model[19] suggests ~9 base pairs of the DNA target must be unwound at the transition state along the well-defined strand invasion reaction coordinate. This result supports a previous model for the role of the telomere repeat binding factor 2 protein (TRF2), which has been shown to wrap duplex telomere DNA in a chiral fashion, resulting in the application of negative superhelical strain and promoting T-loop formation[26].

Interestingly, we observe complex invasion dynamics when the invasion trajectories are collected in the presence of a G-rich ssDNA oligonucleotide, intended to model the G-rich 3' ssDNA tail that exists at endogenous telomere ends. The invasion dynamics are characterized by a combination of forward and reverse steps, and these back steps are suppressed when performing the same experiments with the complementary C-rich strand or in the presence of Li^+ rather than K^+ ions. It is well established that Li^+ has a destabilizing effect on GQ folding[10]. We also provide evidence that TDLs formed upon G-rich strand invasion in the presence of K^+ are more energetically stable than when formed in the presence of Li^+ or with the C-rich strand. Taken together, these results lead to a model wherein the formation of a TDL upon invasion of the G-rich ssDNA tail permits the G-rich displaced strand to fold into a GQ structure. While it is well documented that single-stranded telomere DNA substrates fold into GQ structures *in vitro*[10], the prevalence of this structure at telomeres and elsewhere within the genome has been the subject of debate[12]. Our results suggest the process of strand invasion at telomere DNA targets may provide an opportunity for GQ structures to fold *in vivo*.

The system we describe in the present study provides a powerful experimental platform for future studies of strand invasion at telomere DNA targets. For example, single-molecule studies using this system can be designed to understand the molecular mechanisms of telomere-associated proteins and enzymes known to resolve D-loop and GQ structures[27-29]. Moreover, our novel system can be employed to directly study the mechanism of GQ-binding compounds and their possible role in

stabilizing TDLs[30]. Lastly, recent studies have shown that telomeres, long thought to be transcriptionally silent, are transcribed to generate long non-coding Telomere repeat-containing RNA (TERRA)[31]. TERRA is implicated in regulating various aspects of telomere biology and is proposed to do so through the formation of RNA-loops (R-loops) at telomeres[32]. Future work utilizing our novel MT-based assay will also focus on the mechanical properties of telomeric R-loops and the molecular mechanism of TERRA-mediated regulation of telomere function.

.

REFERENCES

1. Palm, W.; de Lange, T., How shelterin protects mammalian telomeres. *Annu Rev Genet* **2008,** *42*, 301-34.

2. Hastie, N. D.; Dempster, M.; Dunlop, M. G.; Thompson, A. M.; Green, D. K.; Allshire, R. C., Telomere reduction in human colorectal carcinoma and with ageing. *Nature* **1990,** *346* (6287), 866-8.

3. Makarov, V. L.; Hirose, Y.; Langmore, J. P., Long G tails at both ends of human chromosomes suggest a C strand degradation mechanism for telomere shortening. *Cell* **1997,** *88* (5), 657-66.

4. Prelich, G.; Stillman, B., Coordinated leading and lagging strand synthesis during SV40 DNA replication in vitro requires PCNA. *Cell* **1988,** *53* (1), 117-26.

5. Hayflick, L.; Moorhead, P. S., The serial cultivation of human diploid cell strains. *Exp Cell Res* **1961,** *25*, 585-621.

6. Nguyen, T. H. D.; Tam, J.; Wu, R. A.; Greber, B. J.; Toso, D.; Nogales, E.; Collins, K., Cryo-EM structure of substrate-bound human telomerase holoenzyme. *Nature* **2018,** *557* (7704), 190-195.

7. Zhang, J. M.; Yadav, T.; Ouyang, J.; Lan, L.; Zou, L., Alternative Lengthening of Telomeres through Two Distinct Break-Induced Replication Pathways. *Cell Rep* **2019,** *26* (4), 955-968 e3.

8. Greider, C. W., Telomeres do D-loop-T-loop. *Cell* **1999,** *97* (4), 419-22.

9. Zhao, Y.; Sfeir, A. J.; Zou, Y.; Buseman, C. M.; Chow, T. T.; Shay, J. W.; Wright, W. E., Telomere extension occurs at most chromosome ends and is uncoupled from fill-in in human cancer cells. *Cell* **2009,** *138* (3), 463-75.

10. Lane, A. N.; Chaires, J. B.; Gray, R. D.; Trent, J. O., Stability and kinetics of G-quadruplex structures. *Nucleic Acids Res* **2008,** *36* (17), 5482-515.

11. Lee, J. Y.; Yoon, J.; Kihm, H. W.; Kim, D. S., Structural diversity and extreme stability of unimolecular Oxytricha nova telomeric G-quadruplex. *Biochemistry* **2008,** *47* (11), 3389-96.

12. Huppert, J. L.; Balasubramanian, S., Prevalence of quadruplexes in the human genome. *Nucleic Acids Res* **2005,** *33* (9), 2908-16.

13. Balasubramanian, S.; Neidle, S., G-quadruplex nucleic acids as therapeutic targets. *Curr Opin Chem Biol* **2009,** *13* (3), 345-53.

14. Stansel, R. M.; de Lange, T.; Griffith, J. D., T-loop assembly in vitro involves binding of TRF2 near the 3' telomeric overhang. *EMBO J* **2001,** *20* (19), 5532-40.

15. Bustamante, C.; Marko, J. F.; Siggia, E. D.; Smith, S., Entropic elasticity of lambda-phage DNA. *Science* **1994,** *265* (5178), 1599-600.

16. Strick, T. R.; Croquette, V.; Bensimon, D., Homologous pairing in stretched supercoiled DNA. *Proc Natl Acad Sci U S A* **1998,** *95* (18), 10579-83.

17. Kerssemakers, J. W.; Munteanu, E. L.; Laan, L.; Noetzel, T. L.; Janson, M. E.; Dogterom, M., Assembly dynamics of microtubules at molecular resolution. *Nature* **2006,** *442* (7103), 709-12.

18. Strick, T.; Allemand, J.; Croquette, V.; Bensimon, D., Twisting and stretching single DNA molecules. *Prog Biophys Mol Biol* **2000,** *74* (1-2), 115-40.

19. Ramreddy, T.; Sachidanandam, R.; Strick, T. R., Real-time detection of cruciform extrusion by single-molecule DNA nanomanipulation. *Nucleic Acids Res* **2011,** *39* (10), 4275-83.

20. Masai, H.; Kakusho, N.; Fukatsu, R.; Ma, Y.; Iida, K.; Kanoh, Y.; Nagasawa, K., Molecular architecture of G-quadruplex structures generated on duplex Rif1-binding sequences. *J Biol Chem* **2018,** *293* (44), 17033-17049.

21. Yu, Z.; Dulin, D.; Cnossen, J.; Kober, M.; van Oene, M. M.; Ordu, O.; Berghuis, B. A.; Hensgens, T.; Lipfert, J.; Dekker, N. H., A force calibration standard for magnetic tweezers. *Rev Sci Instrum* **2014,** *85* (12), 123114.

22. Long, X.; Parks, J. W.; Stone, M. D., Integrated magnetic tweezers and single-molecule FRET for investigating the mechanical properties of nucleic acid. *Methods* **2016,** *105*, 16-25.

23. You, H.; Le, S.; Chen, H.; Qin, L.; Yan, J., Single-molecule Manipulation of G-quadruplexes by Magnetic Tweezers. *J Vis Exp* **2017,** (127).

24. Lin, J.; Kaur, P.; Countryman, P.; Opresko, P. L.; Wang, H., Unraveling secrets of telomeres: one molecule at a time. *DNA Repair (Amst)* **2014,** *20*, 142-153.

25. Lee, M.; Lipfert, J.; Sanchez, H.; Wyman, C.; Dekker, N. H., Structural and torsional properties of the RAD51-dsDNA nucleoprotein filament. *Nucleic Acids Res* **2013,** *41* (14), 7023-30.

26. Benarroch-Popivker, D.; Pisano, S.; Mendez-Bermudez, A.; Lototska, L.; Kaur, P.; Bauwens, S.; Djerbi, N.; Latrick, C. M.; Fraisier, V.; Pei, B.; Gay, A.; Jaune, E.; Foucher, K.; Cherfils-Vicini, J.; Aeby, E.; Miron, S.; Londono-Vallejo, A.; Ye, J.; Le Du, M. H.; Wang, H.; Gilson, E.; Giraud-Panis, M. J., TRF2-Mediated Control of Telomere DNA Topology as a Mechanism for Chromosome-End Protection. *Mol Cell* **2016,** *61* (2), 274-86.

27. Wu, Y.; Shin-ya, K.; Brosh, R. M., Jr., FANCJ helicase defective in Fanconia anemia and breast cancer unwinds G-quadruplex DNA to defend genomic stability. *Mol Cell Biol* **2008,** *28* (12), 4116-28.

28. Budhathoki, J. B.; Maleki, P.; Roy, W. A.; Janscak, P.; Yodh, J. G.; Balci, H., A Comparative Study of G-Quadruplex Unfolding and DNA Reeling Activities of Human RECQ5 Helicase. *Biophys J* **2016,** *110* (12), 2585-2596.

29. Tippana, R.; Hwang, H.; Opresko, P. L.; Bohr, V. A.; Myong, S., Single-molecule imaging reveals a common mechanism shared by G-quadruplex-resolving helicases. *Proc Natl Acad Sci U S A* **2016,** *113* (30), 8448-53.

30. Tan, J.; Lan, L., The DNA secondary structures at telomeres and genome instability. *Cell Biosci* **2020,** *10*, 47.

31. Azzalin, C. M.; Reichenbach, P.; Khoriauli, L.; Giulotto, E.; Lingner, J., Telomeric repeat containing RNA and RNA surveillance factors at mammalian chromosome ends. *Science* **2007,** *318* (5851), 798-801.

32. Oliva-Rico, D.; Herrera, L. A., Regulated expression of the lncRNA TERRA and its impact on telomere biology. *Mech Ageing Dev* **2017,** *167*, 16-23.

CHAPTER III

TELOMERE DNA G-QUADRUPLEX FOLDING WITHIN ACTIVELY EXTENDING HUMAN TELOMERASE

Linnea I. Jansson[1*], Jendrik Hentschel[2*], Joseph W. Parks[3], Terren R. Chang[2], Cheng Lu[4], Rishika Baral[2], Clive R. Bagshaw[2], Michael D. Stone[2]

[1]Molecular, Cell and Developmental Biology Department, University of California Santa Cruz, CA 95064, [2]Chemistry and Biochemistry Department, University of California Santa Cruz, CA 95064, [3]Invitae, CA 94103. [4]Department of Protein Chemistry, Genentech Inc., CA 94080

[*] authors contributed equally

Originally published in PNAS April 2019

ABSTRACT

Telomerase reverse transcribes short G-rich DNA repeat sequences from its internal RNA template to maintain telomere length. G-rich telomere DNA repeats readily fold into G-quadruplex (GQ) structures *in vitro* and the presence of GQ-prone sequences throughout the genome introduces challenges to replication *in vivo*. Using a combination of ensemble and single-molecule telomerase assays, we discovered that GQ folding of the nascent DNA product during processive addition of multiple telomere repeats modulates the kinetics of telomerase catalysis and dissociation. Telomerase reactions performed with telomere DNA primers of varying sequence or using GQ-stabilizing K^+ versus GQ-destabilizing Li^+ salts yielded changes in DNA product profiles consistent with formation of GQ structures within the telomerase-DNA complex. Addition of the telomerase processivity factor POT1-TPP1 altered the DNA product profile, but was not sufficient to recover full activity in the presence of Li^+ cations. This result suggests GQ folding synergizes with POT1-TPP1 to support telomerase function. Single-molecule FRET experiments reveal complex DNA structural dynamics during real-time catalysis in the presence of K^+ but not Li^+, supporting the notion of nascent product folding within the active telomerase complex. To explain the observed distributions of telomere products, we globally fit telomerase time series data to a kinetic model that converges to a set of rate constants describing each successive telomere repeat addition cycle. Our results highlight the potential influence of the intrinsic folding properties of telomere DNA during telomerase

catalysis and provide a detailed characterization of GQ modulation of polymerase function.

SIGNIFICANCE

Telomeres protect the ends of linear chromosomes from illicit DNA processing events that threaten genome stability. Guanine-rich telomere DNA repeat sequences are protected by telomere-binding proteins, and are also prone to fold into structures called G-quadruplexes (GQs). In highly proliferative cells, including the majority of human cancers, telomeres are maintained by the telomerase enzyme. Thus, telomerase and its telomere DNA substrates represent important targets for developing novel cancer drugs. The results of this study suggest GQ folding of newly synthesized DNA may occur within an actively extending telomerase enzyme. Our experiments highlight the importance of telomere DNA structure during the function of telomerase and its associated telomere-binding proteins.

INTRODUCTION

Telomeres safeguard the ends of chromosomes from illicit DNA processing events that would otherwise threaten genome stability (1, 2). The foundation of telomere structure consists of short G-rich DNA sequence repeats. The majority of mammalian telomeric DNA is double-stranded and can be up to several kilobases in length, whereas telomere ends are processed to terminate with a 3′ single-stranded G-rich

overhang (~50-500 nucleotides in length) (3, 4). Repetitive G-rich DNA sequences are not unique to telomeres and are found throughout the human genome (5). These G-rich repeats have the capacity to fold into G-quadruplex (GQ) structures composed of multiple Hoogsteen bonded G-quartet motifs that stack together to yield stable DNA folds (6, 7). GQ folding has been implicated in a variety of biological processes. For example, replication of GQ-prone sequences is problematic and requires contributions from specific DNA helicase enzymes to avoid replication-coupled DNA damage (8-10). Sequences with GQ-folding potential are enriched within promoter sequences of oncogenes where they are thought to regulate gene expression (11). Finally, recent evidence suggests GQ folds can form *in vivo* in a spatially and temporally regulated manner (12-14). Thus, small molecules that bind and stabilize GQ-folds hold promise as novel cancer drugs, which motivates better understanding of how GQ structure can modulate enzyme function.

Telomerase is an RNA-dependent DNA polymerase that is uniquely adapted to synthesizing G-rich repetitive DNA sequences (15, 16). Telomerase activity combats gradual telomere shortening that occurs with each round of cellular division (17). While telomere shortening induces senescence or cell death in somatic tissues, highly proliferative cells such as stem cells rely upon telomerase activity to maintain telomeres in order to support continued rounds of cell division (15). Genetically inherited hypomorphic mutations in telomerase subunits cause human disorders characterized by deterioration of proliferative tissue types (18-21). In contrast, telomerase overexpression contributes to the immortal phenotype of ~90% of human

cancers, and is therefore an important target for development of novel cancer therapies (22).

Telomerase is a ribonucleoprotein (RNP) complex that includes the long non-coding telomerase RNA (TR) and the catalytic telomerase reverse transcriptase (TERT) protein subunit (23, 24). To initiate telomerase catalysis, the 3′ ssDNA telomeric tail base pairs with the TR template, forming a short RNA-DNA hybrid that is extended in the TERT active site (Fig. 1A). TERT utilizes a limited region of TR to direct synthesis of a defined telomere DNA repeat sequence (GGTTAG in human) with an associated rate constant k_{pol} (Fig. 1A). A unique property of telomerase is the ability to translocate on the DNA product (k_{trans}) in order to recycle the integral TR template during processive addition of multiple telomere repeats prior to dissociation from the DNA product (k_{off}) (Fig. 1A) (25). This repeat addition processivity (RAP) implicitly requires multiple points of contact between telomerase and its DNA substrate, a notion that is consistent with data from a variety of telomerase systems identifying ‘anchor site’ DNA interactions. Anchor site interactions have been attributed to the TERT essential N-terminal (TEN) domain (26-31), a specific DNA-retention site near the TERT active site (32), as well as elements of the TR subunit itself (26-31, 33). Although the minimal telomerase RNP exhibits RAP, components of the telomere-associated shelterin complex can further enhance enzyme processivity. Specifically, the protection of telomeres 1 (POT1) protein binds to single-stranded telomeric DNA and together with its heterodimeric binding partner, telomere protection protein 1 (TPP1), is sufficient to enhance telomerase processivity *in vitro* (34). POT1-TPP1 is further required for telomerase recruitment to telomeres *in vivo* (35).

Model telomere DNA substrates harboring integer multiples of four consecutive telomere repeats are inefficient binding substrates for telomerase *in vitro* while DNA primers with five, six, or seven consecutive repeats are efficiently bound and extended (36). Thus, while GQ structures can inhibit telomerase association (36, 37), the presence of a small single-stranded DNA overhang in the substrate appears sufficient to recover telomerase loading and function. While these previous findings illuminate DNA sequence determinants that mediate the initial binding of telomerase to its substrate, there remained an untested possibility that GQ structure may influence the behavior of an actively extending human telomerase-DNA complex, as was suggested by early studies of telomerase (38-40). Notably, the POT1-TPP1 heterodimer that decorates the G-overhang of human telomeres resolves GQ structures *in vitro* through sequence specific binding of the two POT1 oligonucleotide binding (OB) fold domains (41-43). However, it remains unclear if POT1-TPP1 rapidly binds to newly synthesized DNA repeats to efficiently *prevent* the formation of GQs, or if POT1-TPP1 *resolves* GQs that form within the telomerase-telomere complex.

To study the relationship between DNA structure and human telomerase catalysis, we performed direct primer extension assays using dNTP concentrations similar to those found in the cellular environment (44). Our experiments reveal a complex pattern of telomerase DNA product accumulation that indicates the efficiency of template recycling is dependent upon the number of synthesized repeats. Experiments using telomere DNA primers of varying sequence and salt conditions support the notion that a GQ can form within the telomerase-DNA complex. The addition of the POT1-TPP1

processivity factor alters the telomerase product profile, but does not rescue full DNA synthesis rates under GQ-destabilizing conditions. To estimate individual rate constants for successive repeat addition cycles, we performed global kinetic modeling of telomerase time-series data. Interestingly, our model converges to a unique solution of rate constants that provides a direct measure of processivity for each cycle of telomere repeat addition. Single-molecule FRET experiments reveal DNA structural dynamics during telomerase catalysis, supporting the notion that telomere DNA GQ folding modulates enzyme function. We present a working mechanistic model that provides a framework for understanding the delicate interplay of telomere DNA product folding and POT1-TPP1 during telomerase catalysis.

RESULTS

Telomerase product distribution is sensitive to dNTP concentrations and stoichiometry

When measuring telomerase activity *in vitro*, it is common to employ direct primer extension assays in the presence of [α^{32}P]dGTP. This approach permits reactions to be performed with a large excess of unlabeled DNA substrate, benefits from very high sensitivity of product detection, and circumvents PCR-induced artifacts inherent to the telomere repeat amplification protocol (TRAP) assay. However, the use of [α^{32}P]dGTP incorporation to detect product accumulation limits the amount of total dGTP that can be used in the assay, leading to the widely reported practice of using non-physiological

dNTP stoichiometry that has the potential to significantly alter the telomerase product distribution (40, 45). To circumvent this problem, we used 5′ radiolabeled DNA primers and cold dNTPs to monitor telomerase activity (Fig. 1B). For most experiments conducted in the present study, telomerase was reconstituted *in vitro* using a previously reported two-piece RNA strategy (hTR 32-195 and hTR 239-328) in commercially available rabbit reticulocyte lysates (RRL) (46, 47). The primary motivation for utilizing enzyme prepared in this manner is to facilitate direct comparison of biochemical data with results from single-molecule experiments, which require the use of the two-piece RNA system to permit site-specific modification of hTR (48) (see Methods and Results below). Importantly, enzymes prepared in RRL with the two-piece RNA approach exhibit catalytic properties that are comparable to telomerase enzyme assembled with full-length hTR in HEK293T cells (Fig. S1). We compared the results using 5′ end-labeled primers to standard assays performed with α^{32}P-dGTP using identical dNTP and primer concentrations (Fig. S2). Although the reaction profiles are qualitatively distinct, we observed quantitatively similar product

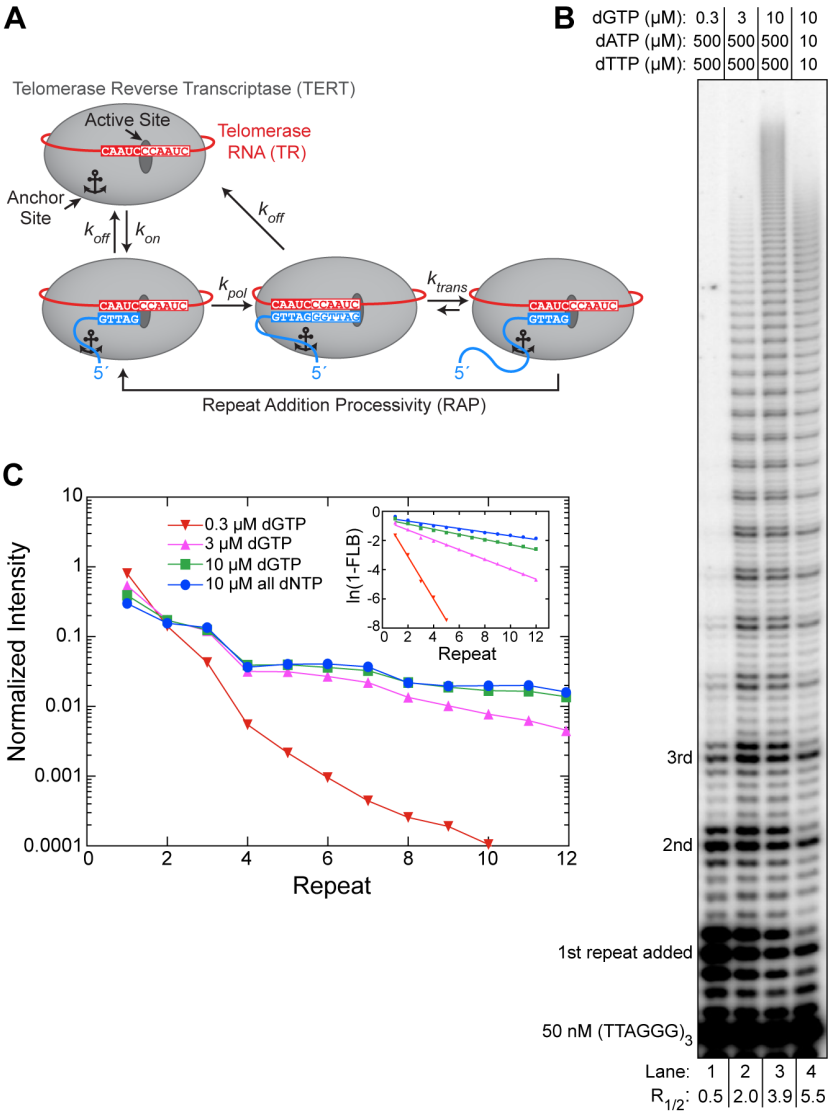

Figure 1. Human telomerase function. (A) Telomerase catalytic cycle. TERT and TR are shown simplified in grey and red, respectively. The telomere DNA is shown in blue and the telomerase anchor site is schematically represented by a dashed circle. k_{off} and k_{on} represent the rate constants for dissociation from and annealing to the telomere, respectively. The rate constant for nucleotide addition during repeat synthesis is represented by k_{pol} and the translocation rate constant after the completion of each repeat is represented by k_{trans}. The rate constants governing nucleotide addition and translocation together define Repeat Addition Processivity (RAP). (B) Telomerase primer extension assay with 50 nM ^{32}P-end-labeled $(TTAGGG)_3$ primer. Nucleotide concentrations are indicated above the gel and repeats added to the $(TTAGGG)_3$ primer are indicated on the left. The $R_{1/2}$ values are shown at the bottom of the gel. (C) Normalized gel band intensity (see B) plotted as a function of repeat number. Inset, FLB (fraction left behind) was calculated by dividing the sum of each RAP band and all bands below by the total intensity of a given lane. The plot of ln(1-FLB) over repeat number was used to calculate $R_{1/2}$ processivity values (B).

incorporation. Importantly, the majority of the input DNA primers are not extended in our experiments, demonstrating our reaction conditions are sufficient to limit distributive telomerase activity (i.e. an individual primer being extended by multiple telomerase enzymes). Such processive telomerase activity is also evident when analyzing pulse-chase experiments in which longer DNA products continue to accumulate after addition of a 400-fold excess of cold DNA primer (Fig. S3).

Having established that our end-labeled DNA primer assay is capable of accurately monitoring processive telomerase action, we next sought to analyze the influence of varying dNTP concentrations on the telomerase product distribution (Fig. 1B). Previous studies have defined telomerase processivity as the number of repeats corresponding to the point where the dissociated DNA represents 50% of the total population (i.e. median product length, $R_{1/2}$) (34, 49) (see Supplementary text). This number can be determined by fitting a linear regression to a plot of ln(1-FLB) versus repeat number, where FLB is the fraction left behind (Fig. 1C inset, see Methods). Titrating increasing amounts of dGTP in the presence of a large excess of dATP and dTTP yields a significant boost in RAP, as has been reported previously for both human and *Tetrahymena* telomerase (Fig. 1B and 1C) (32, 40, 50-53). However, the use of a large excess of dATP and dTTP is not a good approximation for the physiological dNTP pool which is generally closer to the ~10 μM range (44). When assayed in the presence of equimolar dGTP, dATP, and dTTP, we observe the highest RAP of all conditions tested (Fig. 1B, lane 4 and Fig. 1C). Hence, we elected to perform all subsequent telomerase assays in our study under these optimized conditions of equimolar dNTPs.

G-quadruplex folding varies the pattern of telomerase product accumulation

Established methods for approximating RAP processivity using the $R_{1/2}$ value described above assume an exponential decay in the distribution of accumulated telomerase product lengths with each telomere repeat added (34, 37, 49). In other words, the $R_{1/2}$ value represents a weighted average processivity which is convenient for semi-quantitative comparisons, but may mask underlying heterogeneity in the microscopic processivity associated with individual steps (see Supplementary text). Indeed, we noted the appearance of plateaus in the product distribution when using equimolar concentrations of dNTPs in the end-labeled DNA primer extension assay (Fig. 1C and 2). For example, when using a standard telomere DNA primer composed of the sequence $(TTAGGG)_3$, we observed a sudden drop in product accumulation between the bands corresponding to the third and fourth telomere repeat added to the primer (Fig. 2A, lane 1, red asterisk). Further, the intensities of the subsequent four added repeats were approximately equal, until a second decrease in accumulation occurred between added repeats seven and eight (Fig. 2A). This pattern of four equally populated product lengths, followed by a decrease in accumulation, continued throughout the detectable range of telomere DNA products.

Telomere DNA primers with at least four contiguous G-rich repeats can fold into a G-quadruplex (GQ) *in vitro* (54, 55), suggesting the observed RAP-associated 'pattern of

four' may be due to GQ folding of the DNA product within an actively extending telomerase complex. To test this hypothesis, we altered the 5′ end of the telomere DNA sequence so that it no longer harbored the requisite run of guanines needed to participate in GQ folding (Fig. 2A, lanes 2 and 3). Altering the primer in this way should change the product length where the 'pattern of four' appears once the newly synthesized DNA folds into a GQ. Indeed, a modified DNA primer with a 5′ $(TG)_3$ substitution supported telomerase RAP, but the plateaus in the product profile were delayed by one additional repeat, corresponding to the sequence needed to promote GQ formation in the product DNA (Fig. 2A, compare lanes 1 and 2). Similarly, when the first two repeats in the telomere DNA primer were substituted with a $(TG)_6$ dinucleotide repeat sequence, the

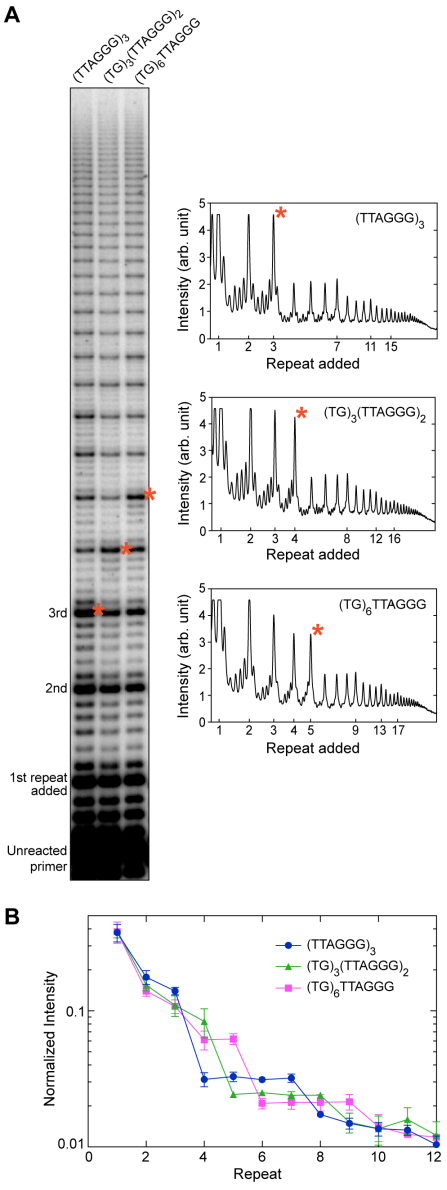

Figure 2. The telomerase product distribution profile varies with the number of consecutive TTAGGG DNA repeats. (A) Telomerase primer extension assay with primers of varying TTAGGG composition. Primer variants are indicated at the top of the gel. Repeats added to the primer are indicated to the left. Lane profiles with raw intensity versus added repeat are shown for each primer variant at right. Corresponding bands between the gel and lane profiles are indicated by a red asterisk. (B) Gel band intensities were normalized to the total counts in each lane and are plotted as a fraction of the total counts versus repeat number. Data plotted represent the mean values from three independent experiments and error bars are the standard deviation.

plateaus were delayed by two additional repeats (Fig. 2A, compare lanes 1 and 3). These results were highly reproducible across three independent experimental trials (Fig. 2B) and support the hypothesis that GQ folding within the nascent telomere DNA causes the telomerase product profile to deviate from a uniformly decreasing decay.

POT1-TPP1 alters the telomere DNA product distribution

The POT1-TPP1 heterodimer simultaneously binds to telomerase via the TEL-patch interaction between the TERT TEN domain and TPP1 (56). In addition, the POT1-subunit binds single-stranded telomeric DNA to provide additional 'anchor site' contacts that serve to promote telomerase RAP (34). POT1-TPP1 also binds and resolves telomere DNA GQ structures *in vitro* (42). To further evaluate GQ folding within the telomerase complex, we performed

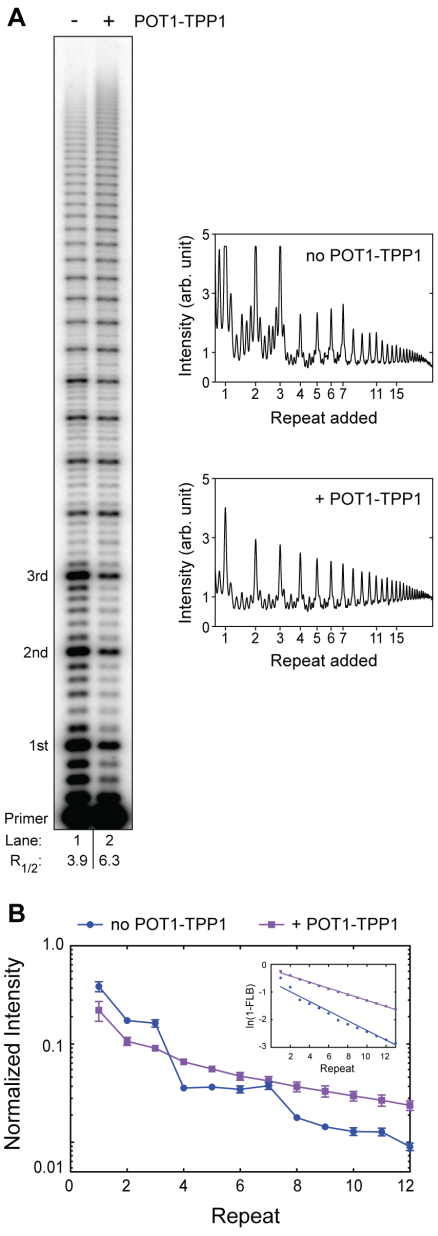

Figure 3. POT1-TPP1 alters the telomerase product distribution profile. (A) Telomerase primer extension assay in absence and presence of POT1-TPP1. Number of added repeats are indicated to the left. The $R_{1/2}$ values are shown at the bottom of the gel. At right, corresponding lane profiles with raw gel band intensities plotted over added repeats. (B) Gel band intensities in the absence (blue squares) or presence (purple squares) of POT1-TPP1 were normalized to the total counts in each lane and plotted as a fraction of the total counts versus repeat number. Data plotted represent the mean values from three independent experiments and error bars are the standard deviation. Inset, the plot of ln(1-FLB) over repeat number was used to calculate $R_{1/2}$ processivity values shown in (A).

primer extension assays in absence and presence of POT1-TPP1 (Fig. 3). In addition to the expected enhancement of RAP, the presence of POT1-TPP1 abolished the four-repeat pattern in the distribution of telomerase products, which instead decay in a uniformly decreasing manner (Fig. 3). Notably, the effects of POT1-TPP1 on the DNA product distribution were the same for both the two-piece hTR reconstituted system and for endogenously reconstituted telomerase preparations from HEK293T cells (Fig. S1). The effect of POT1-TPP1 on the telomere DNA product distribution is consistent with the ability of POT1-TPP1 to bind and remodel the nascent DNA product during active telomere extension. However, this result does not strictly differentiate between the possibilities of POT1-TPP1 *preventing* versus *resolving* a telomere GQ fold within the context of an actively extending telomerase complex.

Destabilization of G-quadruplexes by Li^+ cations slows telomere repeat synthesis

To ultimately address the question of whether GQ folding might impact telomerase function also in the presence of POT1-TPP1, we next set out to characterize the catalytic properties of telomerase under varying cation conditions. The H-bonding configuration of the G-quartet motifs within a GQ fold are differentially stabilized by coordination of specific monovalent cations, with a rank order of $K^+ > Na^+ > Li^+$ in terms of degree of stabilization (57). We observed robust telomerase activity in direct primer extension assays in all cation conditions tested (Fig. 4A). Interestingly, we did not observe the 'pattern of four' RAP product distribution in the presence of Li^+ (Fig. 4A and 4B), the cation condition expected to least stabilize GQ folding during telomerase

catalysis. This effect is most clearly evident when comparing the changes in band intensity between repeats 3-4 and 7-8 (Fig. 4C). Further, there was a clear reduction in total product accumulation in Li^+ when compared to Na^+ and K^+ (Fig. 4A). The lower total product accumulation in the presence of Li^+ was a consequence of slower overall DNA synthesis kinetics as is evident from primer extension time-course experiments

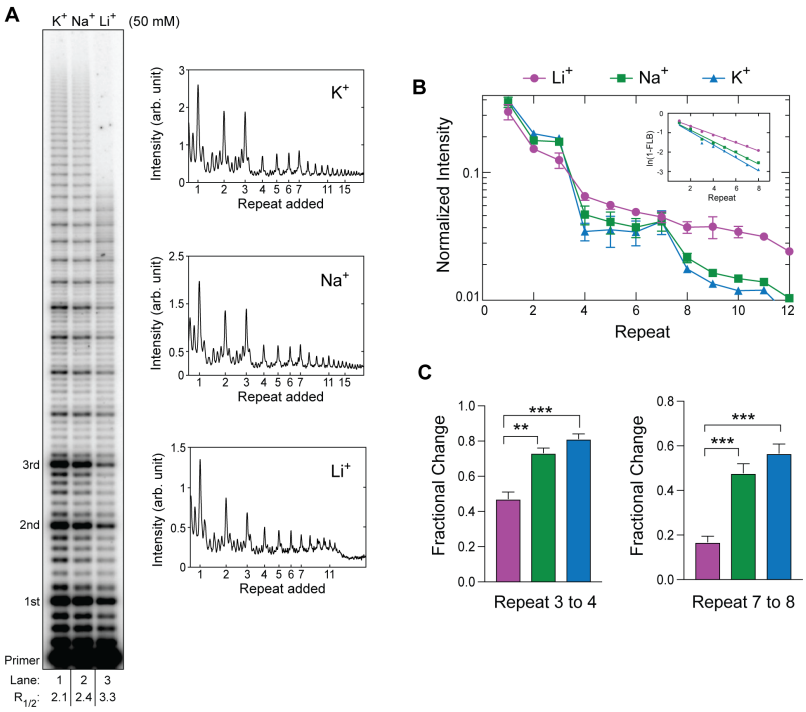

Figure 4. The telomerase product distribution profile depends on monovalent cation identity. (A) Telomerase primer extension assays in presence of different monovalent cations. Repeats added to the primer are indicated to the left. The $R_{1/2}$ values are shown at the bottom of the gel. Lane profiles with raw intensity versus repeat band for each lane are shown on the right. (B) Gel band intensities from experiments in KCl (green triangles), NaCl (blue squares), and LiCl (red circles) were normalized to the total counts in each lane and are plotted as a fraction of the total counts versus repeat number. Data plotted represent the mean values from three independent experiments and error bars are the standard deviation. Inset, the plot of ln(1-FLB) over repeat number was used to calculate $R_{1/2}$ processivity values shown in (A). (C) Statistical analysis of fractional change in band intensities between repeats 3 to 4 (left) or 7 to 8 (right). Error bars represent the standard deviation of experiments performed in triplicate (see B). P values were calculated using a Welch's t test and ***, $p < 0.001$; **, $p < 0.01$.

(Fig. S4). This observation is not completely unexpected based on reported effects of Li^+ on thermophilic DNA polymerases in the polymerase-chain reaction that describe slowed nucleotide incorporation (58). In our telomerase assays, such a general synthesis defect in Li^+ should manifest as increased

NAP (nucleotide-addition processivity) band intensities since each nucleotide incorporation would make a larger contribution to the overall kinetics of each RAP cycle. Consistent with this notion, we observe an up to 2-fold increase in the ratio of NAP:RAP bands when comparing the product distributions in Li^+ versus K^+. However, in both cation conditions the RAP products remain the most populated species across the gel (Fig. 4A), indicating that the catalytic sub-step(s) associated with product translocation and product re-priming remain rate-limiting during RAP. These results demonstrate that GQ-destabilization in the presence of Li^+ negatively impacts the rate, and hence, product yield of telomeric repeat synthesis.

POT1-TPP1 does not rescue DNA-synthesis rates in GQ-destabilizing conditions

We next leveraged the ability to tune the degree of GQ-stabilization in our telomerase assays in order to dissect the potential influence of nascent DNA product folding in the presence of POT1-TPP1. To this end, we performed time-course telomerase primer extension assays using the established K^+ and Li^+ conditions in absence or presence of POT1-TPP1 (Fig. 5). We reasoned if POT1-TPP1 acts by preventing GQ formation in nascent telomere DNA, then GQ destabilization in the presence of Li^+ should not impact POT1-TPP1 enhancement of telomerase catalysis. Conversely, if GQ folding must occur in the presence of POT1-TPP1, then reduced DNA-synthesis rates under

GQ-destabilizing conditions should not be rescued by POT1-TPP1 addition. As expected, primer extension reactions in both K^+ and Li^+ in the presence of POT1-TPP1 exhibited stimulated processivity and lacked the pattern of four in product accumulation (Fig. 5). These results indicate that POT1-TPP1 can productively bind to the nascent product DNA and the telomerase enzyme in both cation conditions. Interestingly, POT1-TPP1 selectively failed to stimulate DNA-synthesis rates in the presence of Li^+ (Fig. 5A, lanes 11 and 14 versus lanes 4 and 7). This result lends unanticipated support to the functional contribution of GQ

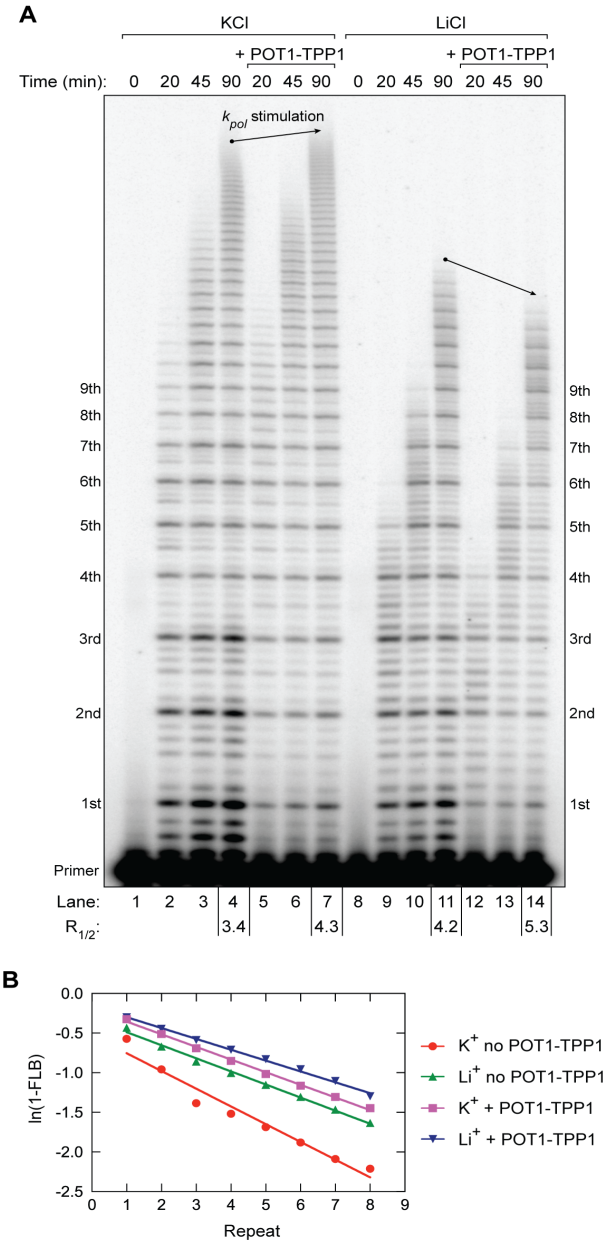

Figure 5. POT1-TPP1 does not enhance telomerase catalysis rates in GQ-destabilizing conditions. (A) Telomerase primer extension time-course assay in absence and presence of POT1-TPP1, and under differential cation conditions. Time points of the reactions are indicated above the gel. POT1-TPP1-dependent differences in the maximum product length at 90 minutes reaction time (i.e. differences in synthesis rate) are indicated by arrows. $R_{1/2}$ processivity values are given for reaction end points below the gel. (B) The plot of ln(1-FLB) over repeat number was used to calculate $R_{1/2}$ processivity values (A)

folding for the POT1-TPP1-telomerase complex, and suggests that POT1-TPP1 may resolve, rather than prevent formation of transient GQ structures within the actively extending enzyme complex (see Discussion for details).

Changes in reaction rate constants govern the modulation of telomerase microscopic processivity

To better understand the effects of GQ folding on the function of the telomerase, we developed a detailed kinetic framework with which to model our experimental data (Fig. 6). We elected to perform our kinetic modeling on data generated in the absence of POT1-TPP1. This condition sensitizes our DNA primer extension experiments to the influence of GQ folding on the observed product distribution, which is masked in presence of POT1-TPP1 (Fig. 3). Telomerase processivity can be modeled as a series of consecutive reactions in which nucleotide addition is in competition with DNA dissociation at each step of the reaction (Fig. 6A). To simplify our telomerase kinetics analysis, we focus on the intense repeat addition bands, assuming the intervening nucleotide addition steps are relatively rapid and accompanied by little DNA dissociation (Fig. 6B) (see Supplementary text for justification). While the macroscopic processivity of telomerase can be conveniently described by the median product length (49), the experiments described in the present study provide clear evidence that telomerase products do not accumulate uniformly and display patterns dependent upon assay conditions, DNA sequence, and/or product length. We therefore developed a kinetic model that can be utilized to globally fit telomerase time-series data in order to extract individual rate constants for the forward progression and

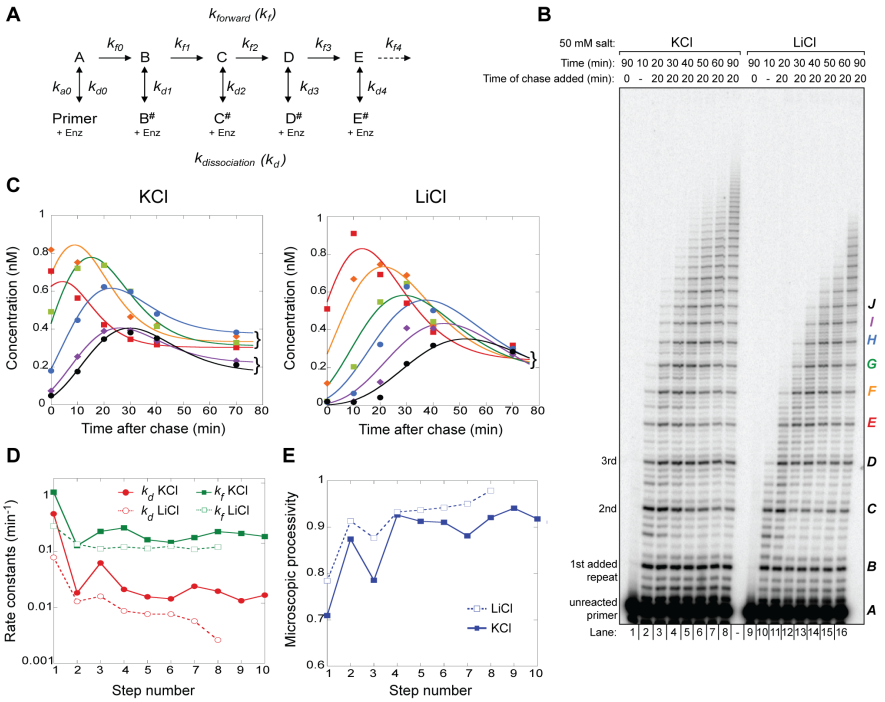

Figure 6. Human telomerase kinetics. (A) Kinetic mechanism for processive telomerase activity used to globally fit the primer extension assay shown in panel B. The letters refer to the repeat band number (Panel B in italics, *B* = 1st added repeat, *C* = 2nd repeat etc.) and dissociated products are identified with the # symbol. Band intensities are proportional to the sum of products (e.g. B + B$^{\#}$). (B) Extending primer dissociation rate assay in the presence of 50 mM KCl or LiCl. Primer extension assays were performed with 50 nM ^{32}P-end-labeled $(TTAGGG)_3$ primer. 20 μM unlabeled chase $(TTAGGG)_3$ primer was added to the reaction after 20 minutes of activity. A control reaction with 20 μM unlabeled chase primer added at the beginning of telomerase activity was included for both buffer conditions (lanes 1 and 9). Repeat number added to the primer is indicated on the left of the gel. Letters indicating band identity for kinetic modeling is indicated on the right of the gel. Bands *E-J* are colored according to plot shown in C. (C) Representative global fits to bands *E-J* in KCl (left panel) and LiCl (right panel). The concentration of the products (see color code in B), based on band intensity relative to the initial 50 nM primer, was plotted against the time after the unlabeled chase. Note the clustering of bands *E-H* and *I-J* 70 minutes post chase in the presence of KCl, which corresponds to the four repeats of the first plateau and the first two repeats of the second plateau (cf. Fig. 2). This partitioning is not present in the presence of LiCl. See Figures S5A and B for corresponding plots for bands *B* to *D* that precede the 'pattern of four' bands. (D) Consecutive rate constant values for forward repeat addition (green squares, k_f) and dissociation (red circles, k_d) returned by DynaFit for data in the presence of KCl (solid symbols) and LiCl (open symbols). The step number refers to the rate constant subscripts shown in A. Note the overall reaction is slower in the presence of LiCl and beyond band *I* (8th step) the fitted rate constant values had a large error because the decay phase had barely started by 70 min. Therefore, these values were omitted. (E) Microscopic processivity (k_f / (k_f + k_d)) at each step of the reaction calculated from the rate constants shown in D. Note the saw-tooth structure in the presence of KCl (solid line) compared to the relative lack of structure in LiCl beyond the second step (dashed line). See also Fig. S6C.

product dissociation at each RAP step that underlie the observed distributions of telomerase products (Fig. 6A). Using this scheme, we treat this multistep process as a first-order reaction with an effective forward rate constant (k_f) for the transition between each repeat and a dissociation rate constant (k_d) (Fig. 6A) (note that k_f in this model reflects a combination of k_{pol} and k_{trans} described in Fig. 1A). Using the kinetic scheme depicted in Figure 6A, we can then define the microscopic processivity (p) at each step as $p = k_f / (k_f + k_d)$.

DNA dissociation is an effectively irreversible process when a large excess of unreacted primer remains, which outcompetes the re-binding of any product DNA. To ensure our experiments complied with this assumption, we analyzed telomerase kinetics following a chase with 400-fold excess of unlabeled primer DNA, which serves to block re-association of the labeled DNA primer following telomerase dissociation (Fig. 6B). Telomerase time course assays were performed in the presence of either K^+ or Li^+ activity buffer conditions (Fig. 6B). Activity was initiated at time zero in the presence of end-labeled telomere DNA primer and dNTPs, followed by addition of excess chase primer at 20 minutes. The presence of 400-fold excess cold primer prior to enzyme addition was sufficient to eliminate any observable extension of the 50 nM end-labeled DNA primer used in our assays (Fig. 6B, lanes 1 and 9). Time points were collected at regular intervals out to 90 minutes and the concentration of each repeat species ($B + B^{\#}$, $C + C^{\#}$, etc., Fig. 6A) was determined at each time point from the band intensity, knowing that the intensity of the initial primer was 50 nM. Individual rate constants were estimated by fitting the concentration time courses globally, using DynaFit (59) (Fig. 6C and S5A and B). Global fitting converged to a set of rate

constants that could be extracted with reasonable precision (see Supplementary Methods for details of kinetic modeling) (Fig. 6D). Comparison of the data obtained in the presence of K^+ and Li^+ revealed that the rate constants, k_f and k_d, decrease with increasing repeat number and result in slightly lower microscopic processivity values for short DNA products as has been noted previously (49). However, in the presence of K^+, the rate constants and microscopic processivity values show a saw-tooth modulation that gives rise to the 'pattern of four' clustering of products noted earlier (Fig. 6E, closed symbols). Although the effect is relatively small, it is robust as determined by Monte-Carlo analysis and is reproducible between experiments and telomerase preparations (Fig. S5 and S6). Interestingly, the rate constants for repeat addition (k_f) and dissociation (k_d) were greater in the presence of K^+ than in Li^+, but the resultant microscopic processivity was lower (Fig. 6D and 6E). Microscopic processivity values were checked using the method of Peng et al. (60) and showed that those derived from kinetic analysis were self-consistent (Fig. S6C).

Taken together, these results suggest that in the presence of K^+, the ability of the DNA product to form a GQ fold (which first arises at step 3) promotes translocation (increased k_f) but at the increased risk of DNA product dissociation (increased k_d) (see Discussion for details). By implication, the absence of GQ folds in Li^+ appears to slow product accumulation (decreased k_f) (Fig. 4, 5 and S4), while decreasing dissociation rate constants (k_d), the functional equivalent of which can be considered a more stable binding of the product DNA through the anchor site(s). The kinetic analysis and corresponding primer extension assays hence raise questions as to the relationship between product DNA structure and anchor site stability.

GQ stabilization alters DNA product handling and structural dynamics

The results of our ensemble telomerase assays suggest that folding of the nascent DNA product can influence telomerase catalysis. To interrogate DNA conformation within an active RNP complex, we employed a single molecule Förster Resonance Energy Transfer (smFRET) assay that directly monitors DNA structure and dynamics within individual telomerase enzymes (48, 61). To simplify interpretation of our single molecule experiments in the present study, we focus again on the telomerase catalytic core in the absence of POT1-TPP1. In order to ensure our smFRET assay supports telomerase activity in both K^+ and Li^+ buffers we utilized a previously reported method for *in situ*

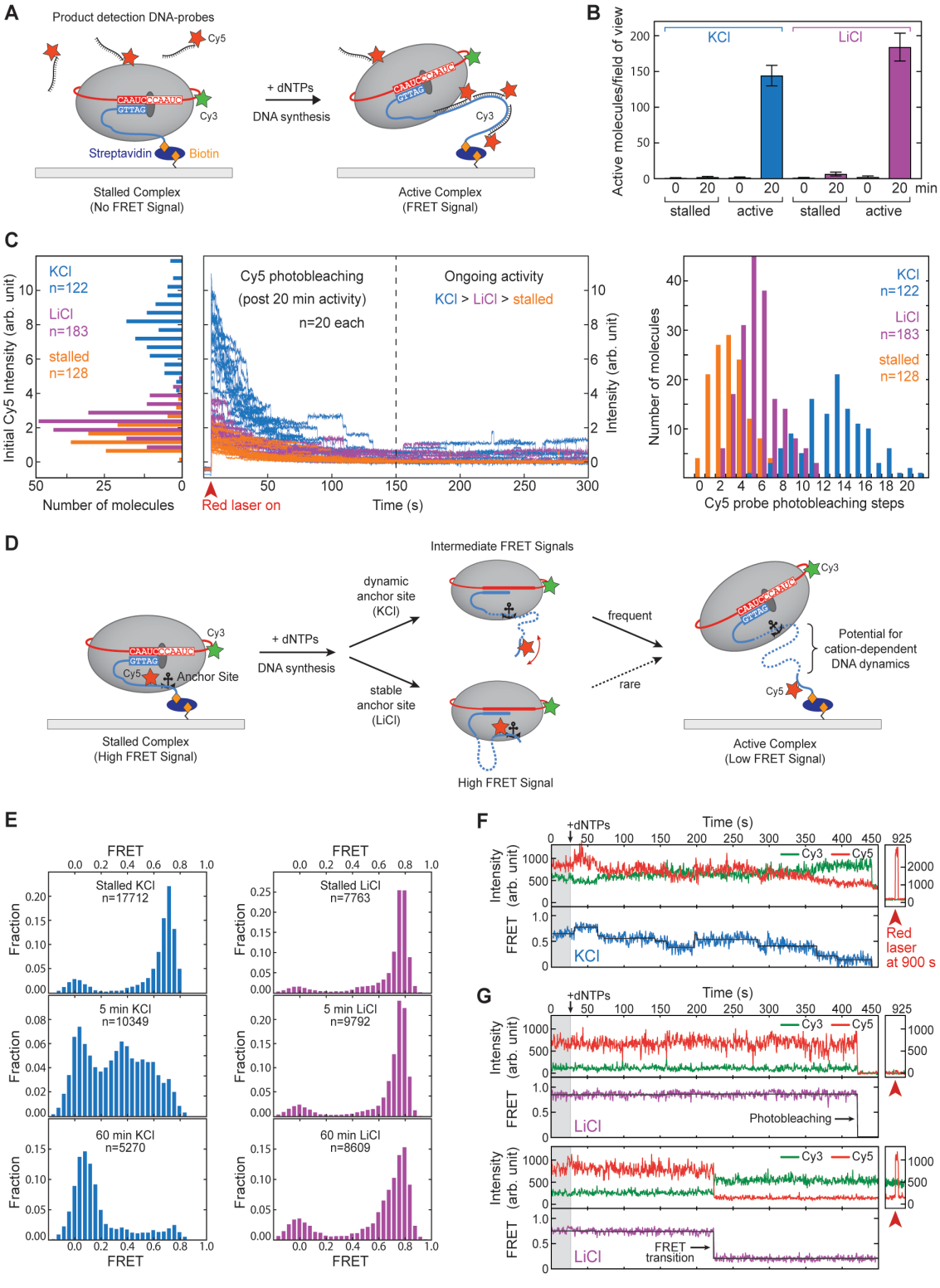
A
Product detection DNA-probes
Cy5
Cy3
Streptavidin
Biotin
+ dNTPs
DNA synthesis
Stalled Complex
(No FRET Signal)
Active Complex
(FRET Signal)
B
Active molecules/field of view
KCl
LiCl
stalled
active
min
C
Initial Cy5 Intensity (arb. unit)
KCl
n=122
LiCl
n=183
stalled
n=128
Number of molecules
Cy5 photobleaching
(post 20 min activity)
n=20 each
Ongoing activity
KCl > LiCl > stalled
Red laser on
Time (s)
Intensity (arb. unit)
Number of molecules
Cy5 probe photobleaching steps
D
Intermediate FRET Signals
dynamic
anchor site
(KCl)
stable
anchor site
(LiCl)
Anchor Site
Stalled Complex
(High FRET Signal)
frequent
rare
Potential for
cation-dependent
DNA dynamics
Active Complex
(Low FRET Signal)
High FRET Signal
E
FRET
Fraction
Stalled KCl
n=17712
5 min KCl
n=10349
60 min KCl
n=5270
Stalled LiCl
n=7763
5 min LiCl
n=9792
60 min LiCl
n=8609
F
+dNTPs
Time (s)
Intensity (arb. unit)
Cy3
Cy5
FRET
KCl
Red
laser
at 900 s
G
LiCl
Photobleaching
FRET
transition

Figure 7. Single-molecule studies of telomerase in the presence of KCl and LiCl. (A) Schematic of human telomerase smFRET activity assay. Purified telomerase is immobilized to a pegylated and biotinylated quartz slide through binding to a biotinylated telomere primer (blue). TERT is depicted as a grey oval and hTR is shown in red. A Cy3 dye (green star) is conjugated to hTR. The binding of Cy5-labeled detection oligonucleotide probes (in black with red star) to newly synthesized telomere DNA is illustrated at right. (B) Analysis of smFRET activity assays in KCl (blue) and LiCl (magenta) cation conditions. Negative controls were performed in presence of Cy5-detection probes but in absence of dNTPs (stalled). Time points and number of FRET-positive molecules per field of view imaged are indicated. Error bars are the standard deviation across all fields imaged (n > 10). (C) Left, histogram analysis of the 'initial Cy5 intensity' distribution under direct laser excitation of active telomerase-DNA complexes (see A, right) in KCl (blue) and LiCl (magenta) cation conditions. Background signal was assessed in absence of dNTPs (stalled, orange). Center, real-time traces showing time-dependent photobleaching of Cy5 dyes under direct laser excitation. Twenty representative traces are shown for simplification. Color coding as indicated. Right, histogram analysis of the distribution of Cy5 photobleaching steps counted from each individual real-time trace. Conditions and number of traces as indicated. (D) Schematic of human telomerase smFRET experiment designed to probe DNA structural dynamics. The telomere primer (blue) is conjugated to a Cy5 dye (red star). Telomere repeat synthesis impacts the FRET behavior depending upon anchor site stability and identity of monovalent cations as illustrated. (E) Histogram analysis of smFRET assays (see D) in KCl (blue) and LiCl (magenta). FRET distributions are shown for stalled telomerase complexes (top panels) as well as at 5 and 60 minute time points after addition of dNTPs (middle and bottom panels, respectively). (F-G) Representative real-time smFRET traces of individual telomerase complexes (see D) in either KCl (F) or LiCl (G). Cy3 donor intensities are shown in green and Cy5 acceptor intensities in red. The corresponding FRET value (blue or magenta) was fit with steps (black) using automated stepfinding algorithm in MATLAB (74). Direct laser excitation of the Cy5 dye in each trace is shown separately at a 900 sec time point.

activity in both K^+ and Li^+ buffers we utilized a previously reported method for *in situ* detection of extended DNA products at the single-molecule level (62). Telomerase RNP complexes harboring a Cy3-modified telomerase RNA subunit were reconstituted in RRLs,

bound to a biotinylated DNA primer, and surface-immobilized onto a streptavidin-coated quartz slide (Fig. 7A). Importantly, telomerase modified with Cy3 at hTR-U42 has been shown previously to retain wild type catalytic function (48). The telomerase-DNA complexes were incubated in either K^+ or Li^+ activity buffer as well as with Cy5-

labeled detection oligonucleotides, each with a sequence that is complementary to 2.5 repeats of the telomere product (Table S1). In this way, telomere primers that are being actively extended by telomerase emerge from the enzyme and are detected as a FRET signal between the Cy3-labeled enzyme and the Cy5-labeled DNA probe (Fig. 7A). The appearance of the FRET signal was strictly dependent upon addition of activity buffer containing dNTPs and was time dependent (Fig. 7B). After 20 minutes of incubation, comparable fractions of active telomerase molecules that produce a positive FRET signal were detected in both K^+ and Li^+ activity buffers (Fig. 7B), demonstrating that telomerase is catalytically active in either cation condition.

Next, we quantitatively monitored the total amount of product synthesized for individual telomerase-DNA complexes by incubating surface-immobilized telomerase enzymes in K^+ and Li^+ activity buffers for 20 minutes prior to the addition of Cy5 detection probe (Fig. 7A and C). Using direct Cy5 laser excitation permitted a measure of the total fluorescence intensity value, which correlates with the number of Cy5 probes bound to the DNA product ('Initial Intensity', Fig. 7C, left). Moreover, prolonged exposure to direct laser excitation induced photobleaching of every DNA-bound Cy5 probe in a time-dependent manner (Fig. 7C, center). We quantified the number of photobleaching steps for each single molecule trace to yield a relative measure of DNA product length in either K^+ or Li^+ activity buffer (Fig. 7C, right). As expected from our ensemble assays, histogram representations of the 'initial Cy5 intensity' upon direct excitation, as well as the distribution of photobleaching steps reflected a decreased DNA synthesis rate in Li^+ when compared to K^+ conditions (Fig. 7C). Interestingly, we occasionally observed upward steps in Cy5 intensity in either cation condition ($K^+ > Li^+$), consistent with real-

time detection of Cy5 DNA probe binding to newly synthesized DNA repeats (Fig. 7C, center). An equivalent but 'stalled' (no dNTPs) telomerase complex served as background control. Note that non-zero amounts of 'Initial Intensity' and Cy5 photobleaching steps were measured in this condition (Fig. 7C, orange), however, this was not due to Cy5 probe binding to the DNA primer as confirmed earlier by the lack of a respective FRET signal (Fig. 7A and B).

To directly monitor DNA structural dynamics we next performed a variation of our smFRET assay in the absence of detection probe, that instead pairs Cy3-labeled telomerase together with site-specifically Cy5-labeled telomere primer. This assay further interrogates anchor-site stability that may underlie the altered microprocessivity values extracted from our kinetic modeling (Fig. 7D). Data collected on surface-immobilized stalled telomerase-DNA complexes in the absence of dNTPs yielded a predominant FRET distribution centered at ~0.75, together with a minor zero-FRET population that represents telomerase-DNA complexes lacking a functional acceptor dye (Fig. 7E, top panels). Next, the telomerase complexes were activated for DNA synthesis by introducing dNTPs in telomerase activity buffer, resulting in an increase in populations of lower FRET values over time (Fig. 7E, middle and bottom panels). These FRET changes upon activation of DNA synthesis are consistent with the Cy5-label on the telomere DNA moving further away from telomerase (Fig. 7E). On the timescale of minutes to hours, both K^+ and Li^+ buffers support multiple rounds of DNA repeat synthesis sufficient to accumulate a FRET~0 state, in which the dyes are separated beyond their FRET range (Fig. 7F, bottom panels). We note that every data point in the accumulating FRET~0 state is derived from primer-bound telomerase (i.e.

requires the presence of a Cy3 dye) and is not due to telomerase dissociation. Interestingly, despite robust telomerase activity in Li^+ buffer (Fig. 7B and C), we observed an unanticipated stable high FRET population over the course of a one-hour experiment in this cation condition (Fig. 7E). Furthermore, in contrast to K^+ cation conditions, the accumulation of the FRET~0 population occurred in apparent absence of any detectable intermediate FRET states at the time resolution of our measurements (Fig. 7E).

Consistent with these findings, analysis of real-time single-molecule FRET trajectories collected on actively extending telomerase complexes revealed substantially different FRET behaviors in each cation condition. In K^+ buffer, dynamic transitions between discrete FRET states were observed (Fig. 7F and S7). The FRET dynamics generally progressed to lower values, but included transient excursions to higher FRET states, indicative of complex DNA conformational dynamics. In contrast, in Li^+ buffer, we did not observe a substantial drop in FRET in the majority of traces before photobleaching of the Cy5 dye occurred, which can be unambiguously confirmed using direct Cy5 laser excitation at the end of data acquisition (Fig. 7G, upper panel and S7). According to the FRET population analysis in a one-hour time window (Fig. 7E), the *bone fide* FRET transition to a ~0 value in Li^+ buffer (i.e. not due to Cy5 photobleaching) should be a rare event on the time scale of the experiment. Nevertheless, we did observe occasional FRET traces that captured abrupt transitions from the high to low FRET states, despite the presence of an active Cy5 dye (Fig. 7G, lower panel). The prolonged high FRET state observed in Li+ buffer conditions suggest the presence of a stable anchor site contact during DNA synthesis, that, once disrupted, results in a

rapid and large displacement of product DNA away from the telomerase enzyme (Fig. 7D, bottom pathway). In contrast, GQ-stabilizing conditions give rise to complex FRET dynamics, implying that nascent DNA folding may facilitate efficient extrusion of the telomere DNA away from the telomerase enzyme.

DISCUSSION

The foundation of telomere structure consists of short G-rich repeat sequences, GGTTAG in humans, that have the propensity to fold into G-quadruplex (GQ) structures *in vitro* and *in vivo* (6, 7). Previous studies have suggested that multiple copies of the telomerase processivity factor and shelterin component POT1-TPP1 decorate single-stranded telomeric DNA and thereby hinder the formation of GQ structures (41). POT1-TPP1 further facilitates the recruitment of telomerase to the telomere through interactions between the TPP1 TEL patch and the TERT TEN domain (56, 63). However, the interplay between newly synthesized G-rich repeats and the actively extending telomerase-POT1-TPP1 complex remains poorly understood.

Here, we present evidence that GQ formation can occur within an actively extending telomerase complex *in vitro* and that formation of such GQs affects the kinetic properties of telomerase. Interestingly, the addition of POT1-TPP1 stimulates telomerase processivity, but does not rescue decreased telomere synthesis rates caused by GQ-destabilizing conditions. This finding suggests that GQ folding may also occur in the context of the POT1-TPP1-telomerase complex and modulates

telomerase activity. We describe a detailed kinetic framework for telomerase catalysis and use this model to globally fit telomerase time-series data. Our kinetic modeling reveals small but significant GQ-dependent changes in the rate constants describing the telomere synthesis reaction and permit us to calculate microscopic processivity values for each cycle of telomere DNA repeat synthesis (see Supplemental Methods for details). Moreover, single-molecule FRET experiments reveal that GQ folding impacts the dynamic handling of newly synthesized DNA by the telomerase complex. Collectively, our study reveals the delicate interplay between telomere DNA structure and the actively extending human telomerase complex.

We present a working model for the mechanism of GQ-dependent effects on telomerase repeat addition processivity, as well as the interplay between GQ structures and the POT1-TPP1 processivity factor (Fig. 8). The complex rearrangements necessary for template recycling during multiple rounds of telomere repeat synthesis require multiple anchor sites between telomerase and its DNA substrate to prevent product dissociation (Fig. 1A). In the schematic model depicted in Figure 8A, two principal pathways are shown that depend on the register of the 3′ end of the telomere as well as on the state of anchor site interactions during the formation of a GQ. GQ folding may bias the positioning of the 3′ end of the primer to favor realignment for a subsequent round of repeat synthesis, provided anchor site contacts remain intact (Fig. 8A, top pathway). This outcome is mechanistically similar to DNA hairpin induced translocation models proposed for diverse telomerase systems (64, 65). Alternately, GQ folding within the DNA product may compete with anchor-site contacts to promote dissociation (Fig. 8A, bottom pathway), as was suggested in

previous telomerase studies that investigated the effect of putative GQ folding during active telomere elongation (38-40).

Any contact with the growing product DNA must be dynamic in the course of activity and might involve further elements of telomerase or associated factors, such as POT1-TPP1 that binds to telomeric DNA and enhances RAP (34, 41). Our data indicate that GQ formation within actively extending telomerase might be required for correct POT1-TPP1 function, in particular the stimulation of telomeric DNA synthesis rates during processive enzyme action. We propose a speculative model, wherein GQ formation within the telomerase complex, followed by POT1-TPP1 binding and GQ unfolding, serves as a mechanism to ensure the concerted decoration and protection of nascent single-stranded telomeric DNA (Fig. 8B). This model is consistent with previous studies reporting a preference of POT1-TPP1 binding to telomeric DNA in a 3′ to 5′ direction (34, 66). This directionality was reported also for the unfolding of GQs by POT1, whereby its individual OB-fold domains engage the GQ in a stepwise manner

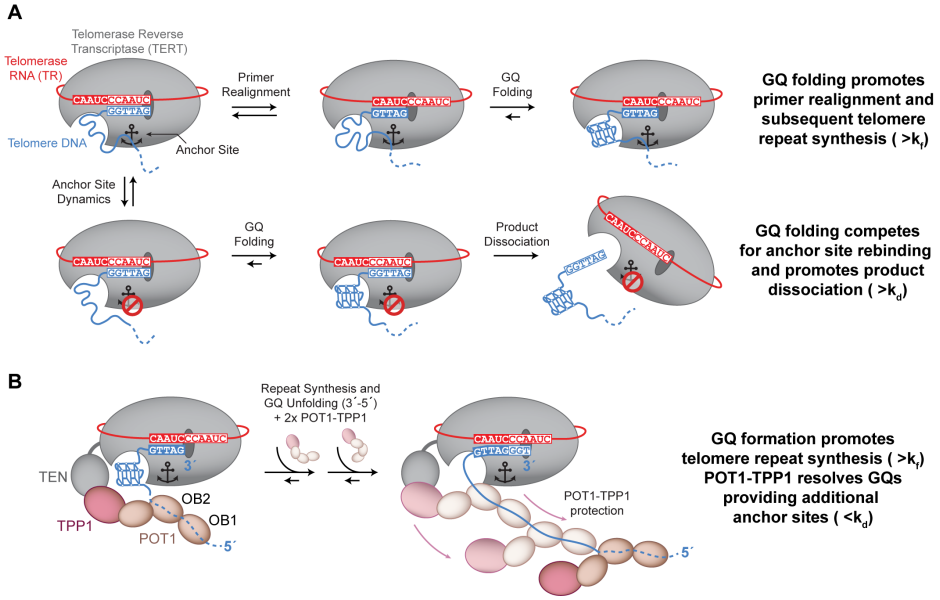

Figure 8. Model of GQ folding within actively extending telomerase complex. (A) At the completion of a telomere repeat, telomerase (with TERT depicted in grey and hTR in red), is annealed to the telomere DNA (blue). The schematically drawn anchor site (dashed circle) is either engaged with the telomere DNA (upper pathway) or disengaged (lower pathway). Sequential repeat synthesis and primer realignment extrude telomere DNA from the active site to eventually allow for GQ formation. In the case where anchor site contacts are maintained at this stage (upper, middle and right cartoons), the formation of a GQ may bias the enzyme complex towards another round of telomere repeat addition. If the anchor site contacts are instead broken when GQ formation occurs (lower, left and middle cartoons), primer realignment results in product dissociation at this stage (bottom, right cartoon). (B) Extension of the mechanistic GQ model (see A) illustrating the possibility and functional contribution of GQ formation in the presence of the GQ resolvase POT1-TPP1. A telomere bound POT1-TPP1 unit engages the hTERT TEN domain via TPP1. Upon GQ formation, further POT1-TPP1 units are recruited to resolve the GQ in a 3′ to 5′ direction resulting in fully protected telomere DNA. Concurrent telomere synthesis generates additional G-rich repeats for the process to continue in a four-repeat periodicity.

(Fig. 8B, OB2 before OB1) (42, 43). Interestingly, the binding of multiple POT1-TPP1 units to telomeric DNA might occur in a pairwise and cooperative fashion, whereby each pair of POT1-TPP1 dimers spans four consecutive G-rich repeats of the unfolded telomeric DNA (34, 66) (Fig. 8B). These lines of evidence are inconsistent with the binding of POT1-TPP1 to each telomeric repeat as it emerges from the telomerase

enzyme (i.e. 5′ to 3′ directionality), but rather describe a 'lagging' type of protein decoration, in which multiple telomeric repeats are produced prior to POT1-TPP1 binding in a reverse direction (Fig. 8B).

The recently reported cryo-EM structures of the human and *Tetrahymena* telomerase enzymes provide a platform for investigating the potential for GQ folding within the actively extending telomerase complex (33, 67). Interestingly, when analyzing the EM density of the human telomerase complex, we noticed a structural pocket immediately proximal to the path of the nascent DNA emerging from the active site (Fig. S8A). This pocket is flanked by two evolutionarily conserved and potentially dynamic elements that are essential for telomerase processivity: the telomerase essential N-terminal (TEN) domain and the hTR P6.1 stem loop (45, 68). The volume of this pocket is compatible with the dimensions of a GQ fold, and raises the possibility that the nascent DNA product has ample space to assume a GQ structure within the confines of telomerase RNP complex prior to POT1-TPP1 binding to the DNA. In the *Tetrahymena* structure, the C-terminal domain of the processivity factor, Teb1, is positioned as a lid to the DNA exit pocket, forming an enclosed cavity that is also sufficient to accommodate a single GQ fold (Fig. S8B). We propose the hypothesis that the Teb1-related shelterin component POT1 may occupy a similar position in the human telomerase complex. Thus, the anticipated binding of POT1 to the DNA as it is threaded out of this DNA exit channel is not mutually exclusive with the possibility of GQ folding within this protected cavity (33, 55, 67).

Our proposed model, while speculative, provides a functional explanation for the evolutionary conservation of G-rich telomere DNA by providing a possible mechanistic link between GQ folding in telomere maintenance and/or telomerase function. Future experiments should continue to investigate the influence of the shelterin proteins POT1-TPP1 on the folding properties of the nascent telomere DNA product, as well as to evaluate the *in vivo* significance of telomerase-confined GQ folding and its suitability for GQ-targeted anti-cancer therapies.

MATERIALS AND METHODS

Preparation of RNAs

Telomerase RNA fragments (hTR CR4/5 (hTR 239-328) and hTR template/pseudoknot (hTR t/PK, 32-195) were prepared using standard *in vitro* transcription protocols. For smFRET experiments, preparation of dye-labeled RNA fragments was performed as described previously (69) (see Supplementary Methods for details).

Telomerase expression and purification

Human telomerase was reconstituted with purified RNA fragments in rabbit reticulocyte lysate (RRL) using the Promega TnT Quick Coupled Transcription/Translation system (47). FLAG-TERT was expressed off the pNFLAG-hTERT plasmid (70) (details of RRL reconstitution are described in Supplementary Methods). For telomerase expression in HEK293T cells, lysate was provided by Samantha Sanford and Patricia Opresko (University of Pittsburgh) prepared as

described previously (71). Telomerase enzyme was purified using via the N-terminal FLAG-tag on hTERT, using ANTI-FLAG M2 beads (Sigma-Aldrich), and eluted with 3xFLAG.

^{32}P-end-labeling of DNA primers

50 pmol of the indicated DNA primer was labeled with gamma-^{32}P-ATP using T4 polynucleotide kinase (NEB). For generating experimental data for kinetic modeling, end-labeled primers were PAGE purified and DNA concentration was precisely determined using a Nanodrop spectrophotometer (Thermo Scientific).

Primer extension assays

Telomerase activity assays were performed in 1x TB (50 mM Tris-HCl, pH 8.3, 50 mM KCl (NaCl or LiCl when indicated), 1 mM $MgCl_2$, 2 mM DTT) as described previously. Where indicated, POT1-TPP1 was added to the reaction mix at a final concentration of 500 nM. The 'fraction left behind' (FLB) for a given lane was calculated by summing each RAP band and all RAP bands below it divided by the total RAP band intensity counts for that lane. The natural logarithm of (1-FLB) was then plotted against repeat number and fitted by linear regression (see main text and Supplemental Methods for details and caveats). The slope value of the linear fit was used to determine processivity $R_{1/2}$ values from -ln(2)/slope (49).

POT1-TPP1 expression and purification

Procedures for insect cell expression were according to the Bac-to-Bac Baculovirus Expression System (Thermo Fisher Scientific) using the pFEV-POT1 and pFastBac-

TPP1N (TPP1 residues 89-334) plasmids. POT1-TPP1N was purified via a GST tag on POT1 using Glutathione Sepharose 4B resin (GE Healthcare), eluted with glutathione, and the affinity tag was removed by TEV-protease cleavage.

Kinetic analysis

For kinetic analysis, the primer extension assay described above was modified by chasing with 20 μM cold $(TTAGGG)_3$ DNA primer. The chase primer was added after 20 minutes of initiating the reaction, to prevent radiolabeled DNA primer and radiolabeled DNA product rebinding within the subsequent 70-minute time course. The intensities of the RAP bands on the gel electrophoretogram were converted to absolute concentrations based on the intensity of the initial radiolabeled primer band (i.e. 50 nM). Multiple exposures of the gel to the phosphor screen were analyzed to ensure intense and weak bands remained within the linear range of the phosphorimager. These data were analyzed globally according to the sequential model (Fig. 6A) using DynaFit (59, 73). Further details are given in the Supplementary Methods.

Single-molecule experiments

Unless indicated otherwise, all single molecule experiments were performed as previously described (48). Detailed experimental methods describing microscope slide preparation, telomerase enzyme immobilization, *in situ* telomerase activity assays, and data acquisition/analysis can be found in the Supplementary Methods.

ACKNOWLEDGEMENTS

We thank Dr. Harry Noller, Dr. Alan Zahler, Dr. Patricia Opresko and Samantha Sanford for critical reading of the manuscript. This work was supported by National Institutes of Health Grants F99CA212439 (to L.I.J) and R01GM095850 (to M.D.S). J.H. was supported by a Swiss National Science Foundation (SNSF) Early Postdoc.Mobility Fellowship.

AUTHOR CONTRIBUTIONS

L.I.J., J.H. and M.D.S. designed research, L.I.J., J.H., T.C., C.L., and R.B. performed research, L.I.J., J.H., J.W.P., C.R.B. and M.D.S. analyzed data and L.I.J., J.H., C.R.B. and M.D.S. wrote the paper.

REFERENCES

1. de Lange T (2005) Shelterin: the protein complex that shapes and safeguards human telomeres. *Genes Dev* 19(18):2100-2110.
2. de Lange T (2010) How shelterin solves the telomere end-protection problem. *Cold Spring Harb Symp Quant Biol* 75:167-177.
3. Palm W & de Lange T (2008) How shelterin protects mammalian telomeres. *Annu Rev Genet* 42:301-334.
4. McElligott R & Wellinger RJ (1997) The terminal DNA structure of mammalian chromosomes. *EMBO J* 16(12):3705-3714.
5. Maizels N & Gray LT (2013) The G4 genome. *PLoS Genet* 9(4):e1003468.
6. Li J, Correia JJ, Wang L, Trent JO, & Chaires JB (2005) Not so crystal clear: the structure of the human telomere G-quadruplex in solution differs from that present in a crystal. *Nucleic Acids Res* 33(14):4649-4659.
7. Burge S, Parkinson GN, Hazel P, Todd AK, & Neidle S (2006) Quadruplex DNA: sequence, topology and structure. *Nucleic Acids Res* 34(19):5402-5415.
8. Saharia A*, et al.* (2008) Flap endonuclease 1 contributes to telomere stability. *Curr Biol* 18(7):496-500.
9. Leon-Ortiz AM, Svendsen J, & Boulton SJ (2014) Metabolism of DNA secondary structures at the eukaryotic replication fork. *DNA Repair (Amst)* 19:152-162.
10. London TB*, et al.* (2008) FANCJ is a structure-specific DNA helicase associated with the maintenance of genomic G/C tracts. *J Biol Chem* 283(52):36132-36139.

11. Balasubramanian S, Hurley LH, & Neidle S (2011) Targeting G-quadruplexes in gene promoters: a novel anticancer strategy? *Nat Rev Drug Discov* 10(4):261-275.

12. Schaffitzel C*, et al.* (2001) In vitro generated antibodies specific for telomeric guanine-quadruplex DNA react with Stylonychia lemnae macronuclei. *Proc Natl Acad Sci U S A* 98(15):8572-8577.

13. Lam EYN, Beraldi D, Tannahill D, & Balasubramanian S (2013) G-quadruplex structures are stable and detectable in human genomic DNA. *Nature Communications* 4.

14. Rodriguez R*, et al.* (2012) Small-molecule-induced DNA damage identifies alternative DNA structures in human genes. *Nat Chem Biol* 8(3):301-310.

15. Blackburn EH*, et al.* (1989) Recognition and elongation of telomeres by telomerase. *Genome* 31(2):553-560.

16. Greider CW & Blackburn EH (1987) The telomere terminal transferase of Tetrahymena is a ribonucleoprotein enzyme with two kinds of primer specificity. *Cell* 51(6):887-898.

17. Allsopp RC*, et al.* (1992) Telomere length predicts replicative capacity of human fibroblasts. *Proc Natl Acad Sci U S A* 89(21):10114-10118.

18. Alder JK*, et al.* (2011) Ancestral mutation in telomerase causes defects in repeat addition processivity and manifests as familial pulmonary fibrosis. *PLoS Genet* 7(3):e1001352.

19. Parry EM, Alder JK, Qi X, Chen JJ, & Armanios M (2011) Syndrome complex of bone marrow failure and pulmonary fibrosis predicts germline defects in telomerase. *Blood* 117(21):5607-5611.

20. Gramatges MM, Qi X, Sasa GS, Chen JJ, & Bertuch AA (2013) A homozygous telomerase T-motif variant resulting in markedly reduced repeat addition processivity in siblings with Hoyeraal Hreidarsson syndrome. *Blood* 121(18):3586-3593.

21. Zaug AJ, Crary SM, Jesse Fioravanti M, Campbell K, & Cech TR (2013) Many disease-associated variants of hTERT retain high telomerase enzymatic activity. *Nucleic Acids Res* 41(19):8969-8978.

22. Kim NW*, et al.* (1994) Specific association of human telomerase activity with immortal cells and cancer. *Science* 266(5193):2011-2015.

23. Feng J*, et al.* (1995) The RNA component of human telomerase. *Science* 269(5228):1236-1241.

24. Nakamura TM*, et al.* (1997) Telomerase catalytic subunit homologs from fission yeast and human. *Science* 277(5328):955-959.

25. Greider CW (1991) Telomerase is processive. *Mol Cell Biol* 11(9):4572-4580.

26. Zaug AJ, Podell ER, & Cech TR (2008) Mutation in TERT separates processivity from anchor-site function. *Nat Struct Mol Biol* 15(8):870-872.

27. Jacobs SA, Podell ER, & Cech TR (2006) Crystal structure of the essential N-terminal domain of telomerase reverse transcriptase. *Nat Struct Mol Biol* 13(3):218-225.

28. Lai CK, Mitchell JR, & Collins K (2001) RNA binding domain of telomerase reverse transcriptase. *Mol Cell Biol* 21(4):990-1000.

29. Robart AR & Collins K (2011) Human telomerase domain interactions capture DNA for TEN domain-dependent processive elongation. *Mol Cell* 42(3):308-318.

30. Lue NF (2005) A physical and functional constituent of telomerase anchor site. *J Biol Chem* 280(28):26586-26591.

31. Lue NF & Li Z (2007) Modeling and structure function analysis of the putative anchor site of yeast telomerase. *Nucleic Acids Res* 35(15):5213-5222.

32. Wu RA, Tam J, & Collins K (2017) DNA-binding determinants and cellular thresholds for human telomerase repeat addition processivity. *EMBO J* 36(13):1908-1927.

33. Jiang J*, et al.* (2018) Structure of Telomerase with Telomeric DNA. *Cell* 173(5):1179-1190 e1113.

34. Wang F*, et al.* (2007) The POT1-TPP1 telomere complex is a telomerase processivity factor. *Nature* 445(7127):506-510.

35. Schmidt JC, Zaug AJ, Kufer R, & Cech TR (2018) Dynamics of human telomerase recruitment depend on template- telomere base pairing. *Molecular biology of the cell*.

36. Hwang H*, et al.* (2014) Telomeric overhang length determines structural dynamics and accessibility to telomerase and ALT-associated proteins. *Structure* 22(6):842-853.

37. Lei M, Zaug AJ, Podell ER, & Cech TR (2005) Switching human telomerase on and off with hPOT1 protein in vitro. *J Biol Chem* 280(21):20449-20456.

38. Zahler AM, Williamson JR, Cech TR, & Prescott DM (1991) Inhibition of telomerase by G-quartet DNA structures. *Nature* 350(6320):718-720.

39. Min B & Collins K (2010) Multiple mechanisms for elongation processivity within the reconstituted tetrahymena telomerase holoenzyme. *J Biol Chem* 285(22):16434-16443.

40. Sun D, Lopez-Guajardo CC, Quada J, Hurley LH, & Von Hoff DD (1999) Regulation of catalytic activity and processivity of human telomerase. *Biochemistry* 38(13):4037-4044.

41. Taylor DJ, Podell ER, Taatjes DJ, & Cech TR (2011) Multiple POT1-TPP1 proteins coat and compact long telomeric single-stranded DNA. *Journal of molecular biology* 410(1):10-17.

42. Hwang H, Buncher N, Opresko PL, & Myong S (2012) POT1-TPP1 regulates telomeric overhang structural dynamics. *Structure* 20(11):1872-1880.

43. Lei M, Podell ER, & Cech TR (2004) Structure of human POT1 bound to telomeric single-stranded DNA provides a model for chromosome end-protection. *Nat Struct Mol Biol* 11(12):1223-1229.

44. Traut TW (1994) Physiological concentrations of purines and pyrimidines. *Mol Cell Biochem* 140(1):1-22.

45. Chen JL & Greider CW (2003) Determinants in mammalian telomerase RNA that mediate enzyme processivity and cross-species incompatibility. *EMBO J* 22(2):304-314.

46. Chen JL & Greider CW (2003) Template boundary definition in mammalian telomerase. *Genes Dev* 17(22):2747-2752.

47. Weinrich SL*, et al.* (1997) Reconstitution of human telomerase with the template RNA component hTR and the catalytic protein subunit hTRT. *Nature genetics* 17(4):498-502.

48. Parks JW & Stone MD (2014) Coordinated DNA dynamics during the human telomerase catalytic cycle. *Nat Commun* 5:4146.

49. Latrick CM & Cech TR (2010) POT1-TPP1 enhances telomerase processivity by slowing primer dissociation and aiding translocation. *EMBO J* 29(5):924-933.

50. Hammond PW & Cech TR (1997) dGTP-dependent processivity and possible template switching of euplotes telomerase. *Nucleic Acids Res* 25(18):3698-3704.

51. Maine IP, Chen SF, & Windle B (1999) Effect of dGTP concentration on human and CHO telomerase. *Biochemistry* 38(46):15325-15332.

52. Hardy CD, Schultz CS, & Collins K (2001) Requirements for the dGTP-dependent repeat addition processivity of recombinant Tetrahymena telomerase. *J Biol Chem* 276(7):4863-4871.

53. Chen YN, Podlevsky JD, Logeswaran D, & Chen JJL (2018) A single nucleotide incorporation step limits human telomerase repeat addition activity. *Embo Journal* 37(6).

54. Moye AL*, et al.* (2015) Telomeric G-quadruplexes are a substrate and site of localization for human telomerase. *Nat Commun* 6:7643.

55. Zaug AJ, Podell ER, & Cech TR (2005) Human POT1 disrupts telomeric G-quadruplexes allowing telomerase extension in vitro. *Proc Natl Acad Sci U S A* 102(31):10864-10869.

56. Nandakumar J*, et al.* (2012) The TEL patch of telomere protein TPP1 mediates telomerase recruitment and processivity. *Nature* 492(7428):285-289.

57. Sen D & Gilbert W (1990) A sodium-potassium switch in the formation of four-stranded G4-DNA. *Nature* 344(6265):410-414.

58. Klenow H & Henningsen I (1969) Effect of monovalent cations on the activity of the DNA polymerase of Escherichia coli B. *Eur J Biochem* 9(1):133-141.

59. Kuzmic P (2009) DynaFit--a software package for enzymology. *Methods Enzymol* 467:247-280.

60. Peng Y, Mian IS, & Lue NF (2001) Analysis of telomerase processivity: mechanistic similarity to HIV-1 reverse transcriptase and role in telomere maintenance. *Mol Cell* 7(6):1201-1211.

61. Wu JY, Stone MD, & Zhuang X (2010) A single-molecule assay for telomerase structure-function analysis. *Nucleic Acids Res* 38(3):e16.

62. Hwang H, Opresko P, & Myong S (2014) Single-molecule real-time detection of telomerase extension activity. *Sci Rep* 4:6391.

63. Xin H*, et al.* (2007) TPP1 is a homologue of ciliate TEBP-beta and interacts with POT1 to recruit telomerase. *Nature* 445(7127):559-562.

64. Yang W & Lee YS (2015) A DNA-hairpin model for repeat-addition processivity in telomere synthesis. *Nat Struct Mol Biol* 22(11):844-847.

65. Jarstfer MB & Cech TR (2002) Effects of nucleotide analogues on Euplotes aediculatus telomerase processivity: evidence for product-assisted translocation. *Biochemistry* 41(1):151-161.

66. Corriveau M, Mullins MR, Baus D, Harris ME, & Taylor DJ (2013) Coordinated interactions of multiple POT1-TPP1 proteins with telomere DNA. *J Biol Chem* 288(23):16361-16370.

67. Nguyen THD*, et al.* (2018) Cryo-EM structure of substrate-bound human telomerase holoenzyme. *Nature* 557(7704):190-195.

68. O'Connor CM, Lai CK, & Collins K (2005) Two purified domains of telomerase reverse transcriptase reconstitute sequence-specific interactions with RNA. *J Biol Chem* 280(17):17533-17539.

69. Akiyama BM & Stone MD (2009) Assembly of complex RNAs by splinted ligation. *Methods Enzymol* 469:27-46.

70. Drosopoulos WC, Direnzo R, & Prasad VR (2005) Human telomerase RNA template sequence is a determinant of telomere repeat extension rate. *J Biol Chem* 280(38):32801-32810.

71. Fouquerel E*, et al.* (2016) Oxidative guanine base damage regulates human telomerase activity. *Nat Struct Mol Biol* 23(12):1092-1100.

72. Laederach A*, et al.* (2008) Semiautomated and rapid quantification of nucleic acid footprinting and structure mapping experiments. *Nat Protoc* 3(9):1395-1401.

73. Kuzmic P (1996) Program DYNAFIT for the analysis of enzyme kinetic data: application to HIV proteinase. *Anal Biochem* 237(2):260-273.

74. Kerssemakers JW*, et al.* (2006) Assembly dynamics of microtubules at molecular resolution. *Nature* 442(7103):709-712.

SUPPLEMENTARY METHODS

Preparation of RNAs

Synthetic, dye-labeled RNA fragments

Synthetic hTR fragment 32-62 was ordered from Dharmacon with an internal aminoallyl uridine (5-N-U) on position U42 for labeling as described. RNA was resuspended in nuclease-free water and ethanol precipitated in the presence of 300 mM sodium acetate, pH 5.2. The pellet was resuspended in 100 µl 0.1 M sodium bicarbonate and was used to solubilize a single mono-reactive Cy3-dye pack (Amersham). The solution was incubated in the dark for 2 h at 37°C. The solution was then adjusted to 300 mM sodium acetate, pH 5.2, and the RNA was ethanol precipitated. The pellet was resuspended in deprotection buffer (100 mM acetic acid, pH 3.6), vortexed and centrifuged for 10 seconds each. The solution was then heated at 60°C for 30 min followed by ethanol precipitation. The pellet was resuspended in 60 µl 0.1 M triethylamine acetate, pH 7.5, and dye-labeled RNA was HPLC purified on a reversed phase C8 column (Agilent Technologies).

Ligation of RNA fragments

In order to generate the dye-labeled hTR template/pseudoknot domain (hTR 32-195), a splinted ligation reaction (1) containing 800 pmol of Cy3-labeled hTR 32-62 fragment, 1600 pmol of *in vitro* transcribed unlabeled hTR 63-195, 1600 pmol DNA splint (see Table S1) in 0.5x T4 DNA ligase buffer (NEB) was brought to 200 µl volume and was incubated at 95°C for 5 min and at 30°C for further 10 min. 200 µl ligation mix (1.5x T4 DNA ligase buffer, 8000 units of T4 DNA ligase (NEB), 2 mM ATP and 1 U/µl

RNasin Plus (Promega)) was then added to the reaction mixture and incubated overnight at 30°C. 10 units of TURBO DNase (Thermo Fisher Scientific) were then added and incubated for 15 min at 37°C. The RNA was then phenol-chloroform extracted and ethanol precipitated prior to purification by preparative urea polyacrylamide gel electrophoresis (PAGE).

In vitro transcription

Unlabeled hTR CR4/5 (hTR 239-328) and hTR template/pseudoknot (hTR t/PK, 32-195) fragments were *in vitro* transcribed using homemade T7 RNA polymerase in RNA polymerase reaction buffer (40 mM Tris-HCl, pH 7.9, 28 mM $MgCl_2$, 90 mM DTT, 2 mM spermidine, 1.5 mM each NTP and 40 U RNasin Plus). The reaction was incubated overnight at 37°C followed by the addition of 10 units of TURBO DNase for 15 min at 37°C. The RNA was phenol-chloroform extracted and ethanol precipitated prior to denaturing urea PAGE purification. hTR t/PK 63-195 for splinted ligation reactions was *in vitro* transcribed as described but with 1 mM of each NTP and 5 mM GMP to obtain 5′ monophosphate groups.

Telomerase Expression and Purification

Human telomerase was reconstituted in rabbit reticulocyte lysate (RRL) using the Promega TnT Quick Coupled Transcription/Translation system (47). In Lo-bind tubes (Eppendorf), 200 µl of TnT quick mix was combined with 5 µg of pNFLAG-hTERT (70) plasmid as well as 1 µM of *in vitro* transcribed and unlabeled hTR t/PK and CR4/5 fragments. Less abundant Cy3-labeled hTR t/PK was instead added at 0.1 µM. The reaction was incubated for 3 h at 30°C. 5 µl of 0.5 M EDTA, pH 8.0, were then added

to chelate Mg^{2+} ions present in the lysate. For telomerase expression in HEK293T cells, lysate was provided by Samantha Sanford and Patricia Opresko (University of Pittsburgh) prepared as described previously (71). After expression in RRL or HEK293T cells, telomerase was purified via the N-terminal FLAG tag on hTERT using ANTI-FLAG M2-agarose beads (Sigma-Aldrich). Beads contained in 50 µl bead slurry were first washed three times with wash buffer (50 mM Tris-HCl, pH 8.3, 3 mM $MgCl_2$, 2 mM DTT, 100 mM NaCl) with 30 sec centrifugation steps at 2350 rcf at 4°C after each wash. The beads were then blocked twice in blocking buffer (50 mM Tris-HCl, pH 8.3, 3 mM $MgCl_2$, 2 mM DTT, 500 µg/ml BSA, 50 µg/ml glycogen, 100 µg/ml yeast tRNA) for 15 min under gentle agitation at 4°C followed by 30 sec centrifugation at 2350 rcf and removal of the supernatant. After blocking, the beads were resuspended in 200 µl blocking buffer and added to the telomerase reconstitution reaction in RRL. The beads and lysate were incubated for 2 h at 4°C under gentle agitation. The beads were then pelleted for 30 sec at 5000 rpm and at 4°C and the supernatant was discarded. The beads were then washed three times in wash buffer containing 300 mM NaCl (KCl or LiCl for salt dependence experiments) followed by three wash steps in wash buffer containing 100 mM NaCl (KCl or LiCl for salt dependence experiments). A 30 sec centrifugation at 2350 rcf at 4°C was performed between each wash cycle. To elute the enzyme, the beads were incubated in 60 µl elution buffer (50 mM Tris-HCl, pH 8.3, 3 mM $MgCl_2$, 2 mM DTT, 750 µg/ml 3xFLAG peptide, 20% glycerol) under gentle agitation at 4°C for 1 h. After elution, the beads were removed by centrifugation at 10000 rcf through Nanosep MF 0.45 µm filters. 5 µl aliquots were prepared in Lo-bind tubes, flash frozen in liquid nitrogen and stored at -80°C until use.

^{32}P-end-labeling of DNA primers

50 pmol of DNA primer was labeled with gamma-^{32}P ATP using T4 polynucleotide kinase (NEB) in 1x PNK buffer (70 mM Tris-HCl, pH 7.6, 10 mM $MgCl_2$, 5 mM DTT) in 50 µl reaction volume. The reaction was incubated for 1 h at 37°C followed by heat inactivation of T4 PNK at 65°C for 20 min. Centrispin columns (Princeton Separations) were used to purify labeled primer. For generating experimental data for kinetic modeling, end-labeled primers were PAGE purified and DNA concentration was precisely determined using a Nanodrop spectrophotometer.

Primer extension assays

Telomerase activity assays were performed using 5 µl purified telomerase in a 15 µl reaction volume brought to 1x activity buffer concentrations (50 mM Tris-HCl, pH 8.3, 50 mM KCl (NaCl or LiCl when indicated), 1 mM $MgCl_2$, 2 mM DTT). For experiments containing ^{32}P-end-labeled DNA primer, each reaction contained 10 µM of each dATP, dTTP and dGTP as well as 50 nM of primer. For reactions containing radiolabeled dGTP, each reaction contained the indicated dNTP concentrations as well as 50 nM unlabeled $(TTAGGG)_3$ DNA primer. Where indicated, POT1-TPP1 was added to the reaction mix at a final concentration of 500 nM. Reactions were incubated for 90 min at 30°C and quenched with 200 µl 1x TES buffer (10 mM Tris-HCl, pH 7.5, 1 mM EDTA, 0.1% SDS). DNA products were then phenol-chloroform extracted and ethanol precipitated. DNA pellets were resuspended in 1x formamide gel loading buffer (50 mM Tris Base, 50 mM boric acid, 2 mM EDTA, 80% (v/v) formamide, 0.05% (w/v) each bromophenol blue and xylene cyanol) and resolved on a 12% denaturing urea PAGE gel. The gel was then dried and exposed to a storage phosphor screen (GE

Healthcare) and scanned using a Typhoon scanner (GE Healthcare). Band intensities were quantified using SAFA (72). The 'fraction left behind' (FLB) for a given lane was calculated by summing each RAP band and all RAP bands below it divided by the total RAP band intensity counts for that lane. The natural logarithm of (1-FLB) was then plotted against repeat number and fitted by linear regression (see main text and Supplemental Methods for further details and caveats). The slope value of the linear fit was used to determine processivity $R_{1/2}$ values from -ln(2)/slope (49).

Single-molecule experiments

Slide preparation

Quartz slides (Finkenbeiner Inc.) were cleaned in boiling water and with Alconox detergent powder. The slides were then sonicated for 20 min in glass holders containing 10% (w/v) Alconox, rinsed with water and further sonicated in water for 5 min. Ultrapure water is used throughout. Next, the slides were sonicated in acetone for 15 min, transferred into 1 M KOH and sonicated for 20 min. The slides were then rinsed with water and thoroughly flame dried on the 'sample side' using a propane torch (BernzOmatic). Slides were cooled at room temperature and transferred into a dry glass holder that was previously cleaned by sonication for 5 min in methanol. Silanization of slides was achieved by addition of silanization solution (mixture of 100 ml methanol, 5 ml glacial acetic acid and 1 ml N-(2-aminoethyl)-3-aminopropyltrimethoxysilane (UCT)) and sonication for 1 min followed by further incubation without sonication for 20 min at room temperature. For slide pegylation, 400 mg of mPEG-Succinimidyl Valerate MW 5000 (Laysan Bio, Inc.) were dissolved in 800 µl of filtered (0.2 µm) 0.1 M sodium bicarbonate. In addition, 2 mg of Biotin-PEG-

Succinimidyl Valerate MW 5000 (Laysan Bio, Inc.) were dissolved in 200 µl filtered 0.1 M sodium bicarbonate. The mPEG and Biotin-PEG solutions were combined (PEG solution) and sonicated for 10 sec to ensure complete dissolution. After silanization, the slides were rinsed with water, dried with nitrogen gas and placed in a humidor box. 150 µl of PEG solution were applied to the 'sample side' of each slide and covered with a coverslip. The slides were incubated overnight in the dark. The coverslip and excess PEG solution were then rinsed off with water and the slides were dried using nitrogen gas. Sample channels were assembled on the pegylated slide surface using Parafilm (Bemis) strips as spacers. Plasma-treated coverslips were then placed to cover strips and channels as the upper channel face. For real-time experiments, prior to cleaning, two holes were drilled at opposite ends of the quartz slides demarcating either end of a respective channel. After cleaning, the end of a plastic pipette tip was cut and glued into one hole to act as a reservoir. Intramedic® PE100 polyethylene tubing was glued to the other hole prior to assembly of the channel. Channels were consequently cut from double sided sticky tape, which was sandwiched between the pegylated quartz surface and a coverslip. This way, sample or buffer of interest can be supplied into the pipet tip reservoir and introduced into the channel by applying suction to the tubing on the opposite end of the channel.

Enzyme immobilization

Channels were incubated with 30 µl 10 mg/ml BSA (NEB) for 30 min. All solutions were passed through the channels by capillary force and removal of excess solution from the end of the channel. At each pass, a final solution volume of approximately 20 µl remained in the channel for incubation. After BSA treatment, 60 µl 0.2 mg/ml

streptavidin (MPS) in T50 buffer (10 mM Tris-HCl, pH 8.3, 50 mM NaCl) were passed through each channel and incubated for 5 min. Each channel was then washed with 150 µl T50 buffer (10 mM Tris-HCl, pH 8.3, 50 mM NaCl, or 50 mM LiCl for Li^+ experiments)). For telomerase complex formation, respective biotinylated telomere DNA primers were brought to 5 nM concentration and heated for 5 min at 95°C in 50 mM Tris-HCl, pH 8.3 (room temperature pH), and 50 mM LiCl prior to cooling on ice. Per channel, 2.5 µl of Cy3-labeled telomerase were incubated with 0.5 nM DNA primer in 10 µl single-molecule buffer (50 mM Tris-HCl, pH 8.3, 50 mM KCl, or LiCl for Li^+ experiments, 1 mM $MgCl_2$, 0.8% glucose, 0.1 mg/ml BSA) for 1 h at room temperature in the dark. For imaging purposes 1x imaging buffer was prepared by saturating single-molecule buffer with Trolox (triplet state quencher) followed by filtration (0.2 µm) and pH adjustment to pH 8.3 with NaOH (or LiOH for Li^+ experiments). Imaging buffer further contained 1% (v/v) of freshly prepared 'Gloxy' solution (200 µg/ml catalase and 100 mg/ml glucose oxidase in T50 buffer at 100% stock concentration). The telomerase-primer complex was consequently diluted with 40 µl of 1x imaging buffer, applied to a slide channel and incubated for 10 minutes at room temperature. The slide was then mounted on a prism-type total internal reflection fluorescence (TIRF) microscope to assess the density of immobilized enzyme.

Primer extension by surface-immobilized telomerase

Immobilized complexes contained either Cy5-labeled or unlabeled DNA primers as indicated in Results. To initiate telomerase activity and/or introduce Cy5-labed DNA detection probes (2), 100 µl of the desired solutions were passed through an individual channel. Activity solutions contained 200 µM of each dATP, dTTP and dGTP in 1x

imaging buffer with cation conditions as specified. Detection probes were used at 100 nM in 1x imaging buffer. Negative controls were conducted in equivalent conditions, but omitting dNTPs. For real-time experiments, activity solutions were added to the custom-made flow channels during active data acquisition.

Data acquisition and analysis

Imaging fields containing 300-700 molecules were imaged on home-built prism-type Total Internal Reflection Fluorescence (TIRF) microscope equipped with an Andor Ixon EMCCD camera at 2 frames/second for real-time smFRET experiments and 10 frames/second for all other single-molecule experiments. Experiments made use of custom Labview software to aquire data and control laser shutters. Green laser (532 nm) power was set to 3 mW for real-time experiments and 15 mW for other experiments. Cy5-photobleaching assays were performed with 35 mW red laser (637 nm) power. Twenty two-second movies were collected in different fields of view for each indicated time point for standard smFRET experiments, and 15-minute movies were collected for real-time smFRET experiments. Individual traces were parsed out using custom written IDL software to correct for dye-cross talk and background. Traces were then filtered in MATLAB and molecules that did not contain and acceptor dye were discarded. FRET intensities were calculated using the equation $FRET=I_A/(I_A+I_D)$ where I_A is the acceptor intensity and I_D is the donor intensity. Histograms and trace representations were generated using custom written MATLAB scripts and GraphPad Prism.

POT1-TPP1 expression and purification

Procedures for insect cell expression were according to the Bac-to-Bac Baculovirus Expression System (Thermo Fisher Scientific). 100 ng of each plasmid pFEV-POT1 and pFastBac-TPP1N (TPP1 residues 89-334) were transformed separately into 50 µl *E. coli* DH10Bac competent cells (Thermo Fisher Scientific) to generate bacmids for expression in Sf9 cells (Expression Systems). Transformed cells were plated onto LB agar plates containing 50 µg/ml kanamycin, 7 µg/ml gentamicin, 10 µg/ml tetracycline, 100 µg/ml Bluo-gal and 40 µg/ml IPTG. White colonies from both POT1 and TPP1 plates were inoculated into 5 ml of 2xYT media containing 50 µg/ml kanamycin, 7 µg/ml gentamicin and 10 µg/ml tetracycline for overnight incubation at 37°C at 200 rpm. Bacmids were isolated according to the QIAGEN miniprep protocol. $2x10^6$ Sf9 cells were plated to a total volume of 4 ml Sf9 media (Expression Systems) in a 60 mm culture dish. Cells were left to adhere for 10-15 min. 186 µl of Grace's media and 12 µl Fugene6 transfection reagent (Promega) were mixed and incubated at room temperature for 5 min. 2 µg of each POT1 and TPP1 bacmids were added to this solution and gently mixed prior to incubation at room temperature for 15 min. The bacmid solution was then added drop by drop to the plated Sf9 cells under occasional and gentle swirling. Dishes were incubated at 27°C for 3 days. To generate the P1 virus, the supernatant containing $1.2x10^6$ cells/ml was cultured in 200 ml Sf9 media in a 1 liter flask at 27°C for 3 days shaking at 125 rpm. Cells for harvested for protein purification by centrifugation at 3600 rpm for 10 min prior to freezing in liquid nitrogen. Further, P1 virus containing supernatant was harvested and stored frozen at -80°C.

For protein purification, cell pellets were resuspended in resuspension buffer (1x PBS, 250 mM NaCl, 1 mM PMSF, 1 mM DTT and three 'cOmplete mini' protease inhibitor

tablets (Roche)). Cells were lysed in a cell disruptor. The lysate was cleared by centrifugation at 20000 rpm at 4°C for 1 h. 4 ml of Glutathione Sepharose 4B resin (GE Healthcare) were added to the cleared lysate and incubated at 4°C for 1 h on a rotating wheel. The resin was then applied to a gravity flow column and washed with 250 ml of wash buffer (1x PBS, 250 mM NaCl, 1 mM DTT). Protein was then eluted using elution buffer (1x PBS, pH 7.6, 250 mM NaCl, 1 mM DTT, 15 mM glutathione). Affinity tags on POT1-TPP1 were removed by TEV-protease cleavage overnight at 4°C using 100 µg of GST-tagged TEV (in-house preparation). GST and protease were then removed using Glutathione Sepharose resin as described above. Purified POT1-TPP1 was concentrated by ultrafiltration and frozen in liquid nitrogen for storage at -80°C.

Kinetic Analysis

The intensities of RAP bands resolved by gel electrophoresis were analyzed globally using DynaFit (Fig. 6 and S5) according to the mechanism shown in Figure 6A (3, 4). All rate constants were floated, except k_{a0} and k_{d0} whose values, within limits, had little effect on the analysis. The value of k_{a0} is beyond the time resolution of the measurement (Fig. S6A) and was fixed at 1 nM^{-1} min^{-1} (with a lower limit of 0.1 nM^{-1} min^{-1}), while k_{d0} was fixed at $\leq$ 0.1 min^{-1}. The association rate constant for the products to the telomerase enzyme was assumed to have the same k_{a0} value as the primer. While this is unlikely to be strictly true, rebinding of products to the telomerase enzyme is likely to be slower, at least in the early stages of the reaction, when the hot primer remains in >5-fold excess over the sum of the dissociated products. Following a chase with 20 µM cold primer, binding of hot primer and labeled products is negligible and

allowed for a more robust analysis without any assumptions regarding the precise values of k_a. The cold chase data of Figure 6 were fitted using the "incubate" command to model the preincubation of telomerase with the hot primer (3, 4).

When modeling more than 10 sequential steps, DynaFit took many minutes to converge to a solution. The analysis could be accelerated by modeling the data in batches that overlapped by 2 repeats. For example, the estimated rate constants for the first 8 steps, obtained from fitting to the first batch of 10 steps, were set as fixed parameters in the analysis of the second batch of data which extended to 18 steps. This simplification is valid because k_f is essentially irreversible so that the steps are decoupled from each other. Such batch-wise analysis also allowed Monte-Carlo analysis to be performed on a practical time scale, to check the confidence of the fit and for any covariance between parameters (Fig. S5C and D).

We also attempted to analyze time courses for primer extension over 90 minutes without a cold chase (Fig. S4) in which substrate depletion and product rebinding could be a complicating factor, leading to distributive telomerase activity. The initial hot primer showed an initial rapid drop in concentration, followed by a slightly curved decay (Fig. S6A). The amplitude of the initial drop in primer concentration (5.3 nM) practically matched the initial burst in the sum of the first 3 dominant repeat bands (B, C and D) and provides a measure of the active telomerase concentration (5, 6). The small deviation of the subsequent primer decay profile from linearity indicates that the primer is depleted to an extent that k_{a0}[primer] is no longer >> k_{d0} + k_{f0} and/or the DNA products are rebinding competitively with the primer. The effect is equivalent to

deviation of the initial linear rate in classical steady-state enzyme kinetics due to substrate depletion and/or product inhibition. However, at the 20-minute time point, equivalent to the preincubation period in the cold chase experiment, the deviation is small (< 0.4 nM at a remaining primer concentration of 39 nM). Furthermore, when the complete time course of the first 12 repeats (bands B to M) were globally fitted using DynaFit, the saw-tooth pattern of the rate constants for sequential steps in the reaction remained (Fig. S6B).

Processivity

Processivity can be defined and derived in several ways, each with their strengths and limitations. We have summarized the processivity determined from primer extension assays using $R_{1/2}$ values which represent the median length of DNA product formed, expressed in terms of number of repeats (Fig. 1, 3 and 5) (7). This analysis assumes the distribution of products follows a near exponential function, where $R_{1/2}$ is equivalent to the half-time for decay in an exponential time course. $R_{1/2}$ is determined from the slope of a plot of ln(1-FLB) versus repeat number, where FLB is the fraction left behind (see Methods section). A $R_{1/2}$ value may be converted into an average (macroscopic) processivity value from the relationship:

$$P = \exp(-\ln(2)/R_{1/2})$$

where P represents an average probability of progressing forward and 1- P, an average probability of product dissociation. The weighting of this average processivity is biased by the logarithmic function and also depends on the magnitude and trend of

any heterogeneity in the processivity at each step in the reaction (i.e. the so-called microscopic processivity (8). The Latrick and Cech (7) plot smooths out the heterogeneity in the microscopic processivity values, which is convenient for deriving a single value for comparing reaction conditions. However, the modulation in microscopic processivity, as observed in our experimental data is of interest here (e.g. Fig. 6E).

Our kinetic analysis yields estimates of k_f and k_d for each step from which we derive the microscopic processivity; $p = k_f / (k_f + k_d)$. Microscopic processivities can also be derived directly from a single time point by the method of Peng et al. (9). For step n, p = (sum of intensities of all bands beyond n) / (sum of all band intensities beyond and including the band leading to n). This analysis assumes that the band intensities before step n represent fully dissociated products and therefore it is only accurate for early repeat numbers in our assays. Figure S6C compares the microscopic processivity values derived from the experiment shown in Figure 6B by kinetic analysis with "end-point" analysis derived from the 70 minutes post-chase data using the method of Peng et al. (9). The close agreement in values over the first 10 repeat steps demonstrates that the kinetic modeling converged to a consistent set of rate constants and that the products (bands B to K) had largely dissociated by 70 minutes after the chase (cf. Fig. 6C in K^+).

A potential source of error in applying the Latrick and Cech (7) or Peng et al. (9) methods, is the need to sum over all band intensities beyond a particular n-value, and if the band analysis is prematurely truncated at too low a total n-value or background

readings are summed into the true intensities, then a systematic deviation in the processivity value can accrue at high repeat numbers. It is therefore useful to compare all three approaches to crosscheck the analysis from each.

The low intensity intervening bands corresponding to nucleotide addition processivity (NAP) were ignored in the analysis above. The intensity of each NAP band amounted to about 5 to 20% of the neighboring RAP bands throughout the time course in K^+. This was also reflected in the higher microscopic processivity values for the NAP steps calculated by the method of Peng et al. (9), which were generally in the region of 0.97 to 0.99. This indicates that the ratio of k_f to k_d for the NAP steps were an order of magnitude higher than those for RAP. Modeling indicates this is largely a reflection of increased k_f (equivalent to k_{pol} for NAP and ~ k_{trans} for RAP in Figure 1A), while k_d values for NAP (equivalent to k_{off} in Figure 1A) are comparable to those derived for RAP. If k_f values for NAP were similar to those of RAP and the low NAP band intensity was due to a much lower k_d, then there would be a transient rise in each NAP band as the reaction progressed through that step, corresponding to bound product. This transient, which would approach the subsequent RAP band in intensity is not seen in our experimental gel time courses. Attempts to fit the NAP band intensities using DynaFit failed to converge to a robust solution for k_f and k_d. This failure resulted from the experimental noise in RAP band intensity exceeding the NAP band intensity, and hence the latter did not constrain the fit. On the other hand, analysis of simulated data showed that DynaFit was able to converge and return the input rate constants accurately for both NAP and RAP bands when they differed by an order of magnitude in intensity, in the absence of noise. This finding allowed us to test the effect of ignoring

NAP bands in the analysis of simulated data and indicated that the returned k_f values for RAP are likely within 2-fold of their correct value when NAP is ignored. This is the same magnitude as the confidence interval in rate constants determined from Monte Carlo analysis arising from experimental noise (Fig. S5C and D).

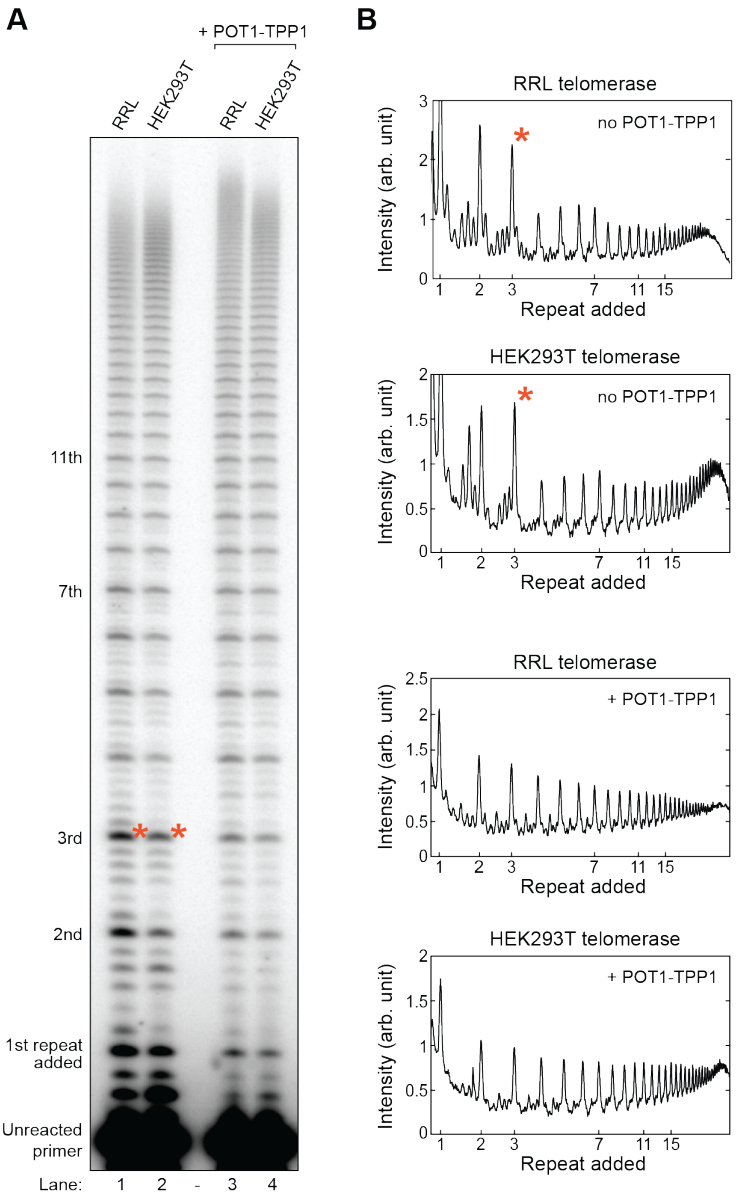

Fig. S1. RRL-reconstituted human telomerase compares to enzyme preparations from HEK293T-cells. (A) Telomerase primer extension assay using telomerase preparations from RRL or HEK293T cells as indicated above the gel. The effect of POT1-TPP1 on either preparation is assessed in lanes 3 and 4, respectively. Added repeats are indicated to the left. Red asterisk marks the high-intensity band characteristic for the 'pattern of four'. (B) Lane profiles with raw intensity versus added repeat are shown for lanes 1 to 4 of the gel in (A) (note red asterisks). The source of the respective telomerase preparation and the POT1-TPP1 condition is indicated above and within each profile, respectively.

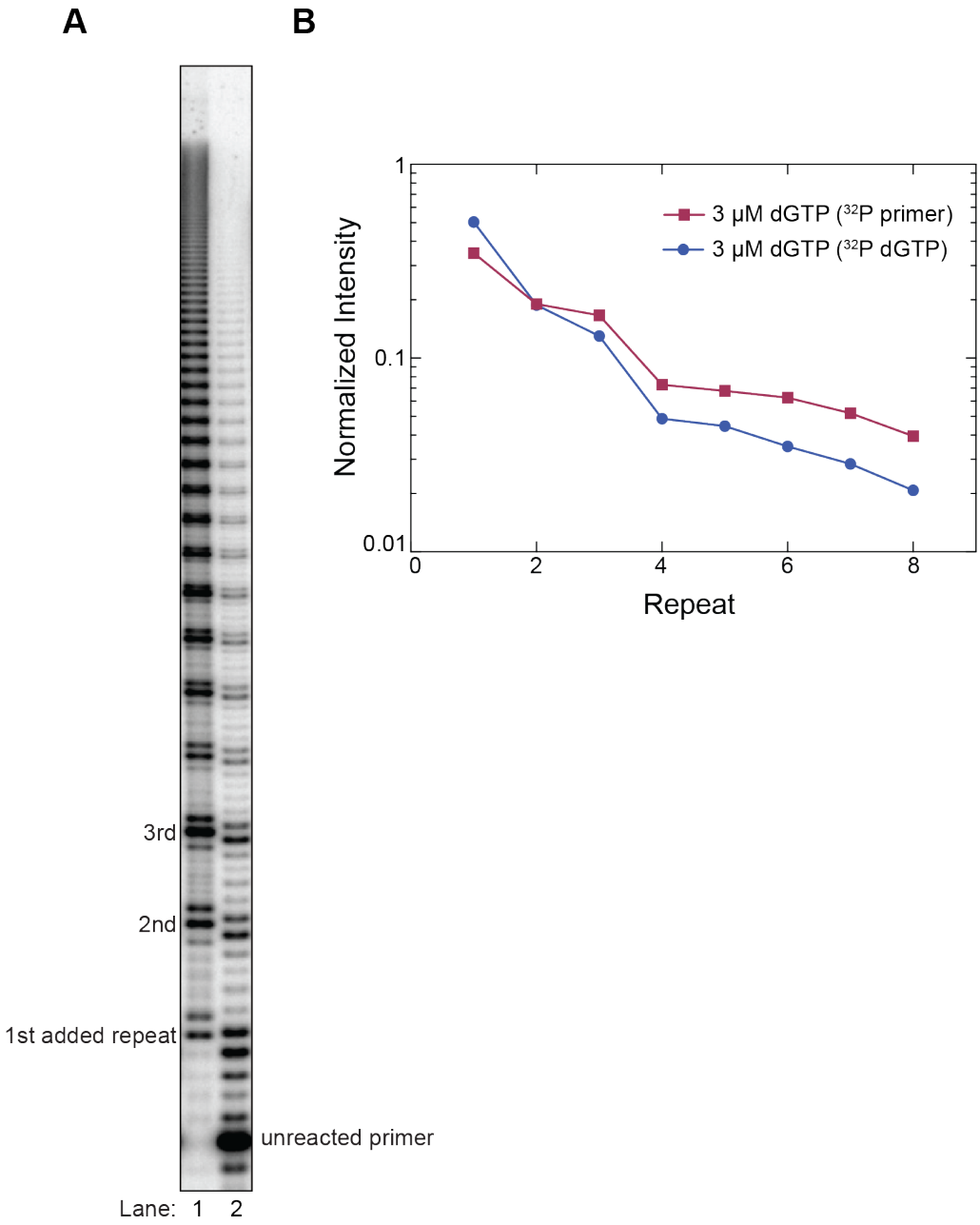

Fig. S2. Using radiolabeled dGTP or radiolabeled primer result in similar product accumulation profiles. (**A**) Telomerase primer extension assay with 3 μM dGTP and 500 μM dATP and dTTP. Repeats added to the primer are indicated to the left. Lane 1 is performed with 0.3 μM radiolabeled dGTP and 2.7 μM cold dGTP. Lane 2 is performed with 50 nM radiolabeled $(TTAGGG)_3$ primer and 3 μM cold dGTP. All assay conditions except for the identity of the radiolabeled nucleic acid are identical between the two samples. (**B**) Normalized intensity plotted vs repeat number.

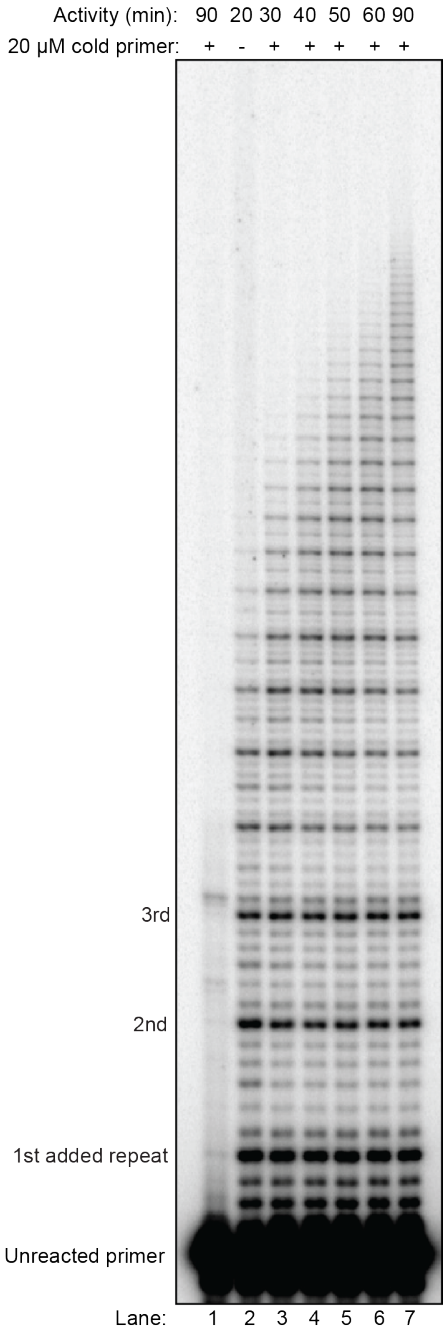

Fig. S3. Telomerase is processive in the presence of 50 nM primer. Telomerase primer extension assay with 20 μM chase primer $(TTAGGG)_3$ added after 20 minutes. Repeats added to the primer are indicated to the left.

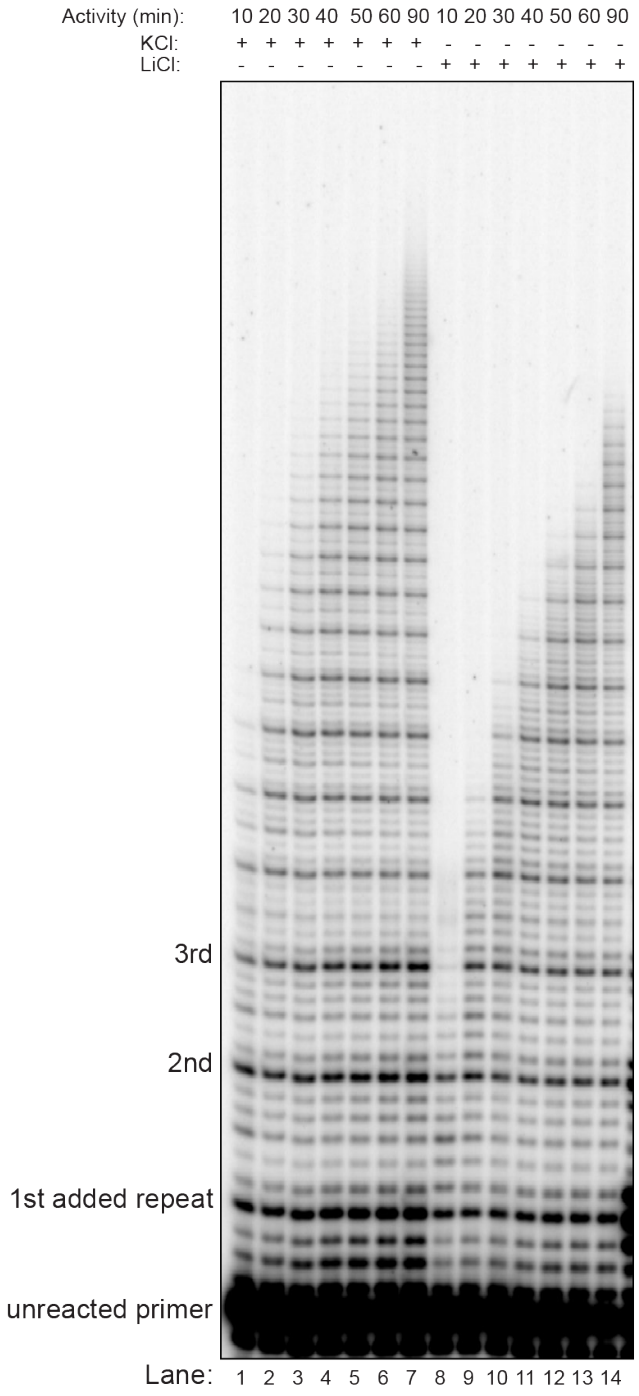

Fig. S4. Telomerase activity is slower in Li^+. Telomerase primer extension assay with samples taken at the indicated time points in either KCl (lanes 1-7) or LiCl (lanes 8-14). Repeats added to the primer are indicated to the left.

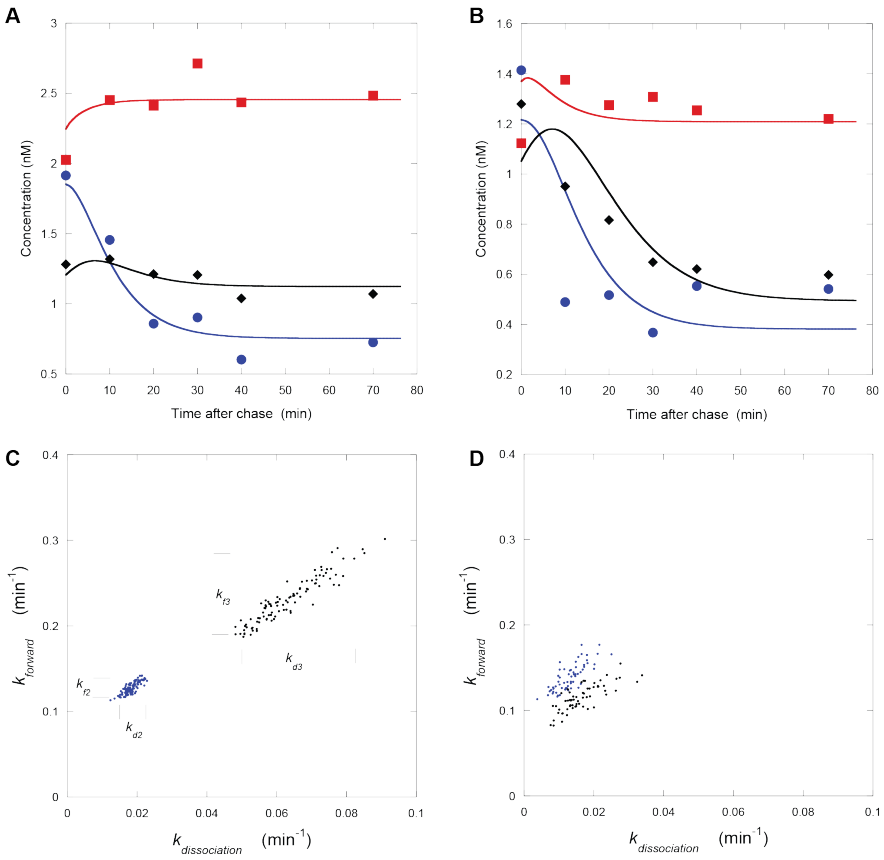

Fig. S5. Analysis of the kinetics of a primer extension assay described in Figure 6 using DynaFit (3, 4). Panels (A) and (B) are global fits for RAP bands B (red squares), C (blue circles) and D (black diamonds). These data are provided on a separate plot to Figure 6C, which shows the fits for bands E to J, because the concentrations of these early repeats are around 2 to 3-fold higher. (C) and (D). Example Monte-Carlo analysis to illustrate confidence of fitting and covariance of parameters for the scheme shown in Figure 6A. The plots show the rate constants for the forward elongation k_f and dissociation, k_d for the repeat bands, C and D (Fig. 6A) in the presence of (C) K^+ and (D) Li^+. The analysis shows that k_{f3} is about 2-fold larger than k_{f2} and k_{d3} is about 3 times larger than k_{d2} in the presence of K^+, leading to reduced microscopic processivity (k_f / (k_f+k_d)), whereas the differences in the presence of Li^+ are only marginally significant. The markers in (C) indicate the 5 and 95 percentile limits of the estimated rate constants based on over 500 iterations. This analysis indicates that the saw-tooth pattern of consecutive rate constants and the processivity observed in K^+ are significant compared with the near-featureless pattern in Li^+ (Fig. 6D). The analysis also shows that k_f and k_d for each repeat band are linearly covariant, leading to an elliptical distribution. Consequently, the microscopic processivity is better defined than the individual rate constants. No covariance is seen between pairs of other rate constants (e.g. k_{f3} versus k_{d2}), which are separated by effectively irreversible steps.

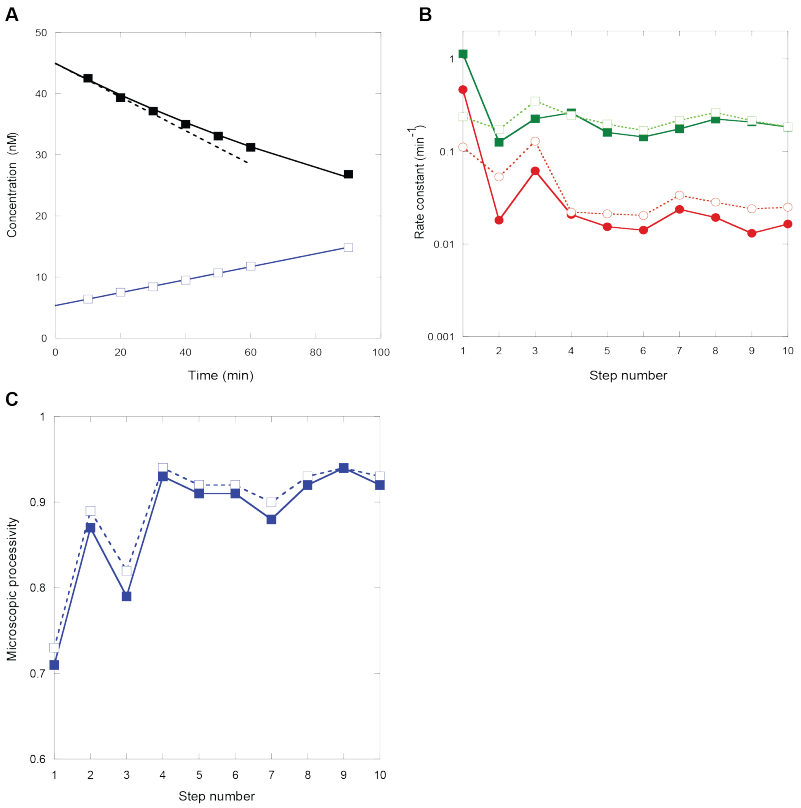

Fig. S6. Reproducibility and self-consistency of kinetic analyses. (A) Primer extension assay performed in the absence of a cold chase (Fig. S4), starting with 50 nM hot primer. Note the drop in primer concentration to 45 nM which is complete within the first time point (black solid symbols). This indicates that $k_{on} = k_{a0}$[primer] + k_{d0} + k_{f0} is rapid on the time scale of this experiment and is dominated by k_{a0}[primer] based on modeling (Fig. 6D) and literature data, $k_{d0} < 0.0006$ min^{-1} (10). The solid black line shows an exponential fit to the data, and the dashed line shows the equivalent initial rate, to illustrate the small deviation from linearity of the early time points. The initial rapid drop in primer concentration is matched by a 5 nM burst in product formation, which is dominated by the first 3 repeat products (blue open symbols = sum B + B$^{\#}$ + C + C$^{\#}$ + D + D$^{\#}$). (B) The rate constants returned by global fitting using DynaFit for primer extension assays carried out in the presence of K^+, with a 20 μM cold primer chase (solid symbols and line = experiment of Figure 6D) compared with a similar experiment (Fig. S4) in the absence of a cold chase (open symbols, dashed line) in which product rebinding may occur during the 90-minute incubation. These data indicate that the saw-tooth profiles of the rate constants (green squares = k_f and red circles = k_d) are a robust feature of telomerase that is observed using a different experimental design and a different sample preparation. (C) Microscopic processivity values calculated from rate constants derived from DynaFit (solid symbols) compared with those derived using the method of Peng et al. (9) (open symbols). The solid symbols are the same data set as shown in Fig. 6E.

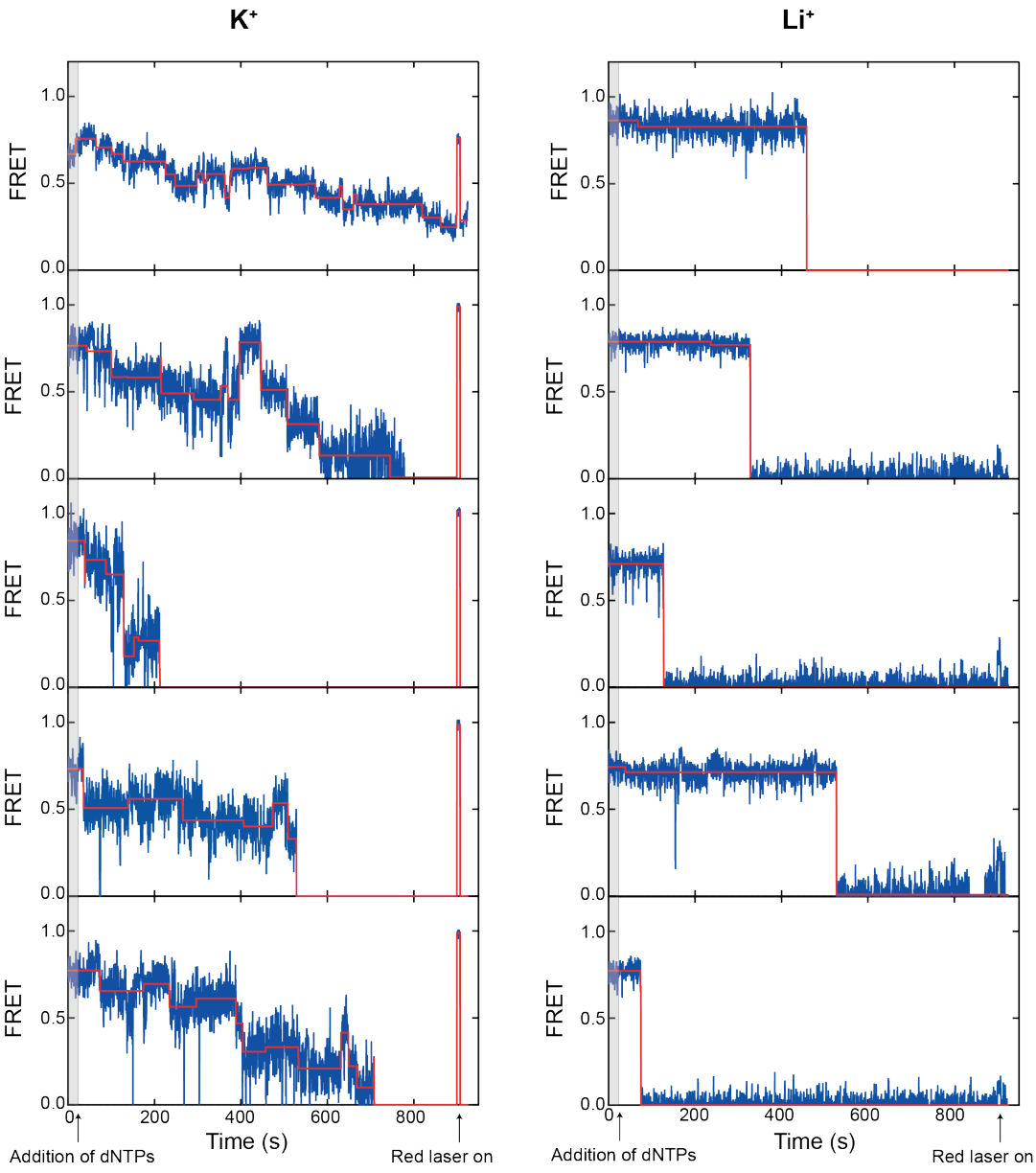

Fig. S7. Real-time smFRET traces. Representative FRET traces are shown for experiments performed in KCl (left panels) and LiCl (right panels). Steps (red) were fit to each trace using MATLAB. Red laser was turned on at 900 (s) to check for Cy5 photobleaching. dNTPs were added after 25 seconds (grey bar).

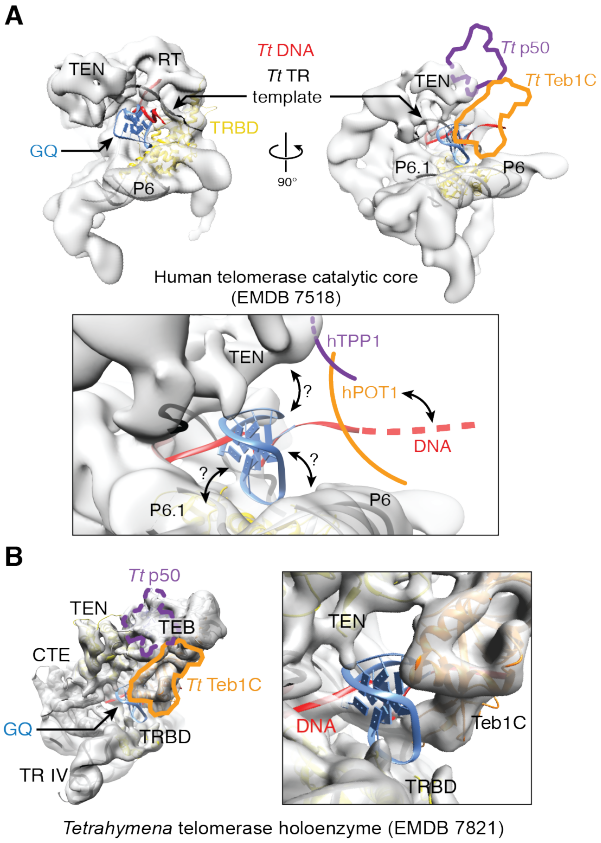

Fig. S8. Model of a GQ within the telomerase enzyme. (A) The DNA exit channel in human telomerase provides space to accommodate a GQ. Structural superposition with the *Tetrahymena* telomerase EM structure places the hPOT1-hTPP1 counterparts *Tt* Teb1 and *Tt* p50 in juxtaposition to the DNA exit upstream of the GQ (outlines at right, also see B). Bottom panel, close up of the GQ model. The distance of the GQ to the active site is below two telomeric repeats according to observations presented in this study. In this position, the GQ has access to critical elements such as the telomerase essential N-terminal (TEN) domain, the telomerase RNA binding domain (TRBD) and the hTR CR4/5 to exert its potential impact on telomerase function. Modeled coordinates, PDB ID: GQ, 2HY9 (representative GQ in presence of K^+); TR template and DNA, 6D6V; TRBD-P6-P6.1, 4O26. Human telomerase catalytic core EM reconstruction, EMDB 7518. (B) In *Tetrahymena*, the modeled GQ pocket is confined by the C-terminal domain of the TEB complex protein Teb1, illustrating how telomere binding proteins can be excluded from a GQ promoting environment prior to unfolding of the GQ upon continued repeat synthesis (Fig. 8B). Modeled coordinates, PDB ID: *Tetrahymena* TERT, TR, p50, Teb1 and DNA, 6D6V; GQ, 2HY9. *Tetrahymena* telomerase holoenzyme EM reconstruction, EMDB 7821.

Table S1. Oligonucleotides used in this study (5′ to 3′).

$(TTAGGG)_3$ primer	TTAGGGTTAGGGTTAGGG
$(TG)_3$ primer	TGTGTGTTAGGGTTAGGG
$(TG)_6$ primer	TGTGTGTGTGTGTTAGGG
hTR-PK RNA fragment 32-62	GGGCCAUUUU-5-N-U-UGUCUAACCCUAACUGAGAA
DNA splint	CAGCGCGCGGGGAGCAAAAGCACGGCGCCTACGCCCTTCT CAGTTAGGGTTAGACAAAAAATGGCCACCACCCCTCCCAGG
Biotin $(TTAGGG)_3$ primer	Biotin-TTAGGGTTAGGGTTAGGG
smFRET primer	Biotin-TTAGGGTTAGGG-(aminoT)-TAGGG
Cy5 DNA detection probe	5AmMC6-CCCTAACCCTAACCC

DNA oligonucleotides were purchased from Integrated DNA Technologies, modified RNA fragments from Dharmacon.

REFERENCES

1. Akiyama BM & Stone MD (2009) Assembly of complex RNAs by splinted ligation. *Methods Enzymol* 469:27-46.

2. Hwang H, Opresko P, & Myong S (2014) Single-molecule real-time detection of telomerase extension activity. *Sci Rep* 4:6391.

3. Kuzmic P (1996) Program DYNAFIT for the analysis of enzyme kinetic data: application to HIV proteinase. *Anal Biochem* 237(2):260-273.

4. Kuzmic P (2009) DynaFit--a software package for enzymology. *Methods Enzymol* 467:247-280.

5. Hartley BS & Kilby BA (1954) The reaction of p-nitrophenyl esters with chymotrypsin and insulin. *Biochem J* 56(2):288-297.

6. Bagshaw CR (2017) *Biomolecular Kinetics: a step-by-step guide* (CRC Press, Boca Raton) 1 Ed p 446.

7. Latrick CM & Cech TR (2010) POT1-TPP1 enhances telomerase processivity by slowing primer dissociation and aiding translocation. *EMBO J* 29(5):924-933.

8. Jarvis TC, Newport JW, & von Hippel PH (1991) Stimulation of the processivity of the DNA polymerase of bacteriophage T4 by the polymerase accessory proteins. The role of ATP hydrolysis. *J Biol Chem* 266(3):1830-1840.

9. Peng Y, Mian IS, & Lue NF (2001) Analysis of telomerase processivity: mechanistic similarity to HIV-1 reverse transcriptase and role in telomere maintenance. *Mol Cell* 7(6):1201-1211.

10. Wallweber G, Gryaznov S, Pongracz K, & Pruzan R (2003) Interaction of human telomerase with its primer substrate. *Biochemistry* 42(2):589-600.

CHAPTER IV

GUIDE TO SETUP AND EXECUTION OF SINGLE-MOLECULE MAGNETIC TWEEZER EXPERIMENTS

INTRODUCTION

Single-molecule force spectroscopy has proven to be a powerful tool for the study of biological molecules and polymers[1-2] due to their ability to impart a finely tuned degree of force on the scale of piconewtons and accurately measure the response of the molecule on the scale of nanometers[2]. The physical manipulation of these molecules offers a method to calculate and measure physical properties of these molecules that simply cannot be done by any alternative method[3]. Of the various techniques of force spectroscopy, magnetic tweezers has the added capability to impart torque on the trapped molecule, a convenient property of the technique when studying helical structures such as nucleic acids[4]. In contrast to optical tweezers, magnetic tweezers are easily calibrated and are free from laser heating and unwanted photophysical effects such as background fluorescence and photobleaching[2]. Furthermore, the ability to control the height of the magnets, and therefore the degree of imparted force, allows for the application of a continuous range of forces from the maximum applicable force to zero[5].

Magnetic tweezers also allow for the real-time detection of structural changes in biomolecules in the nanosecond to millisecond timescales[6]. Biomolecules of interest from proteins[7], RNA[8], non-canonical DNA structures[9] and others can be immobilized and attached to a magnetic bead such that structural changes can be monitored as a function of force and/or torque. Biomolecules can also be introduced to the trapped molecule in *trans* and the effect of these molecules on the trapped molecule can be studied in real time[10-11]. Small molecules can also be introduced to the trapped molecule to investigate the effect of these molecules on the physical properties of the biopolymer of interest[12]. It is because of these properties magnetic tweezers have become such a powerful tool for the elucidation of the physical properties of biological molecules and the underlying mechanisms of the proteins and enzymes that act upon them.

A magnetic tweezer experiment is typically performed in a flow cell (Figure 1). This design allows for the creation of the immobilized molecule (referred to as a tether) and the introduction of secondary molecules once the tether is established. The details of the construction of these flow cells and tethers will be discussed later in this chapter. Briefly, a flow cell is constructed such that the bottom is functionalized providing a mechanism for tether immobilization (typically by attachment of an antibody). This single surface coating imparts polarity to the channel. Non-magnetic beads (referred to as reference beads) and also bound to the surface to act as a fiduciary marker to correct for experimental drift. A bi-functionalized biological polymer (in this case DNA) is then introduced to the passivated channel (typically done by blocking with BSA)

such that only one end of the DNA molecule is competent to bind to the surface. Streptavidin coated magnetic beads are then introduced to the immobilized DNA molecule and bind to the functionalized biotinylated fragment of the DNA molecule to complete the construction of the tether. The channel is then extensively washed to remove unbound beads and DNA. The flow cell is then placed on an inverted microscope where a pair of permanent magnets can be positioned above and the extension of the DNA molecule can be measured.

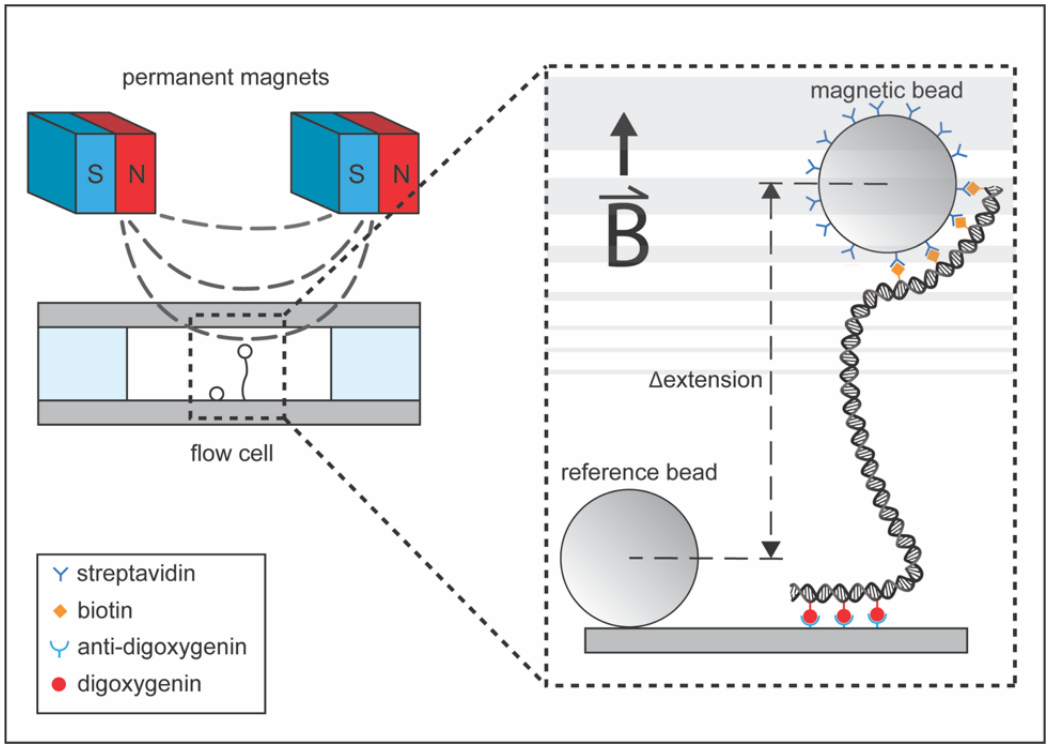

Figure 1 – Typical magnetic tweezer experimental setup. DNA molecules of interest are immobilized on a flow cell and trapped using a magnetic bead through functionalized DNA handles. A pair of permanent magnets is positioned above the flow cell and a force is imparted on the magnetic bead and therefore the DNA molecule. The extension of the molecule can be measured as a function of force by comparing the z-position of the magnetic bead to a fixed reference bead.

OVERVIEW OF THE MAGNETIC TWEEZERS

A schematic drawing of the magnetic tweezers can be seen in figure 2 (not drawn to scale) as well as the hardware controllers and the LabVIEW vi's that control them. The source of illumination for the microscope comes from a monochromatic blue LED. This LED is mounted above a brushless motor that controls the rotational position of the permanent magnets. The brushless motor is mounted to a linear stage that controls the height of the magnets above the flow cell. The flow cell is mounted on a translational stage that allows the flow cell to be moved in the x and y directions above the objective. The objective is mounted on a piezo stepper motor that controls the position of the objective (and therefore the focal plane) relative to the flow cell. Finally, the light from the objective is diverted towards the Andor camera where the images are acquired.

The linear stage is controlled by a ThorLabs DC servo controller that interfaces between the hardware and the LabVIEW vi titled "Linear Stage Control.vi" (Figure 2A). This controller is turned on when it is plugged in and has no power switch. The brushless motor is controlled by a custom made motor controller that is mounted under the shelf above the microscope and is turned on by a toggle switch. This controller is the interface between the motor and the LabVIEW vi titled "Motion Control2.vi" (Figure 2B). The XY translational stage is controlled by a Mad City Labs Inc. microdrive on the shelf above the microscope. This controller is the interface between the hardware and the LabVIEW vi titled "Keyboard MicroDrive Control.vi" (Figure 2C). The focal plane is controlled by the focus knobs on the microscope as well as a piezo stepper motor. The

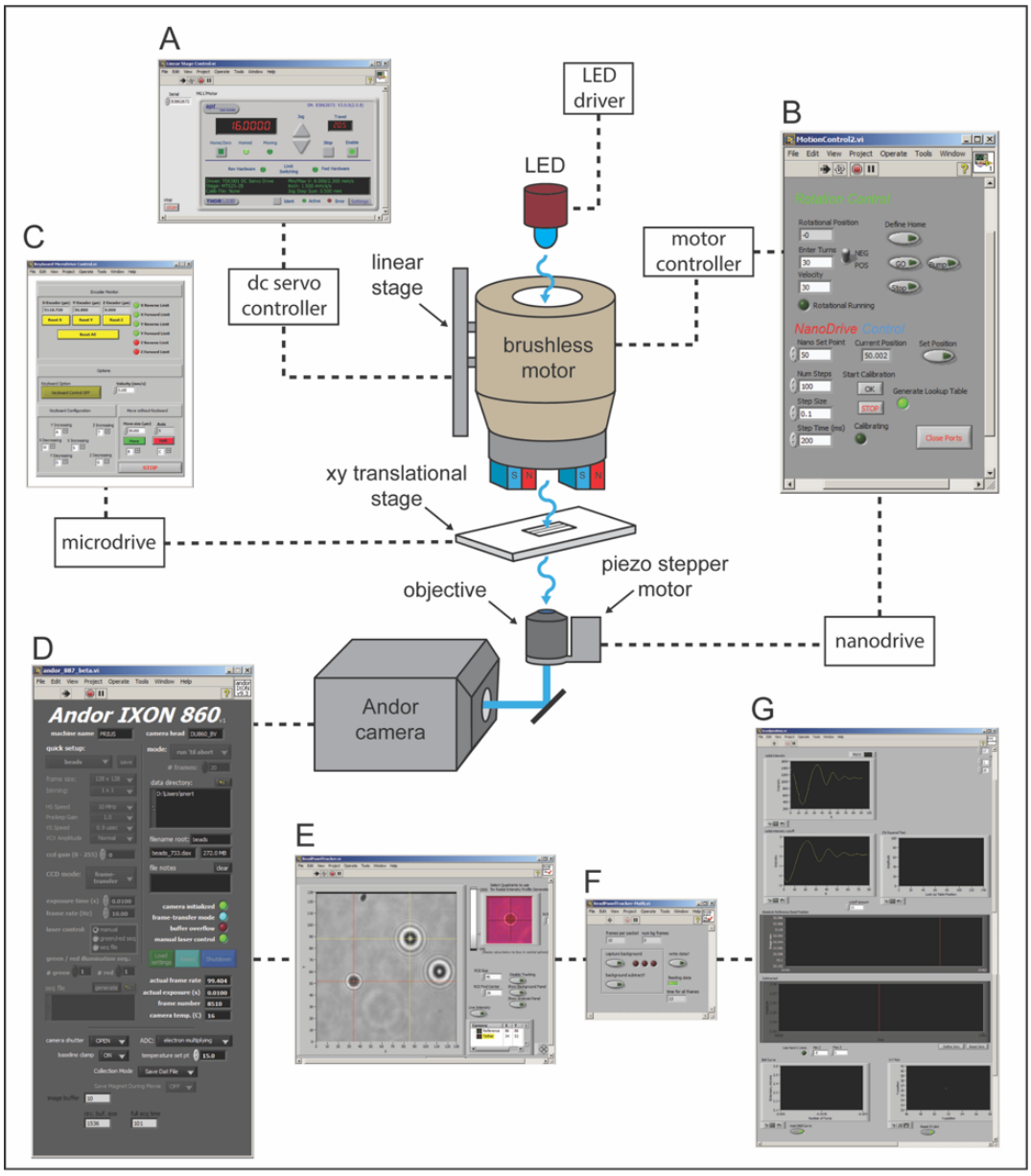

Figure 2 – Overview of the magnetic tweezers. A) Linear stage vi that controls the height of the magnets. B) Motion control vi that controls the rotation of the brushless motor as well as the position of the piezo stepper motor. C) Keyboard control vi that translates the flow cell in the x and y plane. D) Andor camera control vi that controls the camera and sets shutter state, acquisition time, and data directory. E) Bead tracking vi that sets the region of interest for bead tracking and region of interest used to find the center of the bead. F) Bead tracker math vi that performs calculation from the images and also controls weather data is written. G) Bead position vi that is the output of the calculations

piezo stepper motor is controlled by a Mad City Labs Nanodrive that is controlled by the same vi that controls the rotation of the magnets “Motion Control2.vi”. The Andor camera is controlled by “andor_887_beta.vi” (Figure 2D) which sets the shutter state, frame rate, and the directory to which the data is written. The acquired images from the camera are sent to “BeadPanelTracker.vi” (Figure 2E) which tracks the x and y position of the beads. This is where the user sets the region of interest (ROI) for both the tethered bead and the reference bead. It also sets the ROI used to locate the center of the beads. This information is then passed to “BeadPanelTracker-Math.vi” (Figure 2F) which performs calculations on the data and finally output to “BeadPosition.vi” (Figure 2G) which displays the data to the user. Each of these vi’s will be discussed in detail in the subsequent sections of this chapter.

FLOW CELL ASSEMBLY

The relationship between applied force and distance between the magnets and the tethered bead is exponential. Therefore, to maximize the applicable force on the tether, it is desirable to create flow cells that are as thin as possible. In the current configuration of the magnetic tweezer microscope, a difference of 0.5mm results in an approximate doubling of the maximum force. This does present challenges, as thin flow cells are easily fractured. The following protocol gives detailed instructions on how to create thin flow cells using two glass microscope coverslips.

Preparation of 0.2% nitrocellulose

Cut ~1cm^2 piece of nitrocellulose membrane and weigh it. Dissolve the nitrocellulose in absolute ethanol for a final concentration 0f 0.2% (w/v). **Protect this solution from light.** You will need 150μL of 0.2% nitrocellulose per flow cell, so adjust the amount of dissolved nitrocellulose membrane accordingly. Briefly vortex, then place on a room temperature rotator overnight. The next day, briefly vortex again and check to see the membrane has fully dissolved.

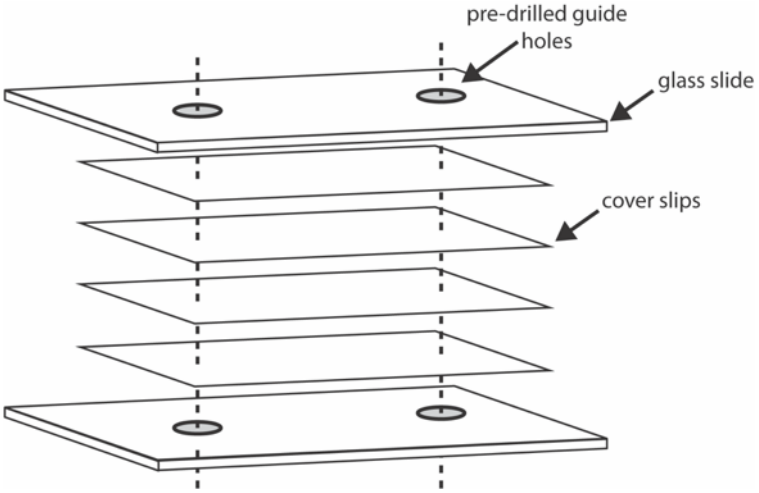

Figure 3 – Guide hole positions.

Preparation of drilled coverslips

Prepare two glass slides by drilling guide holes where the holes in the coverslips will be drilled (Figure 3). These will be used to aid in the drilling of the coverslips. Once the guide slides are prepared, place between them the desired number of coverslips (you will need one per flow cell). Be aware that some

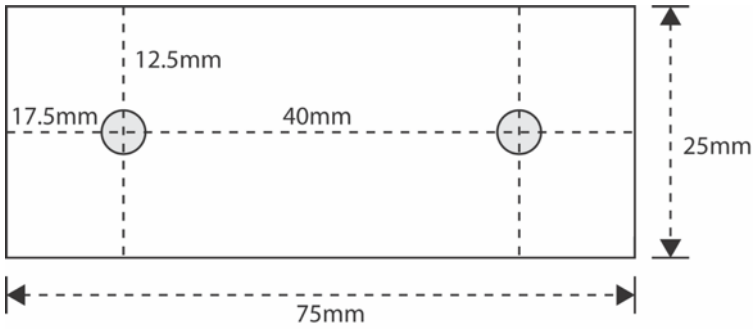

Figure 4 – Coverslip drill assembly.

coverslips might crack (usually the top and bottom ones) so it is beneficial to include a few extras. Be sure to wet all coverslips before placing them between the slides to prevent minimize cracking (Figure 4).

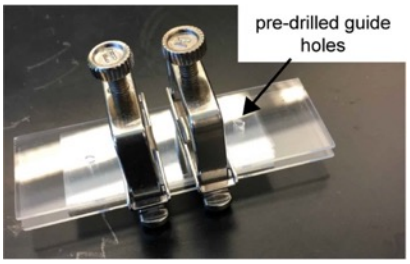

Figure 5 – Coverslips held together with hose clamps.

Once the coverslips are positioned between the two glass slides, tighten them together with two hose clamps (Figure 5). Submerge the clamped coverslips in water below the drill press. With the drill off, position the guide holes so the drill bit will pass through them. Turn the drill on, and slowly lower the bit until it lightly touches the first coverslip through the guide hole. After it touches, move the drill bit up again to clear the hole of glass shards. Continue to drill through the rest of the coverslips using a light, tapping motion, each time clearing the hole of glass shards. Continue until the bit passes through the lower guide hole of the bottom glass slide. Once the drilling is completed, remove the clamps and inspect all the drilled coverslips for small cracks around the holes, discarding ones with visible cracks. The coverslips are now ready to be cleaned.

Cleaning of the coverslips

1. Each flow cell will require one coverslip, and one drilled coverslip. The cleaning procedure is the same for both.
2. With a gloved hand, lightly wash both a coverslip and drilled coverslip per flow cell with Alconox. Place them into a slide holder containing ~5% (w/v) Alconox solution and sonicate for 10 minutes.

3. Rinse thoroughly with dH_2O, and sonicate in dH_2O for 10 minutes in a cleaned slide holder.
4. Sonicate for 10 minutes is acetone.
5. Directly transfer to 1M KOH and sonicate for 10 minutes. Thoroughly rinse with dH_2O and nitrogen dry both coverslips. Plasma clean both for 5 minutes.

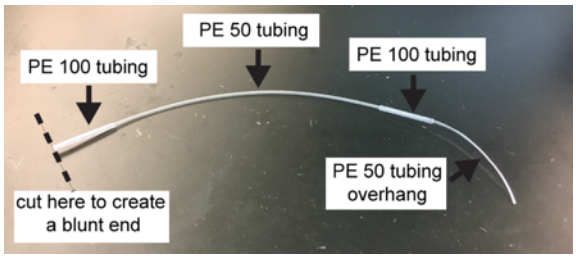

Figure 6 – Outlet tubing assembly.

Assembly of the flow cell

First assemble the flow cell outlet tube. Take a ~10cm piece of Intramedic PE 50 tubing and "draw-out" the ends by pulling so the outer diameter is small enough to fit through a piece of Intramedic PE 100 tubing inner diameter. Cut off the terminal ends at an angle to allow for easy insert into the PE 100 tubing.

Insert the cut ends of the PE 50 tubing into a ~2cm piece of Intramedic PE 100 tubing at both ends, pulling the PE 50 tubing sufficiently through the piece of PE 100 tubing to create a tight seal. At one end, cut through the PE 100 tubing to create a blunt end. At the other end, leave ~ 2cm of a PE 50 tubing overhang (Figure 6).

Insert the PE 50 overhang of the outlet tubing through one of the drilled holes in the coverslip. It is useful to suspend the coverslip and attach a weight (such as a binder clip) to the PE 50 overhang to keep the PE 100 tubing flush against the coverslip

(Figure 7). Cut a ~1cm long piece out of the center of a P1000 pipette tip to act as a reservoir. Position the reservoir over the other drilled hole in the coverslip. It is useful to place a P20 pipette tip through the P1000 tip reservoir and drilled hole to act as a guide and hold the reservoir in place. Once both the outlet tubing and P1000 tip reservoir are in place, glue both with 5-minute epoxy. Be sure keep the glue only on the outside of the P1000 tip reservoir.

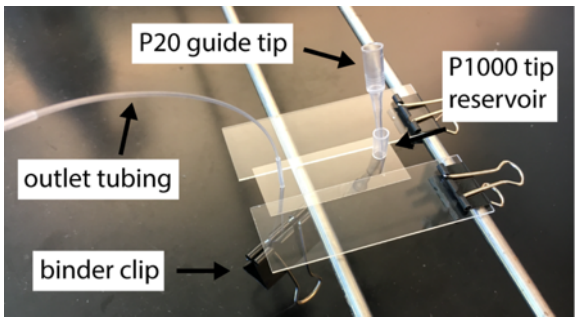

Figure 7 – Fluidics assembly.

Once the glue has dried, the PE 50 tubing overhang must be cut off from the underside of the coverslip. This is best done with a heated razorblade. The razorblade must be hot enough to easily cut through the tubing, but not too hot as the glass coverslip will break. Typically holding the tip of the razorblade in a propane torch for ~3 seconds is sufficient.

Now the flow channel must be assembled. Cut a piece of GRACE bio-labs adhesive to the same size as the cover slips. Using a clean razorblade, cut a ~35mm long 4mm wide channel out of the middle of the adhesive. It is crucial the corners of the channel meet nicely without cutting too far or the channel will leak.

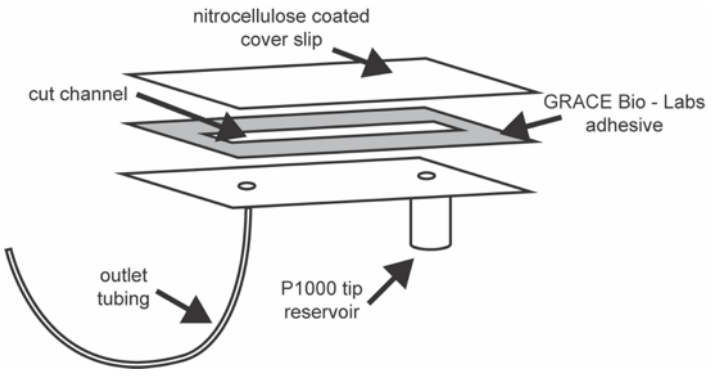

Figure 8 – Flow cell assembly.

Invert the coverslip with the outlet tube and P1000 tip reservoir so the drilled holes are facing up. Pull off one side of the plastic that covers the GRACE bio-labs adhesive and carefully place it onto the inverted coverslip such that the drilled holes align with the center of the cut channel (Figure 8). Remove the other plastic layer from the adhesive. Take a nitrocellulose coated coverslip and place it over the inverted coverslip, nitrocellulose coated side facing down (Figure 8). Using a razorblade, cut off excess adhesive. Take the assembled flow cell and place it on a flat surface with the reservoir and outlet tube facing up. Using a P1000 pipette tip, apply light pressure to all sides surrounding the cut channel to ensure a tight seal (Figure 9).

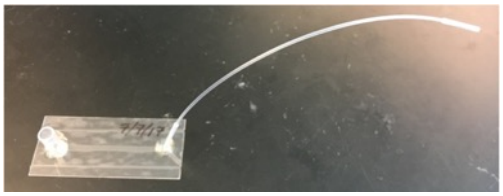

Figure 9 – Assembled flow cell.

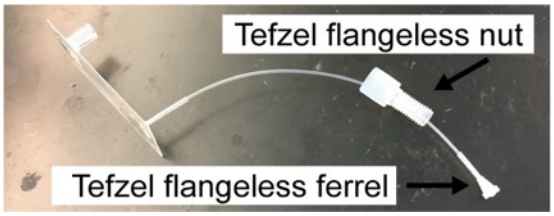

Figure 10 – Tevzel nut assembly.

Slide a Tefzel flangeless nut over the outlet tube. To the blunt PE 100 end of the outlet tube, fit a Tefzel flangeless ferrule (Figure 10). To the flangeless nut, attach a Hamilton valve (Figure 11). In a similar way the outlet tube was attached to the Hamilton valve, attach a piece of PE 100 tubing to the other side of the Hamilton valve with a flangeless nut and ferrule (Figure 11). This is where the vacuum will be applied. The flow cell is now complete.

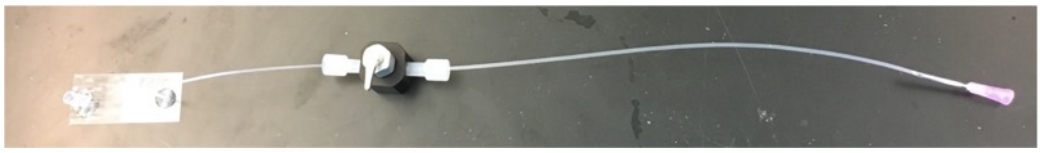

Figure 11 – Completed flow cell.

PROTOCOL FOR TELOMERE MOLECULE ASSEMBLY FOR MAGNETIC TWEEZER EXPRIMENTS

Telomeres in the cell are heterogeneous in length, ranging from 2 – 20kbp. Due to their repetitive nature, reconstruction of these DNA sequences *in vitro* presents many challenges, as they are not amenable to the standard tools typically used in molecular biology. Consequently, many *in vitro* experiments using telomeric DNA substrates have been limited to DNA lengths that can be created synthetically, and often include non-physiological sequences to aid in experimental setup and design. This section will outline a protocol describing the creation of long, uninterrupted doubled-stranded telomeric DNA molecules up to lengths of ~15kbp for magnetic tweezer experiments.

To trap the DNA molecule, two chemically modified sections of DNA are needed (referred to as handles) each containing a specific chemical modification, biotin and digoxygenin (Figure 12). These chemical modifications are introduced by using a modified dNTP in a ~1kbp PCR spanning the multiple cloning site of a pUC19 plasmid, with a BamH1 site roughly in the center of the amplicon. After PCR, the

product is digested with BamH1 generating two roughly identical products with a BamH1 sticky end. Two complimentary oligo nucleotides are then annealed together (referred to as adapters) such that one end has an overhang complimentary to the BamH1 sticky end and the other complimentary to a unique telomeric DNA sticky end. A ~576bp telomere fragment with complimentary sticky ends is generate by restriction enzyme digest of a pRST5 plasmid with the type IIS restriction enzymes Bbs1 and Bsmb1. The telomere fragment is first ligated to a DNA handle in a 1:1 ratio so the fragment can no longer circularize. Then excess telomere fragment is added resulting in concatenation as well as circular by products. The extended products are then capped by ligation of the other DNA handle and gel purified.

DNA handles preparation protocol

Table 1: PCR primers

pUC19 forward primer	5' – ACATTTCCCCGAAAAGTGCCA – 3'
PUC19 reverse primer	5' – TCAAGTCAGAGGTGGCGAAAC – 3'

Perform two separate 800µL PCRs, one using a biotin-modified dUTP, one with a digoxygenin modified dUTP.

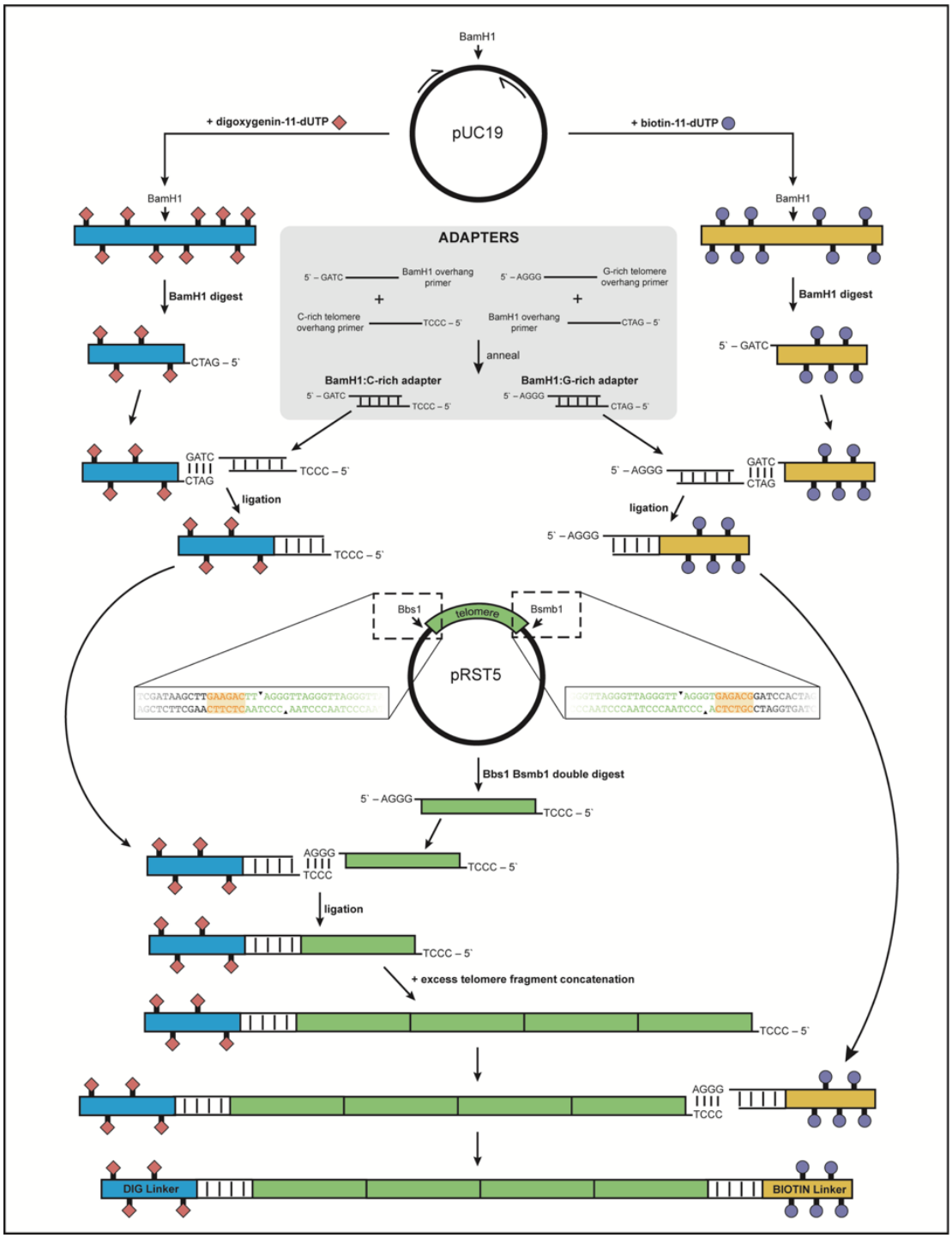

Figure 12 – Telomere molecule construction. DNA handles are in blue and yellow. The ~576bp telomere fragment is in green.

Reaction Setup:

10X Taq buffer:……...80µL

Forward primer…….. 250nM

Reverse primer……250nM

pUC19 template……..100ng

10mM dNTPs……...40µL

1mM Biotin/digoxygenin dUTP……..8µL

Taq DNA polymerase…….8µL

Nuclease free water……to 800µL

Split this into eight 100µL volume PCR tubes for the reaction.

Thermocycler Parameters

Denature at 95ºC for 2 minutes.

_____

Denature at 95ºC for 45 seconds

Anneal at 59ºC for 30 seconds

Extension at 68ºC for 45 seconds

30 cycles

_____

Final extension 68ºC for 10 minutes.

Once the PCR is complete, combined all tubes and perform a PCR cleanup splitting the material over six spin columns and eluting in 50µL of nuclease free water per column. Yields are typically 300µL of ~100ng/µL DNA.

Restriction Enzyme Digest

300µL DNA (~30µg)

20µL BamH1-HF at 100,000U/µL

35.6µL 10X CutSmart® buffer

37ºC overnight

Once the restriction enzyme digest is complete, perform a PCR cleanup splitting the material over three spin columns and eluting in 50µL of nuclease free water per column. Yields are typically 150uL of ~150ng/µL DNA.

DNA Adapter Annealing

BamH1 overhang for adapter ligation	5' – /5Phos/GATCCAGTCTGCGTACAGTGG – 3'
CCCT telomere overhang for adapter ligation	5' – /5Phos/CCCTCCACTGTACGCAGACTG – 3'
AGGG telomere overhang for adapter ligation	5' – /5Phos/AGGGCCACTGTACGCAGACTG – 3'

Table2: Oligonucleotides used for adapters

Annealing conditions:

45µL of 100mM BamH1 overhang oligonucleotide

45µL of 100mM CCCT or AGGG overhang oligonucleotide

10µL of 10X T50 buffer

Combine all reagents in a tube and place in a 95ºC heat block for 5 minutes. Once complete, remove the heat block and place on the benchtop and allow to come to room temperature (about 20 minutes).

Adapter ligation

150µL of DNA handle DNA

8X molar excess of DNA adapter DNA

10µL 10mM ATP

10µL T4 DNA ligase at 2,000,000U/mL

20uL 10X T4 DNA ligase buffer

Nuclease free water to 200µL

16ºC overnight

Once the ligation is complete, gel purify the DNA material on a 0.6% agarose gel and elute in 50µL nuclease free water. Yields are typically ~100ng/µL.

576bp telomere fragment preparation protocol

Prepare the pRST5 plasmid by performing a MaxiPrep. Grow 6X 1L cultures. The telomere fragment is prone to slip replication, and as a consequence some cultures will contain plasmids with telomere fragments of a varying length. A diagnostic double restriction enzyme digest should be performed with BamH1-HF and HindIII-HF to select for cultures that contain plasmids that have the proper length telomere fragment (Figure 13). Discard any cultures that contain telomere fragments of improper length and prepare the others.

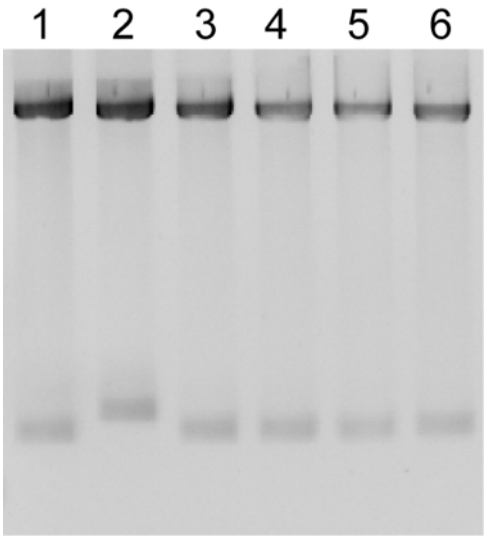

Figure 13 – pRST5 diagnostic double restriction enzyme gel. Lanes 1 – 6 are digestion products from different 1L cultures. Lane 2 corresponds to a culture that has undergone slip replication of the telomere fragment.

<u>Bbs1 Bsmb1 double restriction enzyme digest</u>

300µg pRST5

20µL Bbs1 at 10,000U/mL

2.5µL BSA

35µL 10X NEB buffer #2

Nuclease free water to 350µL

37ºC for 2 hours. To the above, add:

20µL BsmB1 at 10,000U/mL

2.5µL BSA

5µL 10X NEB buffer #2

22.5µL nuclease free water

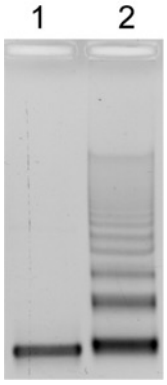

Figure 14 – Autioligation gel. Lane 1 is the telomere fragment in the labsence of ligase. Lane 2 in the autoligated fragments showing circular products, dimers, trimers, and higher order oligomers.

Following restriction enzyme digestion, split the reaction into two tubes and perform a phenol/chloroform extraction followed by an ethanol precipitation to remove excess enzyme. Resuspend the pellets in 50µL of nuclease free water each. Load each on a 0.6% agarose gel and purify the fragment by electroelution. Typical yields are ~50ng/µL.

To check if the prepared telomere fragment is competent to ligate, an autoligation reaction should be performed where the fragment will form circular products, dimers, trimers, and other higher order oligomers (Figure 14).

<u>Autoligation reaction</u>

500ng of DNA

2µL T4 DNA ligase at 2,000,000U/mL

2μL 10X T4 DNA ligase buffer

2μL 10mM ATP

Nuclease free water to 20μL

16ºC for 1.5 hours

Telomere molecule ligation

The first ligation reaction is the seeding reaction, where one DNA handle is ligated to a 1:1 molar ratio of the telomere fragment. Either handle can be used in this reaction, however it is best to start with the handle of lowest concentration, as the final ligation will use excess handle to promote complete ligation. After this is the concatenation reaction where the telomere molecules are extended, followed by the capping reaction, where the other DNA handle is ligated to the telomere molecules.

<u>Seeding ligation reaction</u>

600ng telomere fragment

1:1 molar ratio of DNA handle

2μL 10mM ATP

2μL 10X T4 DNA ligase buffer

2μL T4 DNA ligase at 2,000,000U/mL

16ºC for 30 minutes

Concatenation reaction

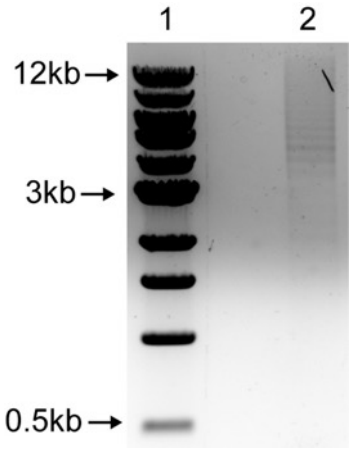

Figure 15 – Telomere molecule gel. Lane 1 is a marker. Lane 2 is the prepared telomere molecules.

Prepare a telomere master mix:

4µg telomere fragment

7µL 10mM ATP

10X T4 DNA ligase buffer for a final concentration of 1X

Store the telomere master mix on ice. Every 30 minutes, add 14µL of the master mix along with 1µL of T4 DNA ligase to the seeding reaction. This slow addition is to prevent the formation of unwanted circular byproducts (do not add T4 directly to the master mix). This process typically takes 3-6 hours.

Capping reaction

4:1 molar ratio of DNA handle to the handle used in the seeding reaction

2µL 10mM ATP

1µL T4 DNA ligase at 2,000,000U/mL

10X T4 DNA ligase buffer for a final concentration of 1X

16ºC overnight

Bring up the volume to 200µL with nuclease free water and perform a phenol/chloroform extraction followed by an ethanol precipitation. Resuspend the DNA pellet in 15µL nuclease free water and add 3µL of 80% glycerol. Load the entire sample on a 0.6% agarose gel pre-stained with 2X SYBR safe stain. Run the gel at 120V for 35 minutes. Using blue light excitation, excise the gel slice containing the higher molecular weight products (the band should appear as a very faint smear just below the well). Electroelute the DNA molecules and perform an ethanol precipitation to reduce the volume to 65µL, resuspend in nuclease free water. Take 15µL of this material and load it onto a 0.75% agarose gel pre-stained with 1X ethidium bromide. There should be faint bands corresponding to higher molecular weight DNA molecules (Figure 15).

Final DNA repair treatment

For a molecule 15kpb long, approximately 30 ligations must take place. If one of these ligations failed to ligate both strands, the DNA will be nicked and cannot be supercoiled on the magnetic tweezers. New England Biolabs offers a product called preCR® repair mix, which employs a cocktail of enzymes to repair DNA nicks.

prCR® reaction

20µL of DNA

1μL of NAD^+

2μL dNTPs

1μL enzyme mix

5.9μL 10X buffer

37ºC for 30 minutes, 4ºC overnight

The following day, add 2μL of dNTPs and 1μL NAD^+ and incubate for 30 minutes at 37ºC. Perform a phenol/chloroform extraction followed by an ethanol precipitation and resuspend in 50μL of TE buffer. At this point, the DNA is too dilute to measure the concentration by UV–vis spectroscopy so the amount to use for magnetic tweezer experiments will need to be determined empirically on the microscope, however typically a 1:50 dilution works well.

PROTOCOL FOR TELOMERE MOLECULE IMMOBILIZATION

DNA molecules used for magnetic tweezer experiments are immobilized by a series of incubations. First, anti-digoxygenin antibodies are bound to the nitrocellulose-coated surface of the flow cell. The flow cell is the passivated by incubation of a BSA blocking buffer. DNA containing digoxygenin chemical modifications in then incubated to bind to the antibody-coated surface. The channel is then washed with blocking buffer to remove any unbound DNA. Pre-blocked streptavidin-coated magnetic beads are then introduced to the flow cell and bind to the biotinylated DNA molecules. The flow cell is then expensively rinsed to clear out any unbound magnetic beads.

Resuspend lyophilized anti-digoxygenin in 1mL of 1X PBS containing 0.02% NaN_3. Add ~40uL to the flow cell (this volume can be reduced if the flow cell channel width is thin, ~3mm). Place the flow cell in a humidity chamber and incubate at 4ºC overnight.

Prepare 1mL of blocking buffer:

100µL of 10X PBS

250µL of 20mg/mL BSA

650µL nuclease free water

Slowly flow 100µL of blocking buffer into the flow cell. Allow this to incubate at room temperature for 1 hour. Place a swinging jaw compression clamp on the outlet tube to prevent the channel from drying. At this point, the magnetic beads should be blocked as well. Vortex the stock magnetic beads for 1 minute. Add 5 µL of beads to 45µL of blocking buffer and briefly vortex. Place this on a rotator at 4ºC and incubate for 1 hour.

Dilute the DNA molecules into an empirically predetermined volume of blocking buffer to a final volume of 100µL. Slowly flow this into the flow cell ~25µL at a time, with 10 minutes between each addition at room temperature. After the final addition, allow the DNA to incubate for 30 minutes.

Dilute the pre-blocked magnetic beads 1:10 in blocking buffer for a final volume of 100μL. Slowly flow this into the flow cell ~25μL at a time, with 10 minutes between each addition at room temperature. After the final addition, allow the magnetic beads to incubate for 30 minutes.

Prepare 1mL of imaging buffer. The composition of the imaging buffer will vary depending on the particular experiment, but should typically contain 0.5% BSA and always be sterile filtered through a 0.2μm filter. Add 100μL of imaging buffer to the flow cell reservoir while the compression clamp is still closed. Elevate the flow cell above to end of the outlet tube to create a siphoning effect. Slowly open the compression clamp to a point where imaging buffer is flowing at an approximate rate of 20μL/min (this is difficult to visualize and should be determined empirically). Continue to add imaging buffer to the flow cell until 1mL of imaging buffer has passed through the channel. The flow cell is now ready to be placed on the microscope.

MAGNETIC TWEEZER MICROSCOPE OPERATION

Startup procedure

Turn on the computer, Nanodrive (Figure 16A), Microdrive (Figure 16B), motor controllers (Figure 16C), dc server controller (Figure 16D), and LED driver (Figure 16E). On the desktops of the PC, double click “Start Magnetic Tweezers”, all the LabView vi’s will open. On the Andor IXON 860 vi, click the run button (Figure 17, red square). This will start the vi, as well as the

Bead Tracker, Bead Tracker Math, and Bead Position vi’s. Click run on the Motor Control2, Keyboard Microdrive Control, and Linear Stage Control vi’s. On the Andor IXON 860 vi, set the exposure time to 0.01s (Figure 17, green square). Set the

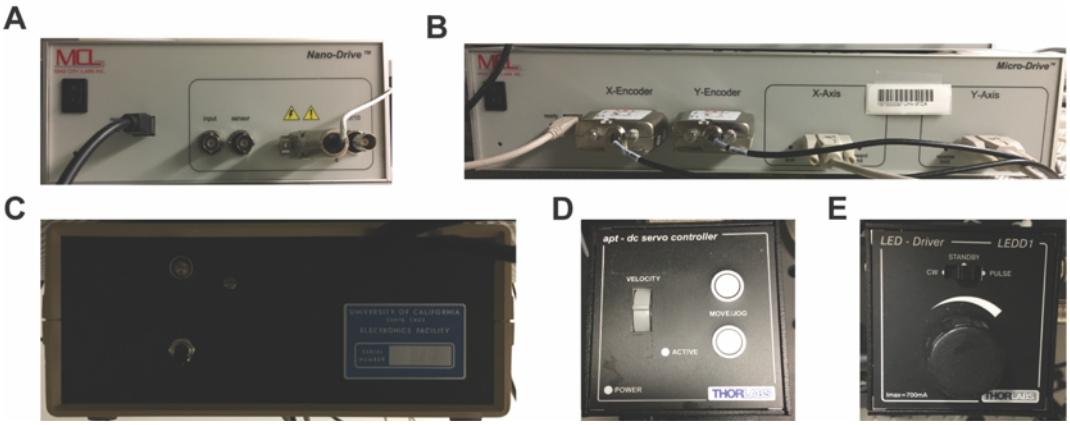

Figure 16 – Magnetic tweezers controllers. A) Nanodrive that controls the piezo stepper motor. B) Microdrive that controls the xy translational stage. C) Motor controller that controls the brushless motor. D) DC servo controller that controls the linear stage. E) LED driver that controls the LED.

Figure 17 – Andor XION 860 vi. The button in red square starts the vi. The numerical input in the green square sets the exposure time and frame rate. The drop down menu in the blue square sets the shutter state. The button in the yellow square loads all the settings that have been changed.

shutter state to open (Figure 17, blue square). Click load settings (Figure 17, yellow square). At this point, the camera is ready but not collecting or writing data. To start collecting data, press the space bar. To stop, press the space bar again.

Before beginning an experiment, it is important to home the linear stage to prevent the magnets from touching the slide and potentially damaging the objective and piezo stepper motor. On the Linear Stage Control vi, click “Home/Zero” (Figure 18, red square). The stage will move to

the top position and the position on the vi will read zero. Now set the maximum magnet position so the magnets cannot move past the top of the flow cell. In the Linear Stage Control vi, click the settings button (Figure 18, blue square). In the dialog window that appears, click in the stage/axis tab and set the max position to 20.5 (this might vary depending on the flow cell you are using, so it is a good idea to manually lower the

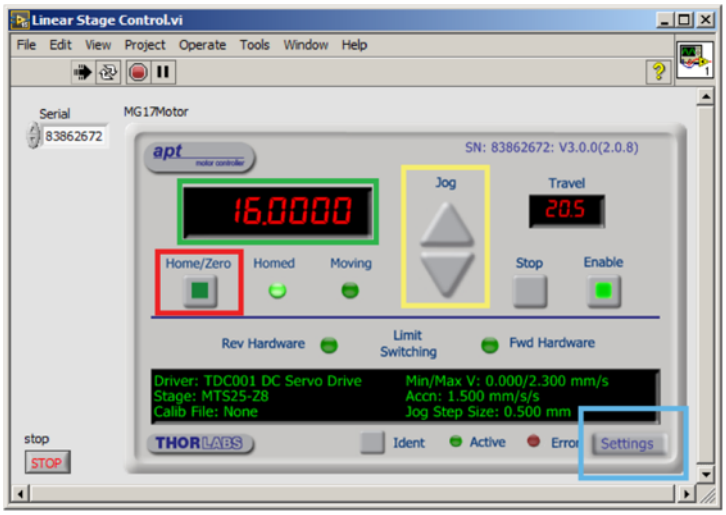

Figure 18 – Linear Stage Control vi. The numerical input in the green square moves the magnets to a given position. The buttons in the yellow square moves the magnets in increments of 0.5mm. The button in the red square homes the magnets. The settings tab in the blue square opens the dialog menu the set the maximum magnet position.

magnets using the toggle switch on the dc servo controller and visually inspect how close the magnets are, and then set the maximum position to the number displayed on the vi). **It is important to note:** the magnets will move past this position if you are controlling them with the toggle switch on the dc servo controller, or if you use the jog buttons on the Linear Stage Control vi (Figure 18, yellow square). This only limits the magnet position when using the numerical input on the Linear Stage Control vi.

Molecule locating, tracking, and z position calibration

The xy translational stage is controlled by the keys W up, S down, A right, and D left. Using the oculars on the microscope, translate over the slide until a molecule used for study is located. The optimal magnet height for locating a molecule is 16.0mm. At this height, the molecules will be in a different focal plane than the reference beads which will optimize contrast, while also having sufficient fluctuations in x and y positions that distinguish them from magnetic beads stuck to the surface of the chamber. There should be a reference bead in close proximity to the tether, but not too close that the diffraction rings overlap as that will cause errors in the centroid tracking software.

Once a molecule is located, it should be checked to be torsionally constrained. Divert the image to the Watec camera by pulling the sliding lever on the right side of the microscope out, the image will be displayed on the screen on the laser table. Adjust the focus on the microscope so the magnetic bead is in focus and there are no visible diffraction rings. If the molecule is torsionally constrained, supercoiling the molecule by rotating the magnets will cause the DNA to buckle, the extension of the molecule

will decrease, and the bead will move out of focus causing diffraction rings to appear. The amount of turns needed to buckle the DNA is dependent on the length of the tether. For a 3μm long molecule, 30 positive turns will result in diffraction rings appearing with a magnet height of 16.0mm. Set the number of turns on the numerical input on the Motion Control2 vi under rotation control (Figure 19, red square). Set the turn velocity to 30 (Figure 19, blue square). To start the motor, press go (Figure 19, green square). Regardless of whether or not the molecule buckles, the magnets should be returned to zero to relax all other tethers on the slide. Flip the toggle switch to negative (Figure 19, yellow square) and press go.

Figure 19 – Rotation control vi. The numerical input in the red square sets the amount of turns. The numerical input in the blue square set the rotational velocity. The toggle switch in the yellow square set the rotation direction. The button in the green square starts the motor.

Now the z position of the molecule must be calibrated. This is done by tracking the reference and tethered beads and at various objective positions, where a radial intensity profile of the diffractions rings is generated for each bead at each position, referred to as a look up table (LUT). Then the objective position is held constant, and by comparing the radial intensity profile of the beads to the profiles in their respective LUT, the z position is determined. Start by diverting the image to the Andor camera by turning the knob of the front of the microscope to the camera (make sure the slider on the right side of the microscope is in). Click on the Andor XION 860 vi and press the spacebar to start collecting images. Lower the magnets to the lowest position to hold the tethered bead as still as possible while generating the LUT. Center the tethered

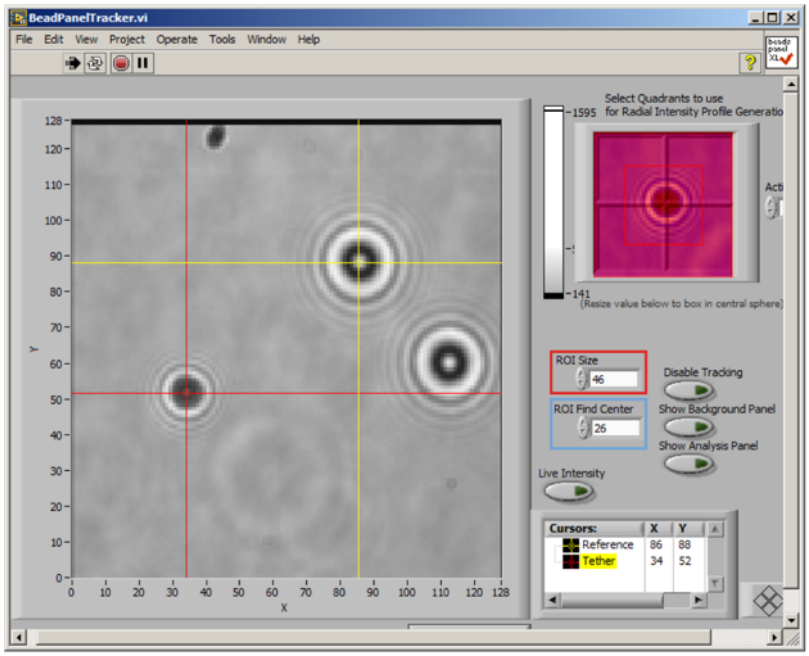

Figure 20 – Bead Panel Tracker vi. ROI size is used to determine the RIO for generating the radial intensity profiles. RIO find center is used to determine the RIO for centroid tracking of the beads.

bead and reference bead on the Bead Panel Tracker vi (Figure 20). Set the region if interest (RIO) size to 46 (Figure 20, red square) and RIO find center to 26 (Figure 20, blue square). Left click on the center of the reference bead and right click on the center of the tethered bead to begin tracking the beads.

Now the LUT must be generated. The number of steps (i.e., the number of radial intensity profiles generated) used in the LUT should always be 50nm apart, however the amount of steps will depend on the length of the tether. It is good practice to have a LUT with a length that is 4μm longer than the length of the tether to account for experimental drift. For example, a tether with a length of 3μm should have a LUT with 100 steps, with 50nm between each step making the total length of the LUT 5μm. Once the LUT is generated, the objective should be set to a position 2μm above the

bottom of the LUT so there is 2μm of room for drift above and below the length of the tether. Adjust the focus on the microscope so the starting radial intensity profile for the tethered bead has 2 – 3 peaks. Always finish changing the focus by rotation the knobs counterclockwise, as rotating them clockwise will lead to the focal plane drifting over time. It is good practice to let the microscope sit for ~10 minutes before generating the LUT to minimize drift during calibration. The default Nano set point is 50. Set the number of steps using the numerical input in the Nano Drive Control panel in the Motion Control 2 vi (Figure 21, red square). Set the step size to 0.05μm using the numerical input in the Nano Drive Control (Figure 21, blue square). Press "Start Calibration" on the Nano Drive Control (Figure 21, green square). Once the calibration is complete, set the Nano Set Point back to 50 (Figure 21, yellow square) and repeat the calibration. After the second calibration, Set the Nano Set Point to 52.

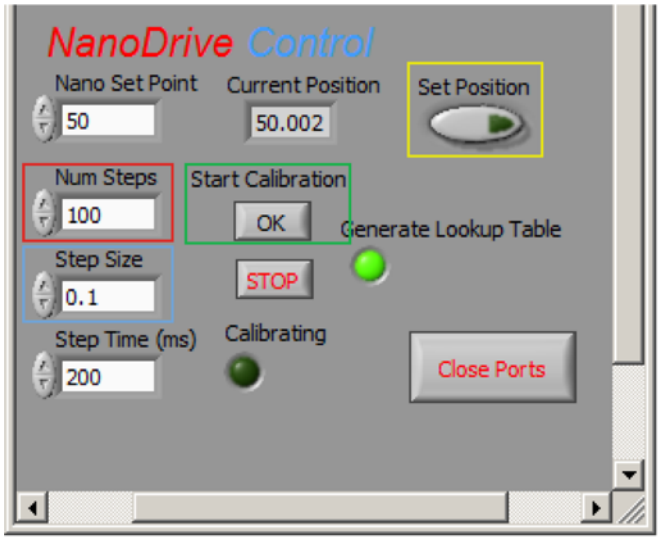

Figure 21 – NanoDrive Control. The numerical inputs determines the number of steps and the step size for radial intensity profiles generated in the look up table.

The zero position of the tether must now be determined. This is done by moving the magnets to a height that allows the magnetic bead to touch the bottom of the channel while tracking the z position. Move the magnets to position 5.000mm using the numerical input of the Linear Stage Control vi. The extension of the molecule will

change from zero to a negative number on the Bead Position vi (Figure 22). Once the magnets have reached position 5.0000, press the “Define Zero” button on the Bead Position vi (Figure 22, red square). This will record the lowest z position the magnetic bead reaches, which will be used to define zero. Wait ~10 seconds, then press the “Define Zero” button again, the z position will change to zero. Now move the magnets to the minimum distance above the channel, typically this is position 20.5000mm.

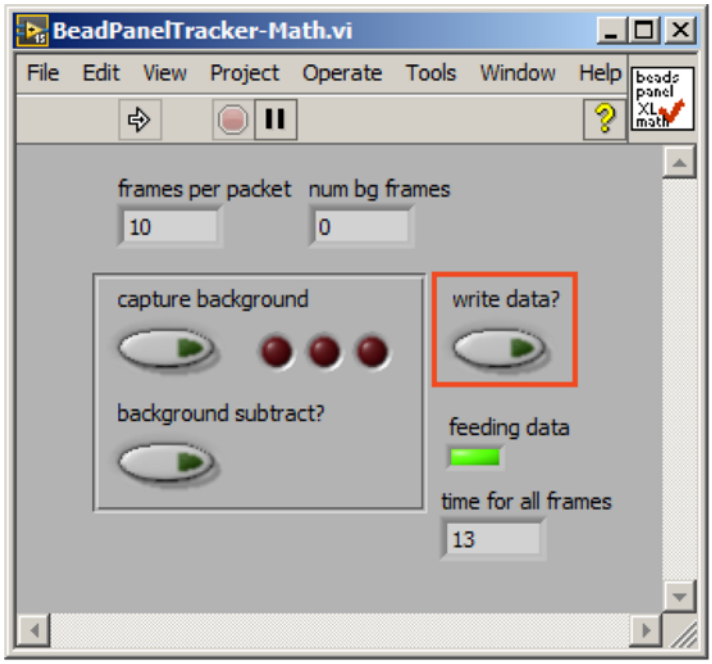

Figure 23 – Bead Panel Math vi. The write data button controls whether data is written to the directory set in the Andor XION 860 vi.

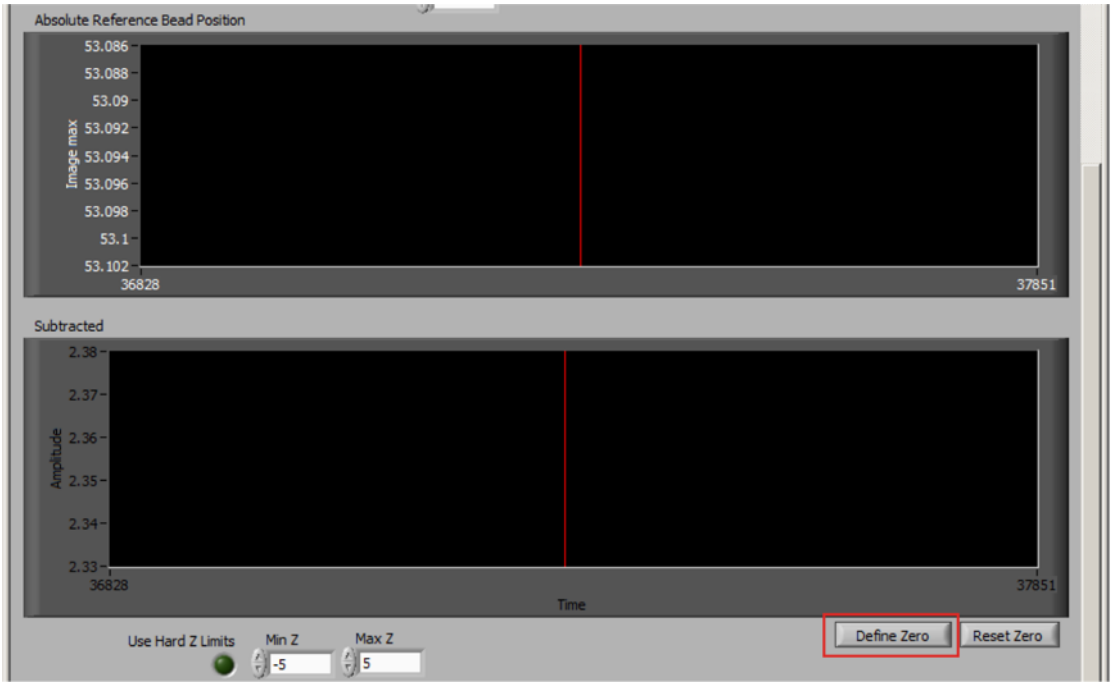

Figure 22 – Bead Position vi. Displays the z position of the magnetic bead. The Define Zero button in the red square defines the position where the magnetic bead is at the bottom of the channel.

Force Calibration

Because the magnetic material in the magnetic bead is not uniform between beads, the force applied to each tether as a function of magnet position must be calibrated for each molecule. This is done by measuring the variance of bead position at various magnet heights, and then using these measurements to calculate the force[13].

In the Andor XION 860 vi, set the exposure time to 0.002s and click “Load Settings”. Click on the folder icon to set the path to where data will be written. In the Bead Tracker Math vi, click the button “Write Data” (Figure 23, red square). Click in the Andor XION 860 vi and press the spacebar to start writing data. The measured

extension at each magnet position will be averaged over the period of time the magnets are held at each position. The amount of time data should be collected at each magnet position is dependent on the variance of the measured extension at each magnet position. Acquisition times for each magnet position are listed in Table 3. Once the data collection is complete, click on the Andor XION 860 vi and press the spacebar to stop data collection.

Magnet Position	Acquisition Time (min)
20.5	0:20
20.0	0:20
19.5	0:20
19.0	0:40
18.5	0:40
18.0	0:40
17.5	0:40
17.0	1:00
16.5	1:00
16.0	1:00
15.5	1:30
15.0	1:30
14.5	1:30
14.0	2:00
13.5	2:00

Table 3 – Force calibration acquisition times.

To analyze the data, five MATLAB scripts will be used: readMTfile5.m, GEAF.m, exp2fitter.m, fit_WLC_weighted.m, and MPcalculator.m (all MATLAB scripts can be found in the data share in the directory: SRG Public Share/Terren/MATLAB Scripts). First run the readMTF5.m script, which reads in the data and sorts it into useful data arrays. The script will first prompt the user to input the frame rate, which is 490 frames per second.

The script will then ask the user what to plot, select “FEC”. The script will finish by plotting the extension of the molecule as a function of time, along with the magnet positions (Figure 24).

Next the forces must be calculated from the variance of x and y positions. The DNA in a magnetic trap can be modeled as a Hookean spring, and the forces can be calculated using the following equation:

$$F_x = \frac{k_b T\langle z\rangle}{\partial x^2} \qquad F_y \frac{k_b T\langle z\rangle}{\partial (y+r)^2}$$

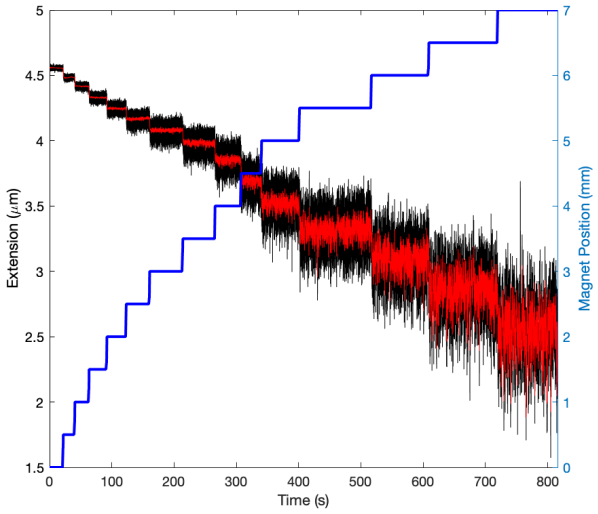

Figure 24 – Force extension calibration. readMTF5.m outputs the read in data into useful data arrays and plots the extension of the molecule as a function of time as well as the magnet positions.

Where k_b is the Boltzmann constant, T is the temperature, and z is the extension of the tether. Run the script GEAF.m. The program will generate two arrays, an array of the averaged extension at each manet positions titled, "extensions" and "xForcesCorrected" which is the calculated force in the x direction corrected for blur[2]. To generate an expression for the force as a function of magnet position, run the script exp2fitter.m, which fits a double exponential function to the xForcesCorrected array and the magnet positions. The script will output the fit plotted over the data (Figure 25).

The elasticity of double-stranded DNA is well described by the worm-like polymer model having a persistence length of ~50nm[13]. To ensure this tether meets this criteria, run the script fitWLC_weighted.m, which fits the function described by a worm-like chain model to the force extension data. However, at high forces, it is possible that the bead is vibrating so quickly that the position data points are no longer correlated. The characteristic timescale parameter generated by autocorrelation analysis of the x position data for each magnet position is stored in an array titled "xtaus". As a general rule, force and extension data should not be used in the worm-like chain fit for any xtaus values less than 10ms. If the high force data point fail to meet this criteria, delete those data points in the "extensionsWLC" and "mparrayWLC" arrays. The fitWLC_weighted.m script uses a least-squares fitting algorithm to calculate the persistence length and contour length for the DNA tether. The output of

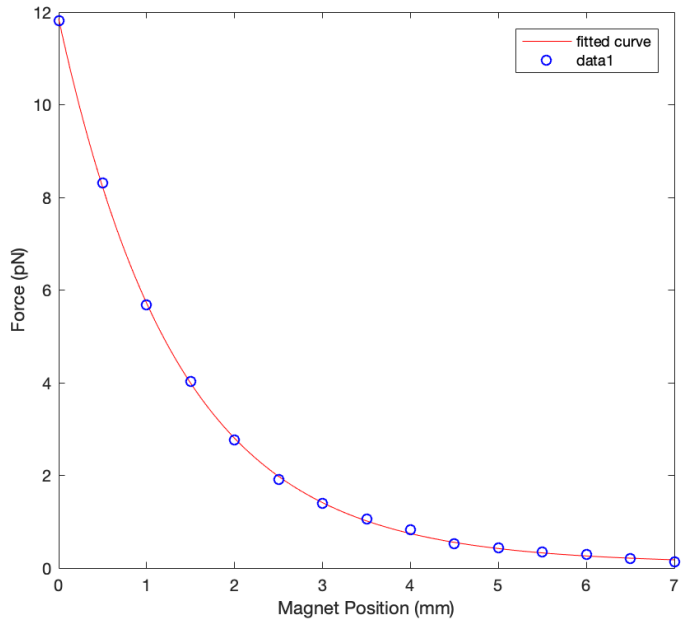

Figure 25 – Double exponential fit of forces as a function of magnet positions. The parameters of this function will be used to calculate the magnet position for a given force set point.

the script shows the worm-like chain fit plotted over the force-extension data as well as displays the calculated persistence length and contour length (Figure 26). With the parameters to the worm-like chain fit calculated, the force at a given extension can be recalculated for the high force set points that were likely underestimated during the exponential fit calculations due to the rapid vibration in the bead, and thus underestimation of the variance in the x position. The fitWLC_weighted.m script calculated the force at a given extension and stores these values in an array titled "calcForces". For the data points removed due to low xtaus values, replace those in the array "xForcesCorrected" with the "calcForces" data points and rerun the exp2fitter.m script. The script MPcalculator.m can then be run to calculate the magnet position for a desired force set point.

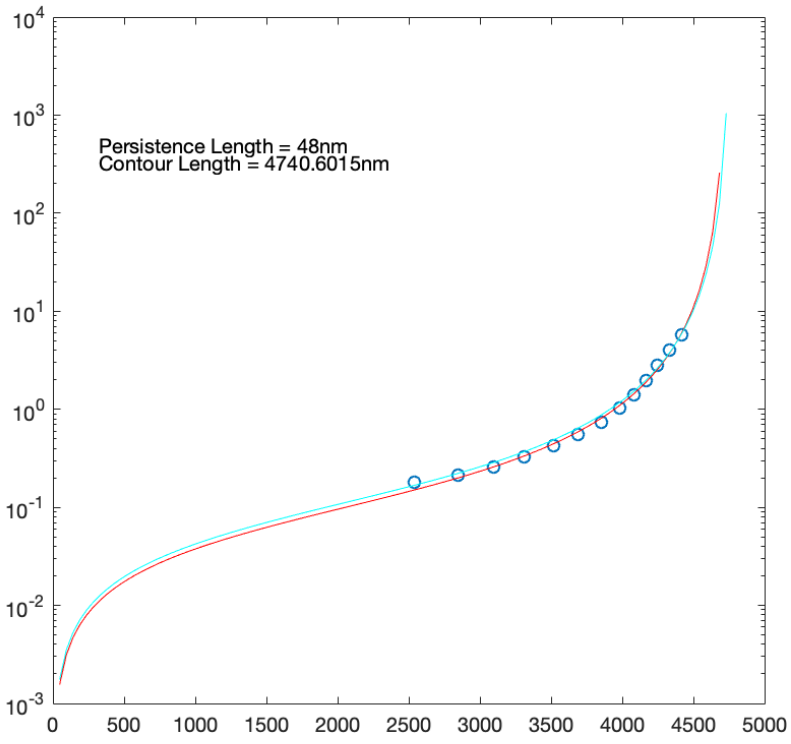

Figure 26 – Worm-like chain fit. The fit to the worm-like chain model is plotted over the force extension data. The persistence length should be ~50nm.

REFERENCES

1. Bouchiat, C.; Wang, M. D.; Allemand, J.; Strick, T.; Block, S. M.; Croquette, V., Estimating the persistence length of a worm-like chain molecule from force-extension measurements. *Biophys J* **1999,** *76* (1 Pt 1), 409-13.

2. Yu, Z.; Dulin, D.; Cnossen, J.; Kober, M.; van Oene, M. M.; Ordu, O.; Berghuis, B. A.; Hensgens, T.; Lipfert, J.; Dekker, N. H., A force calibration standard for magnetic tweezers. *Rev Sci Instrum* **2014,** *85* (12), 123114.

3. De Vlaminck, I.; Dekker, C., Recent advances in magnetic tweezers. *Annu Rev Biophys* **2012,** *41*, 453-72.

4. Strick, T. R.; Allemand, J. F.; Bensimon, D.; Croquette, V., Behavior of supercoiled DNA. *Biophys J* **1998,** *74* (4), 2016-28.

5. Strick, T.; Allemand, J.; Croquette, V.; Bensimon, D., Twisting and stretching single DNA molecules. *Prog Biophys Mol Biol* **2000,** *74* (1-2), 115-40.

6. Dulin, D.; Cui, T. J.; Cnossen, J.; Docter, M. W.; Lipfert, J.; Dekker, N. H., High Spatiotemporal-Resolution Magnetic Tweezers: Calibration and Applications for DNA Dynamics. *Biophys J* **2015,** *109* (10), 2113-25.

7. Lof, A.; Walker, P. U.; Sedlak, S. M.; Gruber, S.; Obser, T.; Brehm, M. A.; Benoit, M.; Lipfert, J., Multiplexed protein force spectroscopy reveals equilibrium protein folding dynamics and the low-force response of von Willebrand factor. *Proc Natl Acad Sci U S A* **2019,** *116* (38), 18798-18807.

8. Jacobson, D. R.; Saleh, O. A., Magnetic tweezers force calibration for molecules that exhibit conformational switching. *Rev Sci Instrum* **2016,** *87* (9), 094302.

9. Long, X.; Parks, J. W.; Bagshaw, C. R.; Stone, M. D., Mechanical unfolding of human telomere G-quadruplex DNA probed by integrated fluorescence and magnetic tweezers spectroscopy. *Nucleic Acids Res* **2013,** *41* (4), 2746-55.

10. Lipfert, J.; Koster, D. A.; Vilfan, I. D.; Hage, S.; Dekker, N. H., Single-molecule magnetic tweezers studies of type IB topoisomerases. *Methods Mol Biol* **2009,** *582*, 71-89.

11. Ivanov, I. E.; Wright, A. V.; Cofsky, J. C.; Aris, K. D. P.; Doudna, J. A.; Bryant, Z., Cas9 interrogates DNA in discrete steps modulated by mismatches and supercoiling. *Proc Natl Acad Sci U S A* **2020,** *117* (11), 5853-5860.

12. Lipfert, J.; Klijnhout, S.; Dekker, N. H., Torsional sensing of small-molecule binding using magnetic tweezers. *Nucleic Acids Res* **2010,** *38* (20), 7122-32.

13. Bustamante, C.; Marko, J. F.; Siggia, E. D.; Smith, S., Entropic elasticity of lambda-phage DNA. *Science* **1994,** *265* (5178), 1599-600.

CHAPTER V

FUTURE DIRECTIONS

TRF2 BINDING EXPERIMENTS

Of the proteins in the shelterin complex, TRF2 is perhaps the most well studied[1] due to its historical significance[2] and clinical relevance[3]. Knockdown of TRF2 induces non-homologous end joining (NHEJ) and an ATM signaling-dependent DNA damage response[4]. TRF2 has been implicated in extra-telomeric functions such as transcriptional repression of oncogenic promoters[5]. It has been shown to slide on double-stranded DNA; however it's mobility is slowed on telomeric DNA substrates[6]. TRF2 has been shown to wrap DNA in a chiral fashion and this wrapping promotes strand invasion in neighboring DNA, suggesting a mechanism for telomere loop (t-loop) formation[7]. TRF2 forms a heterodimer with the shelterin protein Rap1, and it has been shown that Rap1 modulates the affinity of TRF2 for telomeric DNA[8]. TRF2 has a N-terminal basic domain, and this domain increases the affinity of TRF2 for telomeric DNA[9]. Here I will describe a single-molecule magnetic tweezer assay that demonstrates TRF2 will compact telomeric DNA against an externally applied force, and this compaction is modulated by the n-terminal basic domain of TRF2 and the

presence of Rap1. I will then discuss future experiments designed to further investigate the mechanism of this observed DNA compaction.

Experimental design

To eliminate confounding topological effects due to DNA supercoiling, all experiments we performed on nicked, torsionally unconstrained DNA molecules of uninterrupted telomeric repeats ~12kbps in length. A molecule is first held at a force set point of 10pN while protein is introduced to the channel (Figure 1). It was determined empirically that at this force, TRF2 is unable to compact the DNA molecule.

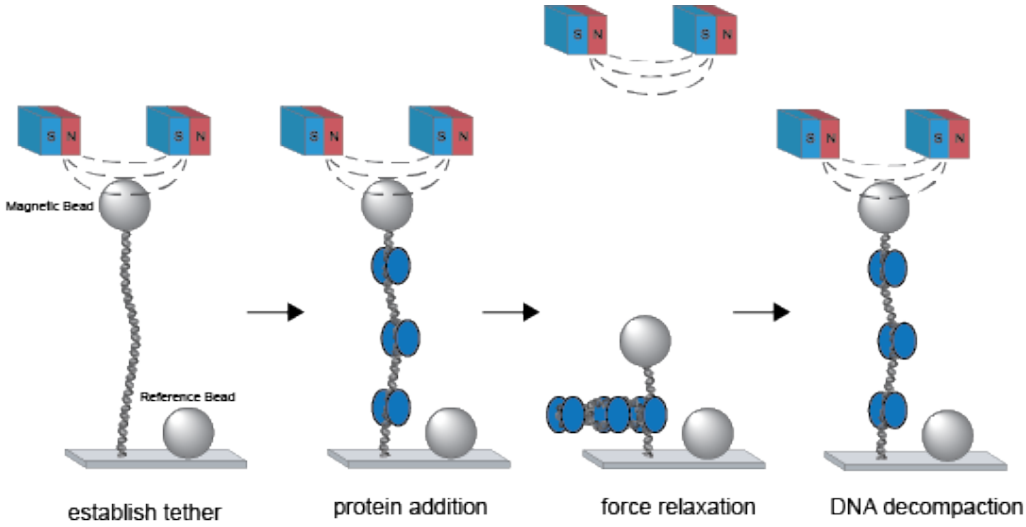

Figure 1 – TRF2 binding magnetic tweezer experimental setup. At high force, protein is introduced to the channel and binds the target molecule. The molecule is then relaxed to a given force set point and allowed to compact. The molecule is then stretched at high force so the experiment can be repeated.

After protein introduction, the molecule is then relaxed to a given force set point at held at that force for 10 minutes. The molecule is then returned to a stretching force of 10pN so the experiment ca be repeated.

Results

At a protein concentration of 10nM TRF2, DNA compaction was not observed above 3pN (Figure 2A). At a force between 2pN and 3pN, slow DNA compaction was observed (Figure 2A, orange and green traces) however when the molecule was stretched at 10pN, significant decompaction was observed (Figure 2A, grey box) suggesting the structures formed during compaction were removed under these experimental conditions. When returned to a force set point between 2-3pN, the DNA molecule again compacted, suggesting during DNA stretching the protein remained bound to the DNA. When to force was set to

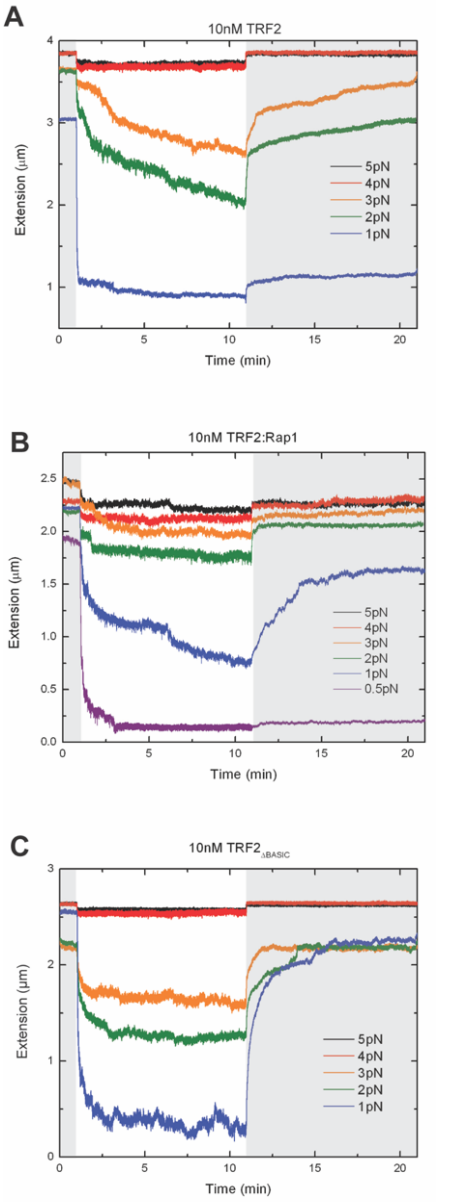

Figure 2 – TRF2 dependent telomeric DNA compaction against an externally applied force. Grey boxed correspond to a force set point of 10pN. A) TRF2 alone rapidly compacts DNA at lower force set points. B) The presence of Rap1 modulates the ability of TRF2 to compact DNA. C) The n-terminal basic domain of TRF2 aids in DNA compaction.

1pN, the molecule rapidly compacted (Figure 2A, blue trace) and upon stretching at 10pN no significant decompaction was observed. Taken together, these data suggest that the structures formed at 1pN were different than those formed during DNA compaction at higher forces.

The experiment was then repeated, with TRF2 pre-incubated with a 1:1 molar ratio of Rap1. Like TRF2 alone, no significant DNA compaction was observed at the higher force set points (Figure 2B, black and red traces). However, unlike TRF2 alone, no significant DNA compaction was observed at the moderate force set points of 2-3pN (Figure 2B, orange and green traces). At the force set point of 1pN, significant DNA compaction was observed albeit at a slower rate than TRF2 alone, and this compaction was reversible under these experimental conditions (Figure 2B, blue trace). At 0.5pN (a condition that was not permitted with TRF2 alone) the DNA rapidly compacted and DNA decompaction was not observed when stretched at 10pN. Taken together, these data suggest that the presence of Rap1 modulate the ability of TRF2 to compact DNA against an externally applied force.

The experiment was again repeated, this time with a truncated TRF2 mutant lacking the basic n-terminal domain. This mutant failed to compact the DNA molecule at the higher force set points (Figure 2C, black and red traces). At the intermediate force set points of 2-3pN, the molecule rapidly compacted to an intermediate extension, but unlike the full-length protein, no slow further compaction was observed (Figure 2C, orange and green traces). At the low 1pN force set point, the molecule was rapidly compacted, however unlike the full length protein, this compaction was reversible under these experimental conditions. Taken together, these data suggest

the N-terminal basic domain of TRF2 assists in DNA compaction against an externally applied force.

Future experiments

An open question raised by these experiments is what is the mechanism of this observed DNA compaction? Since TRF2 is known to wrap DNA, it could be the case that DNA wrapping results in compaction. A second model is that TRF2 compacts DNA through protein-protein interactions, and these interactions are responsible for the

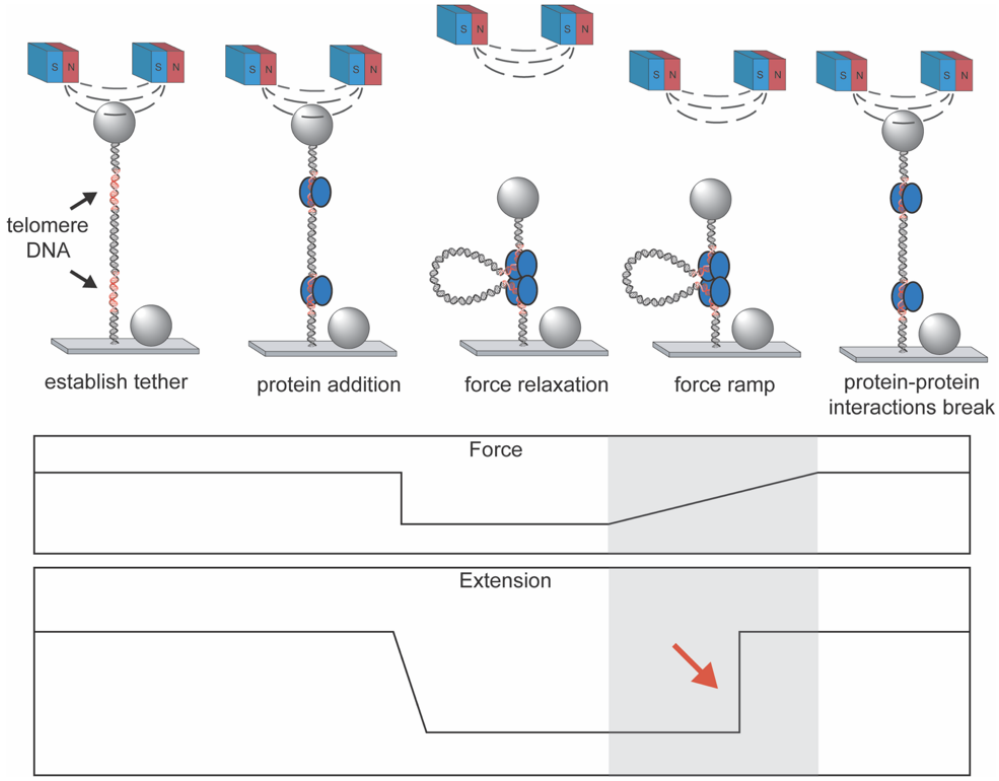

Figure 3 – Proposed future force ramp experiment. Telomeric DNA shown in red, TRF2 shown in blue. Protein in introduced to the channel at high force. The DNA is then relaxed to allow the two distal telomere fragments to come into contact with each other. The force is then slowly increased back to high force. If two TRF2 molecules each bound to the distal telomere fragments are making protein-protein contacts, once a critical force is reached that breaks these interactions a rapid change in extension would be observed proportional to the length of the DNA flanked by the two telomere fragments (red arrow).

observed DNA compaction. An experiment designed to test this model is outlined in Figure 3. In this proposed experiment, a DNA molecule is designed with two telomere fragments separated by non-telomeric DNA. Since TRF2 has a higher affinity for telomeric DNA than non-telomeric DNA, a low protein concentration could be introduced to this molecule such that only the telomeric sites on the molecule are bound by TRF2. The molecule could then be relaxed to allow these distal telomere fragments to come into contact. Then the force could slowly be increased to 10pN (Figure 3, grey boxes). If TRF2 is making protein-protein interactions between molecules bound to the two distal telomere sites, one would expect that after a critical force is reached, these interaction would suddenly break, resulting in a rapid change in extension (Figure 3, red arrow) proportional to the length of DNA flanked by the telomere fragments.

WRN PROTEIN, TOPOISOMERASE 1B, AND CAMPTOTHECIN EXPERIMENTS

This project was first introduced to the lab as a collaboration with Dr. Hanlee Ji, Associate professor of Oncology at Stanford University. Dr. Ji made an observation in a study investigating the efficacy of treating colorectal cancer patients with the chemotherapeutic agent irinotecan, a camptothecin derivative and a standard of care drug for colorectal cancer. Camptothecin is a topoisomerase 1b (top1b) poison which binds in the active site of the enzyme[10] and reduces the ability of top1b to relax supercoiled DNA[11]. It is presumed that in rapidly dividing cancer cells, the reduced ability of these cells to relax supercoiled DNA after treatment with camptothecin causes replication fork stalling and DNA damage, which induces apoptosis[12]. Dr. Ji

observed that in patients that have higher levels of the RecQ like helicase Werner Protein (WRN), the efficacy of irinotecan treatment was greatly reduced. It was previously reported that WRN and top1b coimmunoprecipitate[13], and WRN will stimulate top1b activity while top1b will reduce WRN helicase activity[14]. The hypothesis then became patients with higher levels of WRN are resistant to irinotecan due to a direct interaction between WRN and top1b preventing the drug from poisoning the enzyme.

Experimental design and preliminary results

We designed a single-molecule magnetic tweezer based DNA topology assay to investigate the possibility of a direct interaction between top1b and WRN helicase, and if this interaction increases the ability of top1b to relax supercoiled DNA in the presence of the camptothecin-based top1b poison SN-38[15]. First, a molecule is supercoiled resulting in a decrease of the extension of the DNA molecules due to superhelical density partitioning into writhe[16]. If a top1b molecule diffusing in solution binds to the supercoiled molecule and relaxed it, a rapid increase in the extension will be observed (Figure 4A). This can be quantified by calculating the relaxation velocity, which is the change in extension over time during the relaxation event (Figure 4B). However, if top1b is bound to SN-38 while performing the DNA relaxation, a slow gradual change in extension will be observed as previously reported[11] resulting in a reduction in the relaxation velocity (Figure 4C). With this system established, it could

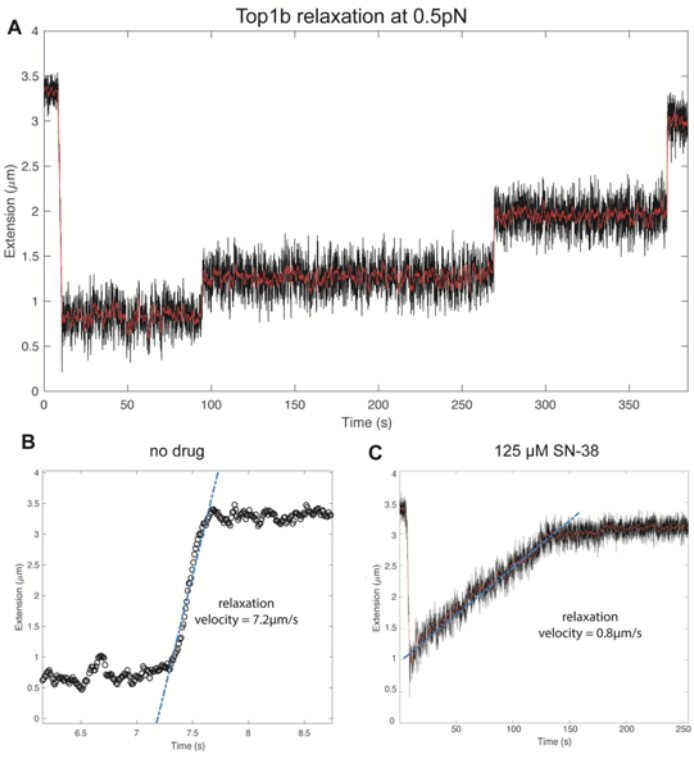

Figure 4 – Effects of SN-38 on the relaxation velocity of top1b. A) Time trace showing individual DNA relaxation events by top1b. B) Relaxation velocity calculation for a single event. C) SN-38 results in a drastic slowing of the relaxation velocity of top1b.

be tested if the addition of WRN results in the abolishment of the slow relaxation events indicative of poisoned top1b enzymes.

Future experiments

The above experiment performed in the presence of WRN was the ultimate goal of this project. This was attempted using a purified fragment of WRN, where the first 51 amino acids was purified from overexpression in *E. coli*, a fragment that was previously reported to be sufficient for top1b stimulation[14]. This experiment had no obvious difference in the magnetic tweezer based assay, however the addition of this

material to gel based DNA relaxation experiments showed that this material changed the supercoiling state of plasmid DNA but was not top1b dependent (data not shown). The conclusion was that there was a contaminating enzyme in the preparation of the WRN fragment, and that contaminant was responsible for the DNA relaxation in the plasmid based assay. It would be interesting to repeat the magnetic tweezer experiment using full length WRN.

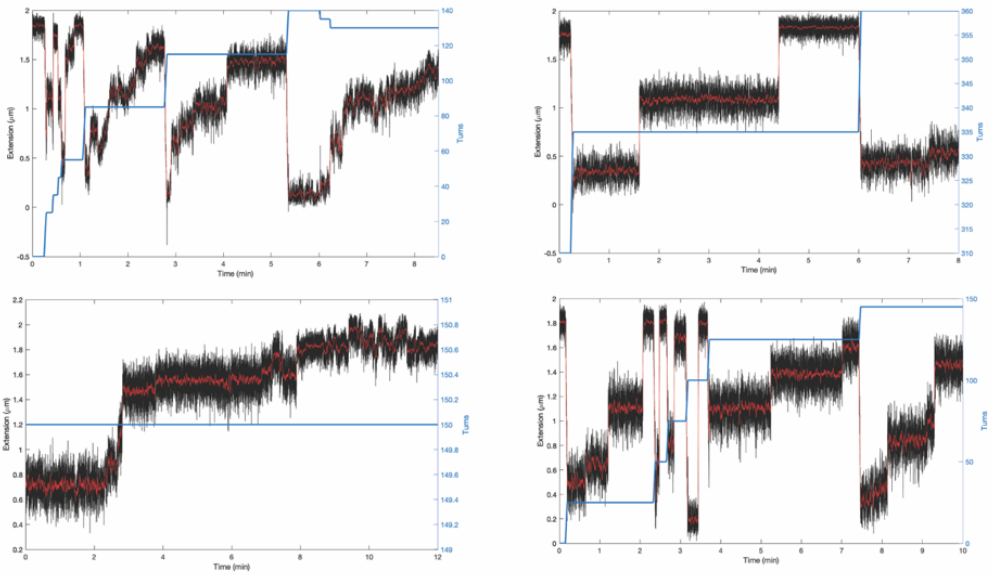

Figure 5 – Representative traces of top1b telomeric DNA relaxation in the presence of 125μM SN-38. Plotted in blue on the right y axis is the amount of turns applied to the molecule. Relaxation events were a combination of fast relaxation and slow relaxation. In the absence of drug, no relaxation was observed.

One interesting result came when the magnetic tweezer-based assay was performed using telomeric DNA molecules. Surprisingly, when top1b was introduced to the telomere molecules, relaxation was never observed (data not shown). Interestingly, only in the presence of SN-38 was DNA relaxation ever observed, and the relaxation events where a combination of fast relaxation and slow relaxation (Figure 5). One possible explanation for this observation is the telomere sequence

being a poor substrate for top1b. Only in the presence of drug is the enzyme trapped on the molecule for a long enough period of time to go through the catalytic cycle.

TELOMERIC NUCLEOSOMES

Due to the clinical relevance of the shelterin complex, many telomeric chromatin studies often overlook the presence of nucleosomes at the telomere[17]. Approximately 80% of the telomere is bound by tightly spaced nucleosomes separated by 10-15bp of linker DNA[18]. *In vitro* studies using chromatinized telomeric substrates have demonstrated that both the TRF proteins in the shelterin complex alter nucleosome spacing[19]. Albeit with a weakened affinity, both TRF1 and TRF2 have the capacity to bind nucleosomal DNA compared to free DNA and this binding is modulated by the histone tails, the n-terminal basic domain of TRF2, and the n-terminal acidic domain of TRF1[20]. Nucleosome binding energetics and positioning is dictated by the sequence of the DNA[21], and due to the repetitive nature of telomere all positions 6bp apart are predicted to be isoenergetic[22]. *In vitro* gel-based assays demonstrate that the addition of TRF1 to telomere-positioned nucleosomes causes nucleosome migration to neighboring non-telomeric sequences[23-24]. This project aimed to better characterize telomeric nucleosome positioning and the effects shelterin proteins have on their position.

Experimental design

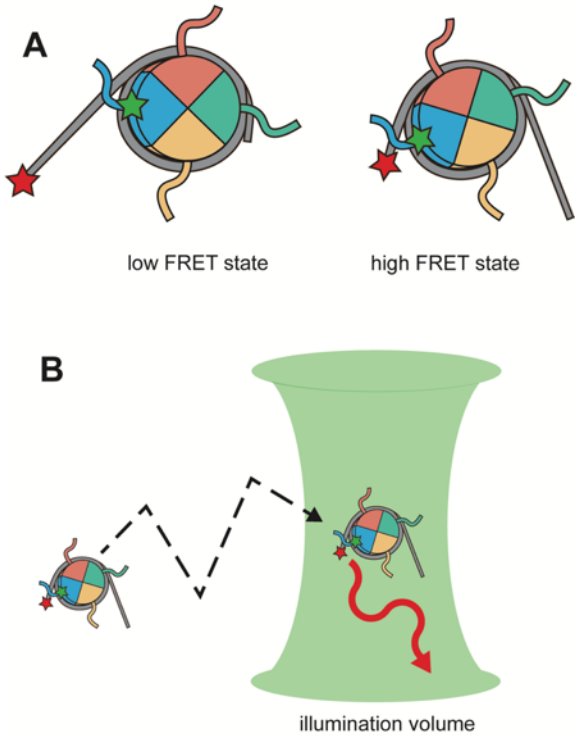

Figure 6 – Experimental setup. A) Inter-dye distance determines the efficiency of energy transfer. B) Molecules freely diffuse into the illumination volume where FRET is measured.

Telomeric nucleosomes were reconstituted by refolding 212bp of telomeric DNA with a cy5 dye incorporated into the DNA using a PCR with a dye labeled primer. Nucleosome octamers were refolded[25] using an engineered cy3 dye labeled on H2A K120C as previously reported[26] (Figure 6A). Non-scanning confocal microscopy was then employed to measure the Förster resonance energy transfer (FRET) between the two dyes, where the efficiency of the energy transfer is proportional to the distance between the two dyes (Figure 6B). TRF2 was then titrated in to monitor the effect the protein had on the FRET distribution.

Results

The FRET distribution with no protein in solution was broad, with no discernable individual population (Figure 7A). This is consistent with a heterogenous distribution of nucleosome positions on the telomeric DNA, with no energetic preference for one position over another. At low protein concentration, this distribution

remained largely unchanged (Figure 7B, C). However, at a protein concentration of 1μM, a defined mid-FRET peak at 0.6 emerged (Figure 7D). These data suggest that TRF2 is having an ordering effect on the nucleosome positions, transitioning the distribution into one structure. Determination of the nature of this structure required further experimentation.

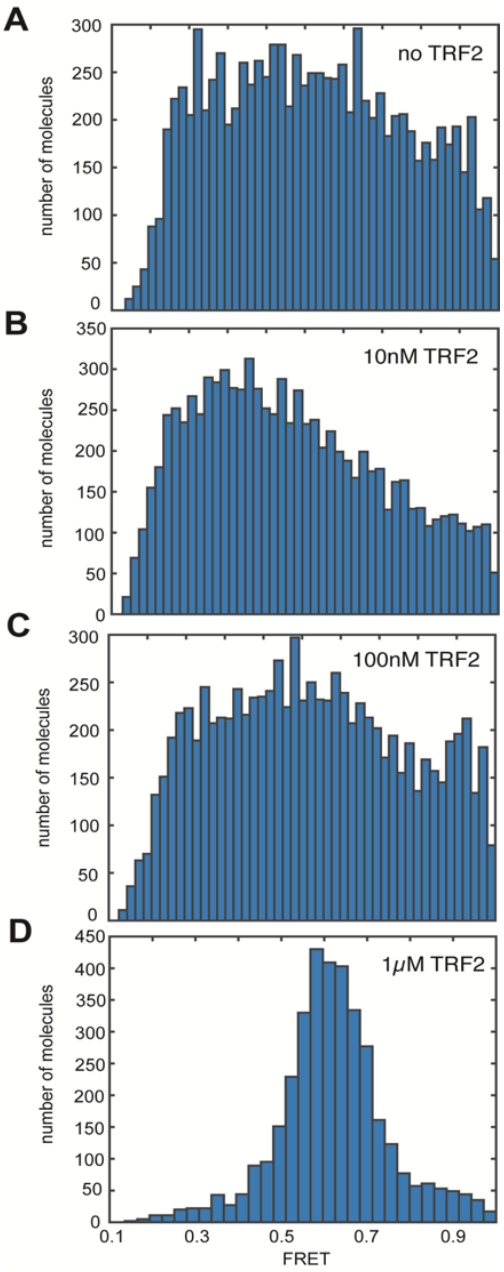

Figure 7 – TRF2 orders heterogeneously positioned telomeric nucleosomes. Telomeric nucleosomes display a broad FRET distribution indicative of heterogeneous nucleosome positioning. Addition of TRF2 results in the formation of a single population, suggesting TRF2 is ordering these structures.

Future Experiments

The confocal data suggest that telomeric nucleosome positions are isoenergetic, with no preference for one position over another. However, these data are incapable of determining if these nucleosome positions are interconverting between each other, or once folded they are locked in place. To monitor the position of a telomeric nucleosome over time, a prism-based single-molecule FRET experiment using surface-immobilized nucleosomes could be performed (Figure

8). Nucleosome dynamics could be monitored over time at different temperatures, ionic strengths, and in the presence of shelterin proteins. Data gleaned from these experiments would expand our understanding of how telomeric chromatin transitions between a closed protected state required for chromosomal end protection and an open state required for telomere replication.

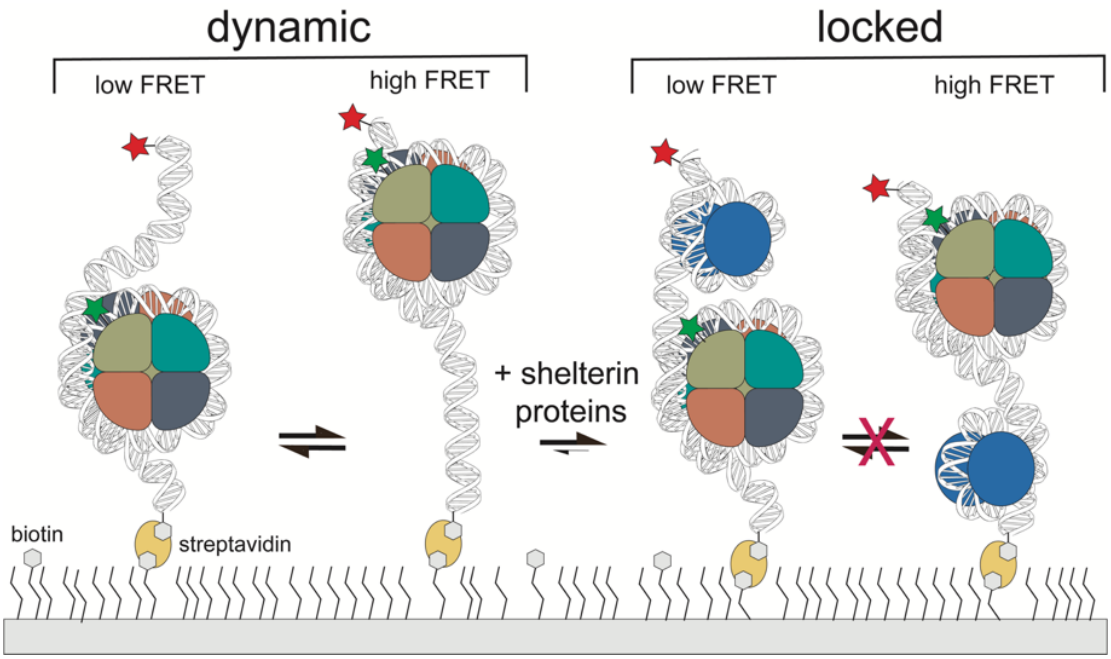

Figure 8 – Proposed TIRF-based FRET experiment. Telomeric nucleosome dynamics could be monitored over time. The effects of temperature and/or ionic strength on nucleosome dynamics could be monitored. Shelterin proteins could be introduced to monitor their effects on telomeric nucleosome dynamics.

REFERENCES

1. de Lange, T., Shelterin-Mediated Telomere Protection. *Annu Rev Genet* **2018,** *52*, 223-247.

2. Zhong, Z.; Shiue, L.; Kaplan, S.; de Lange, T., A mammalian factor that binds telomeric TTAGGG repeats in vitro. *Mol Cell Biol* **1992,** *12* (11), 4834-43.

3. Ozden, S.; Tiber, P. M.; Ozgen, Z.; Ozyurt, H.; Serakinci, N.; Orun, O., Expression of TRF2 and its prognostic relevance in advanced stage cervical cancer patients. *Biol Res* **2014,** *47*, 61.

4. Celli, G. B.; de Lange, T., DNA processing is not required for ATM-mediated telomere damage response after TRF2 deletion. *Nat Cell Biol* **2005,** *7* (7), 712-8.

5. Hussain, T.; Saha, D.; Purohit, G.; Kar, A.; Kishore Mukherjee, A.; Sharma, S.; Sengupta, S.; Dhapola, P.; Maji, B.; Vedagopuram, S.; Horikoshi, N. T.; Horikoshi, N.; Pandita, R. K.; Bhattacharya, S.; Bajaj, A.; Riou, J. F.; Pandita, T. K.; Chowdhury, S., Transcription regulation of CDKN1A (p21/CIP1/WAF1) by TRF2 is epigenetically controlled through the REST repressor complex. *Sci Rep* **2017,** *7* (1), 11541.

6. Lin, J.; Countryman, P.; Buncher, N.; Kaur, P.; E, L.; Zhang, Y.; Gibson, G.; You, C.; Watkins, S. C.; Piehler, J.; Opresko, P. L.; Kad, N. M.; Wang, H., TRF1 and TRF2 use different mechanisms to find telomeric DNA but share a novel mechanism to search for protein partners at telomeres. *Nucleic Acids Res* **2014,** *42* (4), 2493-504.

7. Amiard, S.; Doudeau, M.; Pinte, S.; Poulet, A.; Lenain, C.; Faivre-Moskalenko, C.; Angelov, D.; Hug, N.; Vindigni, A.; Bouvet, P.; Paoletti, J.; Gilson, E.; Giraud-Panis, M. J., A

topological mechanism for TRF2-enhanced strand invasion. *Nat Struct Mol Biol* **2007,** *14* (2), 147-54.

8. Janouskova, E.; Necasova, I.; Pavlouskova, J.; Zimmermann, M.; Hluchy, M.; Marini, V.; Novakova, M.; Hofr, C., Human Rap1 modulates TRF2 attraction to telomeric DNA. *Nucleic Acids Res* **2015,** *43* (5), 2691-700.

9. Necasova, I.; Janouskova, E.; Klumpler, T.; Hofr, C., Basic domain of telomere guardian TRF2 reduces D-loop unwinding whereas Rap1 restores it. *Nucleic Acids Res* **2017,** *45* (21), 12170-12180.

10. Staker, B. L.; Feese, M. D.; Cushman, M.; Pommier, Y.; Zembower, D.; Stewart, L.; Burgin, A. B., Structures of three classes of anticancer agents bound to the human topoisomerase I-DNA covalent complex. *J Med Chem* **2005,** *48* (7), 2336-45.

11. Koster, D. A.; Palle, K.; Bot, E. S.; Bjornsti, M. A.; Dekker, N. H., Antitumour drugs impede DNA uncoiling by topoisomerase I. *Nature* **2007,** *448* (7150), 213-7.

12. Delgado, J. L.; Hsieh, C. M.; Chan, N. L.; Hiasa, H., Topoisomerases as anticancer targets. *Biochem J* **2018,** *475* (2), 373-398.

13. Lebel, M.; Spillare, E. A.; Harris, C. C.; Leder, P., The Werner syndrome gene product co-purifies with the DNA replication complex and interacts with PCNA and topoisomerase I. *J Biol Chem* **1999,** *274* (53), 37795-9.

14. Laine, J. P.; Opresko, P. L.; Indig, F. E.; Harrigan, J. A.; von Kobbe, C.; Bohr, V. A., Werner protein stimulates topoisomerase I DNA relaxation activity. *Cancer Res* **2003,** *63* (21), 7136-46.

15. Kawato, Y.; Aonuma, M.; Hirota, Y.; Kuga, H.; Sato, K., Intracellular roles of SN-38, a metabolite of the camptothecin derivative CPT-11, in the antitumor effect of CPT-11. *Cancer Res* **1991,** *51* (16), 4187-91.

16. Strick, T.; Allemand, J.; Croquette, V.; Bensimon, D., Twisting and stretching single DNA molecules. *Prog Biophys Mol Biol* **2000,** *74* (1-2), 115-40.

17. Pisano, S.; Galati, A.; Cacchione, S., Telomeric nucleosomes: forgotten players at chromosome ends. *Cell Mol Life Sci* **2008,** *65* (22), 3553-63.

18. Galati, A.; Magdinier, F.; Colasanti, V.; Bauwens, S.; Pinte, S.; Ricordy, R.; Giraud-Panis, M. J.; Pusch, M. C.; Savino, M.; Cacchione, S.; Gilson, E., TRF2 controls telomeric nucleosome organization in a cell cycle phase-dependent manner. *PLoS One* **2012,** *7* (4), e34386.

19. Galati, A.; Rossetti, L.; Pisano, S.; Chapman, L.; Rhodes, D.; Savino, M.; Cacchione, S., The human telomeric protein TRF1 specifically recognizes nucleosomal binding sites and alters nucleosome structure. *J Mol Biol* **2006,** *360* (2), 377-85.

20. Galati, A.; Micheli, E.; Alicata, C.; Ingegnere, T.; Cicconi, A.; Pusch, M. C.; Giraud-Panis, M. J.; Gilson, E.; Cacchione, S., TRF1 and TRF2 binding to telomeres is modulated by nucleosomal organization. *Nucleic Acids Res* **2015,** *43* (12), 5824-37.

21. Onufriev, A. V.; Schiessel, H., The nucleosome: from structure to function through physics. *Curr Opin Struct Biol* **2019,** *56*, 119-130.

22. Cacchione, S.; Cerone, M. A.; Savino, M., In vitro low propensity to form nucleosomes of four telomeric sequences. *FEBS Lett* **1997,** *400* (1), 37-41.

23. Pisano, S.; Leoni, D.; Galati, A.; Rhodes, D.; Savino, M.; Cacchione, S., The human telomeric protein hTRF1 induces telomere-specific nucleosome mobility. *Nucleic Acids Res* **2010,** *38* (7), 2247-55.

24. Pisano, S.; Marchioni, E.; Galati, A.; Mechelli, R.; Savino, M.; Cacchione, S., Telomeric nucleosomes are intrinsically mobile. *J Mol Biol* **2007,** *369* (5), 1153-62.

25. Luger, K.; Rechsteiner, T. J.; Richmond, T. J., Preparation of nucleosome core particle from recombinant histones. *Methods Enzymol* **1999,** *304*, 3-19.

26. Yang, J. G.; Narlikar, G. J., FRET-based methods to study ATP-dependent changes in chromatin structure. *Methods* **2007,** *41* (3), 291-5.